Department of BIOTECHNOLOGY AND BIOSCIENCES

PhD program in TRANSLATIONAL AND MOLECULAR MEDICINE (DIMET)

XXXIV Cycle

Orexinergic and cholinergic function in the brain ascending modulatory system and its implications in sleep-related pathologies

Candidate	Giulia Colombo
Registration number	775520
Tutor	Andrea Becchetti
Co-tutor	Anne Vassalli
Coordinator	Andrea Biondi

ACADEMIC YEAR 2021/2022

To those who made me eager to be,

to know, to live.

A coloro che hanno generato in me la smania di essere,
di sapere, di vivere.

A mia madre, mio padre, alla mia famiglia (e a tutti i suoi membri pelosi o piumati), al mio ragazzo, aə mieə amicə, compagnə e colleghə.

Table of Contents

Chapter 1. General Introduction 11

The brain ascending regulatory system 11

Rhythm generation, arousal and sleep/wake regulation . 15

Sleep disorders and sleep-related diseases as rhythmopaties 18

Aim of the thesis 19

References 23

PART I. The cholinergic system and the Autosomal Dominant Sleep-related Hypermotor Epilepsy 27

Sleep-related Hypermotor Epilepsy and ADSHE 27

The cholinergic system 31

The prefrontal cortex (PFC) as a cholinergic innervation target 32

References 36

Chapter 2. CHRNA2 and nocturnal frontal lobe epilepsy: Identification and characterization of a novel loss of function mutation 41

Abstract 41

Introduction 43

Materials and Methods 46

Culture and Transfection Procedure 46

Patch-Clamp Recordings 47

Statistical Analysis 49

Results 50

Patient and Mutation 50

Mutation effects on the Channel Function 52
Discussion 60
Appendix. Implication of CHRNA2 mutations in other epileptic syndromes? 62
$\alpha2^{Arg121Leu}$ Mutation 62
Discussion 66
References 67
Chapter 3. Morpho-functional alterations in the prefrontal cortex layer V of mice conditionally expressing the ADSHE-linked $\beta2^{V287L}$ nAChR subunit. Possible role of α2 subunits. ... 73
Abstract 73
Introduction 74
Materials and Methods 77
Animals 77
Tissue preparation and brain regions 78
Dendritic arborization and spine density 79
Chemicals and drugs 80
Whole-cell patch-clamp recordings in acute brain slices 80
Analysis of APs 81
Post-recording morphological characterization 82
Statistical analysis 83
Results 83
$\beta2^{V287L}$ effects on Fr2 layer V interneurons 83
Expression of heteromeric nAChRs on layer V interneurons 87
Discussion 96
The possible role of α2 nAChRs in ADSHE seizures* 96

References 98

PART II. The orexinergic system and narcolepsy with cataplexy 104

The orexinergic system 104

Narcolepsy with cataplexy and orexinergic transmission 106

Theta-dominated wakefulness and cataplexy 112

References 116

Chapter 4. Physiological validation of the Orexin Receptor 2 CKO mouse model 122

Abstract 122

Introduction 123

Materials and Methods 126

Brain slices 126

Whole-cell recordings 127

Drugs and solutions 128

Analysis of patch-clamp data 128

Statistics 129

Results 130

References 137

Chapter 5. Orexinergic modulation of the microcircuit activity in the prefrontal cortex: a possible source of θ rhythmogenesis 140

Abstract 140

Introduction 141

Materials and Methods 144

Patch-clamp recording and data analysis 144

Tissue preparation for immunohistochemistry 145
Primary antibodies 145
Immunofluorescence histochemistry 146
Signal intensity and colocalization analysis 147
Results 151
OrxA stimulates glutamatergic transmission in PFC 151
Patch-clamp on C57BL6 mice 158
Distribution of Ox2R in murine PFC 159
Discussion 174
Effects of OrxA and OrxB on the PFC excitatory network 174
Ox1R and Ox2R distribution in the PFC 176
Effects on θ rhythmogenesis 181
References 182
Chapter 6. Orexinergic modulation of the ventral tegmental area: a possible regulator of hippocampal-dependent θ rhythmogenesis 190
Abstract 190
Introduction 191
Materials and Methods 195
Brain slices 195
MEA recordings 197
Patch-clamp recordings 200
Drugs and solutions 200
Results 201
HD-MEA 201

Patch-clamp 212
Discussion 218
References 221
Chapter 7. Summary, Conclusions and Future Perspectives 226
α2* nAChRs role in epileptogenesis 226
Dysfunctional SOM^{+} regular spiking interneurons and ADSHE seizures 227
A possible role for Ox2R in TMN histaminergic neuron maturation 229
Both orexins modulate the microcircuit activity and θ rhythmogenesis in the PFC 231
$Ox2R^{DatCKO}$ profoundly modifies the orexinergic modulation of the microcircuit activity in the VTA 234
Publications 236
Acknowledgements - Ringraziamenti 237

Chapter 1. General Introduction

The brain ascending regulatory system

The brain ascending regulatory system is a complex of interconnected neuronal nuclei of different neurochemical nature, located in the brainstem, basal forebrain and hypothalamus (Fig 1.1). These nuclei regulate arousal, attentive and conscious states in all Mammals, as their evolutionary equivalent do in all the Vertebrates studied so far (Kovalzon, 2016). Such system is also implicated in the autonomic regulation of respiration, heart rate and blood pressure, thus modulating both high and low complexity aspects of behaviour, in a coherent and integrated fashion.

The definition of this anatomo-functional structure, initially called Ascending Reticular Activating System (ARAS), dates back to Moruzzi and Magoun's studies on Bremer's model of "encéphale isolé"- a brain preparation on anesthetized cat with spinal cord transected at C1 (Moruzzi & Magoun, 1949). Electrical stimulation of the paramedian reticular formation, particularly within the midbrain, produced an EEG desynchronization consistent with arousal. Subsequent studies identified a slab of tissue at the junction of the rostral pons and caudal midbrain as critical for maintaining the waking state (Lindsley et al. 1949) and the ARAS began to

be seen as the most important structure to control global brain state. Initially, the neurons responsible for arousal were thought to be part of the undifferentiated reticular formation, but subsequent studies showed that the cell groups at the mesopontine junction that project to the forebrain mainly consist of monoaminergic and cholinergic neurons that reside in specific cell groups rather than in the reticular core (Saper et al. 2010). Nonetheless, a fundamental part of the ARAS is the poorly delineated structure consisting of many axonal fascicles that gave the reticular formation its name. Only very recent technologies, such as tractography, revealed the presence of fine fibre connections and additional bundles, not captured by conventional magnetic resonance imaging (Wijdicks, 2019). Such redundancy of the ascending regulatory system allows, at least in humans, to support wakefulness unless the entire network is destroyed or fully disconnected from the thalamus (Edlow et al. 2013), deposing in favour of its essential role in the economy of brain function.

The ascending regulatory system is composed of monoaminergic nuclei (the noradrenergic locus coeruleus, LC; the serotonergic raphe nuclei; the histaminergic tuberomammillary nucleus, TMN, of the hypothalamus; the dopaminergic ventral tegmental area, VTA) and of cholinergic nuclei (the pedunculopontine, PPT, and laterodorsal

tegmental, LDT, nuclei of the brainstem, and the magnocellular nucleus of the basal forebrain, BF). It also includes other neuronal populations, such as the glutamatergic parabrachial nuclear complex and the adjacent precoeruleus area, and the orexinergic neurons in the posterior half of the lateral hypothalamus (Saper et al. 2010; Eban-Rothschild et al. 2019).

These wake-promoting populations project to various structures through a dorsal and a ventral pathway. The dorsal pathway innervates the thalamus, which facilitates the transmission of sensory information to the cortex. The ventral pathway innervates the hypothalamus, BF, and other forebrain structures, including the cerebral cortex. Wakefulness is thought to be achieved when both pathways are active (Eban-Rothschild et al. 2019). On the other hand, the motor control typical of wakefulness and NREM sleep is granted by the GABAergic neurons in the ventral periaqueductal gray matter (vlPAG) and the adjacent lateral pontine tegmentum (LPT). These neurons, in fact, inhibit and are inhibited by a population of GABAergic neurons in the sublaterodorsal region (SLD) that fires during REM sleep. A separate population of glutamatergic neurons in the SLD activates, as well, groups of inhibitory interneurons in the medulla and spinal cord, which inhibit motor neurons, thus producing REM sleep atonia. This mutually inhibitory

relationship produces a flip-flop switch, modulated in turn by the brain ascending regulatory system. In fact, noradrenergic neurons in the LC and serotoninergic neurons in the DR inhibit REM by exciting REM-off and inhibiting REM-on neurons, whereas cholinergic neurons promote REM sleep by having opposite actions. The orexin neurons inhibit entry into REM sleep by exciting neurons in the REM-off population and by presynaptic effects that excite monoaminergic terminals (Fig. 1.1; Saper et al. 2010).

Figure 1.1. Schematic representation of the brain ascending regulatory system, of the motor control nuclei and their main projections. Cholinergic nuclei: magnocellular preoptic area (MCPO), laterodorsal tegmentum (LDT) and peduncolopontine tegmentum (PPT). Noradrenergic nucleus of the locus coeruleus (LC). Dopaminergic nuclei: ventral tegmental area (VTA) and substantia nigra (SN). Orexinergic nuclei in the lateral hypothalamus (LH). Histaminergic ventral tuberomammillary nucleus of the hypothalamus (vTMN). Serotonergic nucleus of the dorsal raphe (DR).

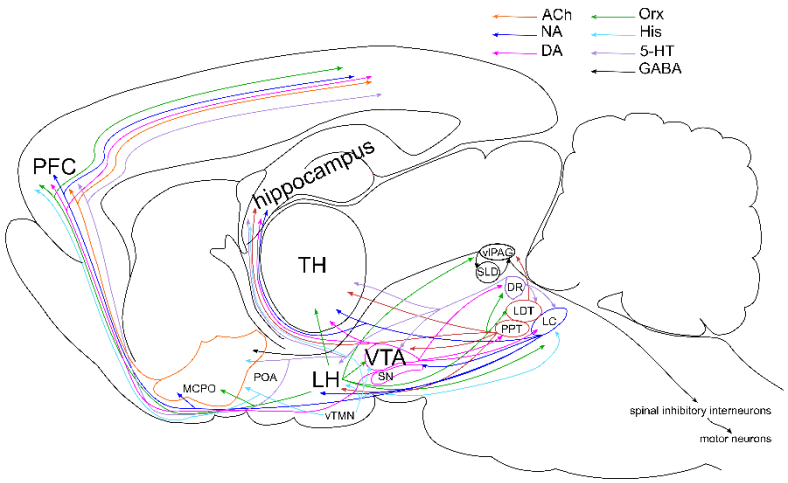

Figure 1.1. *(follows)* GABAergic nuclei: sublaterodorsal tegmental nucleus (SLD) and ventrolateral periacqueductal gray (vlPAG). Preoptic area (POA), prefrontal cortex (PFC) and thalamus (TH) are also represented.

Rhythm generation, arousal and sleep/wake regulation

The brain ascending regulatory system acts at all scales in the brain: it regulates the behaviour and brain state at the slow time scale (hours-minutes); the macrocircuit oscillatory activity and rhythmogenesis at the intermediate time scale (minutes-seconds); and the microcircuit synchronization and synaptic activity at the fast time scale (seconds-milliseconds). All these levels of control are achieved through a variety of neurotransmitters' mechanisms of action, having different time lags and durations (Buzsaki, 2006). Arousal and sleep/wake regulation are major phenomena collectively regulated by the components of such a complex system.

The sleep/wake states differ in various physiological parameters, such as thermoregulation, cardiac activity, metabolism, and respiration (Brown et al. 2012; Saper et al. 2010). Nonetheless, in mammals and birds, sleep and wake states are typically identified using electroencephalogram (EEG), electromyogram (EMG) and electrooculogram (EOG), which respectively record global cortical and muscular

activity, and eye movements. Two distinct sleep states can be recognized, which alternate cyclically across sleep: non-rapid eye movement (NREM), and rapid eye movement (REM) sleep. NREM sleep can be divided into four substates (N1-N4), based on EEG/EMG criteria. Stage 2 is characterized by EEG sleep spindles (bursts of 7–15 Hz oscillations) and K complexes, and leads to stages 3 and 4 (often collectively named slow-wave sleep, SWS). These are characterized by high amplitude low-frequency δ oscillations (0.5–4 Hz), and low postural muscle tone. During REM sleep, EEG is dominated by θ and γ oscillations, with a complete loss of muscle tone in postural muscles (REM atonia), accompanied by rapid eye movements and EEG ponto-geniculate-occipital waves.

The awake state is heterogeneous, with desynchronized EEG oscillations of low amplitude and mixed frequencies, and a variable amount of muscle activity. Active or motivated wakefulness is rich in θ (4–9 Hz) and γ (40–300 Hz) EEG frequency ranges, whereas quiet wakefulness is characterized by slower EEG frequencies, including α (7–15 Hz) and β (8–30 Hz; Eban-Rothschild et al. 2019).

A major factor in wakefulness and cortical rhythm regulation is the balance between the cholinergic and noradrenergic activation. They exert their cortical effects through two main

pathways: 1) direct projections to the neocortex, where they extensively innervate the associative prefrontal cortex (PFC); 2) projections to the thalamus, that stimulate non-specific thalamocortical glutamatergic neurons (Jones, 2011). The cholinergic PPT and LDT nuclei are highly active during wakefulness and REM sleep, but not during SWS (Jones, 2005). The main noradrenergic nucleus, the LC, maximally discharges during active wakefulness and is almost silent during both REM and NREM sleep (Aston-Jones and Bloom, 1981). The simultaneous presence of acetylcholine (ACh) and norepinephrine (NE) is necessary to sustain the waking state through cortical activation and muscle tone (Jones, 2005), while, during REM sleep, ACh release largely prevails and muscle tone is absent. The serotonergic dorsal raphe nucleus (DR) seems to be implicated in less-aroused waking states (Jacobs and Fornal, 1991), while the dopaminergic median raphe nucleus stimulates arousal related to positive emotions during wakefulness and REM sleep (Maloney et al. 2002). Histaminergic cells, located in the posterior hypothalamus, also contribute to arousal and wakefulness (Saper et al. 2001). Orexinergic hypothalamic neurons exert a global control of arousal by innervating most of the above-mentioned nuclei as well as sending direct projections to the PFC. Orexin neurons mainly discharge during active wakefulness and regulate a variety of functions, ultimately

sustaining the exploratory and goal-oriented behaviours driven by physiological needs (Lee et al. 2005; Lőrincz & Adamantidis, 2017; Jones, 2020).

Because of such a complex pattern of reciprocal connections accompanied by direct neuromodulation of the neocortex (Jones, 2005; Saper & Fuller, 2017; Scammell, Arrigoni & Lipton, 2017), each EEG rhythm is generated by a sophisticated interplay of local cortical and deep subcortical oscillators. Examples are the thalamocortical interplay underlying SWS δ activity (Crunelli et al. 2015) and the sleep spindle generation in NREM stage 2 (Fernandez & Lüthi, 2020).

Sleep disorders and sleep-related diseases as rhythmopaties

Any defect or alteration of the brain ascending modulatory system may impact on its ability to generate and/or sustain rhythms and thus affect the regulation and stability of sleep/wake and behavioural states. A pathological alteration of brain rhythm generators can also cause cognitive consequences. This has been extensively studied in the context of epilepsy, in which a dysfunctional circuitry produces abnormal activity and rhythm regulation, giving rise to seizures. In this light, epilepsy can be fully defined as a rhythmopathy, that is a disease of brain rhythm (Shuman,

Amendolara & Golshani, 2017). Moreover, some sleep disorders and sleep-related diseases have been shown to be linked to malfunction of the brain ascending regulatory system, and to display alteration of some rhythmic activity related to the sleep/wake homeostasis (Chokroverty, 2010).

The two diseases I am going to focus on belong to this group: Autosomal Dominant Sleep-related Hypermotor Epilepsy (ADSHE), often linked to cholinergic dysfunction, and narcolepsy with cataplexy (NC), caused by orexin deficiency. Both ADSHE and narcolepsy can be defined as rhythmopaties, since their defining symptoms are dysfunctions of brain activity rhythm (nocturnal focal seizures in ADSHE, and abnormal EEG/EMG activity during cataplexy in NC). Both are associated to alteration of an “ARAS” neurotransmitter system. In both, the neorological and cognitive impact of the disease is closely linked to the abnormal rhythmogenesis events.

Aim of the thesis

My aim is to characterize the pathogenesis of ADSHE (Part I) and NC (Part II), considered as rhythmopaties linked to dysfunction of the brain ascending regulatory system. Especially, I have investigated the molecular and cellular substrates of the dysfunctional rhythmic activity at the

microcircuit level, with a particular focus on neocortex and ventral tegmental area.

In chapter 2, I will describe the functional alterations of nicotinic acetylcholine receptors (nAChR) containing the $\alpha2^{Tyr252His}$ mutant subunit linked to ADSHE. When expressed in HEK293 cells, the mutation caused a loss-of-function of the channel by drastically reducing the maximal currents in response to saturating concentrations of the agonists in both the α2β4 and α2β2 nAChR subtypes. The effect was caused by a strong right-shift of the concentration-response curve, not paralleled by a decrease in receptor expression. This work sheds some light on the role of mutant α2 nAChR subunits linked to ADSHE, which may underlie a novel pathogenetic mechanism, involving the dysfunction of cortical layer V Martinotti SOM^+ interneurons (see chapter 3).

Moreover, we studied the effects of another mutation (Appendix), $\alpha2^{Arg121Leu}$, found in a patient affected by Autosomal Dominant Lateral Temporal Lobe Epilepsy (ADLTE). Also in this case, the data point to a reduction in channel functionality: it is, thus, likely that CHRNA2-affecting mutations are more commonly linked to epileptic syndromes than previously thought, especially loss-of-function ones, pointing to a specific implication of α2-expressing neurons in cortical rhythmogenesis.

In chapter 3 I will report the morpho-functional alterations in the prefrontal cortex layer V of mice conditionally expressing the ADSHE-linked $\beta2^{V287L}$ subunit. Its expression was correlated to minor morphological alterations in pyramidal neurons' (Py) dendritic ramification, as well as to a ~10% decrease of prefrontal cortex thickness. Moreover, mutant mice showed larger somatic nicotinic currents in regular spiking SOM^{+} interneurons insensitive to serotonin (largely Martinotti cells). These results may explain why seizures may be facilitated by the low cholinergic tone typical of NREM sleep and why nicotine administration can be palliative in patients.

In chapter 4 I will show the effective functional deletion of Ox2R in the Ox2R-Δ mice, created by our colleague Dr. Anne Vassalli (University of Lausanne) and based on the Cre-lox recombination technology. I also assessed if the Ox2R-flox mice had functionally equivalent Ox2R as C57BL6/J control mice. The responses to Ox2R agonists of the classical Ox2R-expressing neuronal type – the histaminergic neurons of the ventral tuberomammillary nucleus of the hypothalamus – were recorded by whole-cell patch-clamp. Overall, the data confirm the functional equivalence of Ox2Rs in control and Ox2R-flox mice, as well as its functional ablation in Ox2R-Δ mice, validating this mouse model as a reliable tool to dissect the specific function of Ox2R in the cerebral circuits.

In chapter 5 I will describe the orexinergic neuromodulation of Py and interneuronal microcircuits of the dorso-lateral (Fr2) and medial PFC, especially in layer V. Orexins showed to have an excitatory effect on Fr2 layer V pyramidal neurons, which is mainly mediated by Ox1Rs, and probably representing a mostly presynaptic contribution. To this, a postsynaptic effect adds up, only partly depending on the activation of L-type Ca_V channels. On the other hand, OrxB and OrxB-AL do not seem to be strongly involved in the excitatory transmission regulation on Pys, suggesting a secondary role for Ox2Rs. The preliminary histological assays showed that the Ox2R has a diffuse distribution both on putative cell bodies and in the neuropil, and that SOM^+ interneurons seem to be both more densely innervated by orexinergic fibres and have a higher Ox2R expression than PV^+ ones. These results are in line with the hypothesis that orexins could regulate rhythmogenesis in the PFC at frequencies around the θ band, with the involvement of SOM^+ interneurons. Since hypersynchronous paroxysmal θ activities are highly enriched during cataplexy in orexin knockout mice and narcoleptic children, especially in the frontal cortex, this could enlighten some possible mechanisms for cataplexy occurrence in narcoleptic patients.

In chapter 6 we established the proper experimental conditions to investigate the network and cellular

mechanisms underlying the θ rhythm increase recorded during wakefulness in mice lacking Ox2R in DA cells. To do this, I studied the firing activity in the VTA-hippocampal pathway, by using horizontal slices laid onto high-density multi-electrode array dishes. Global burst activity could be followed for a few hours, in different experimental conditions, in $Ox2R^{Dat\text{-}CKO}$ and the $Ox2R^{flox/flox}$ controls. Preliminary results suggest that OrxB tends to inhibit global firing in $Ox2R^{flox/flox}$ slices, whereas the effect is excitatory in $Ox2R^{Dat\text{-}CKO}$, suggesting that the increased θ activity in the latter may depend on a relief of an inhibitory effect produced by Ox2Rs on firing activity of the VTA-hippocampal pathway. Preliminary patch-clamp experiments on VTA^{DA} cells are consistent with this hypothesis.

References

Allada, R., & Siegel, J. M. (2008). Unearthing the phylogenetic roots of sleep. Current biology, 18, R670-R679.

Aston-Jones, G., & Bloom, F. (1981). Activity of norepinephrine-containing locus coeruleus neurons in behaving rats anticipates fluctuations in the sleep-waking cycle. Journal of Neuroscience, 1, 876-886.

Brown, R. E., Basheer, R., McKenna, J. T., Strecker, R. E., & McCarley, R. W. (2012). Control of sleep and wakefulness. Physiological reviews, 92, 1087-1187

Buzsaki, G. (2006). Rhythms of the Brain. Oxford university press.

Chokroverty, S. (2010). Overview of sleep & sleep disorders. Indian J Med Res, 131, 126-140.

Cirelli, C., & Tononi, G. (2008). Is sleep essential? PLoS biology, 6, e216.

Crunelli, V., David, F., Lőrincz, M. L., & Hughes, S. W. (2015). The thalamocortical network as a single slow wave-generating unit. Current opinion in neurobiology, 31, 72-80.

Eban-Rothschild, A., Appelbaum, L., & de Lecea, L. (2018). Neuronal mechanisms for sleep/wake regulation and modulatory drive. Neuropsychopharmacology, 43, 937-952.

Edlow, B. L., Haynes, R. L., Takahashi, E., Klein, J. P., Cummings, P., Benner, T., ... & Folkerth, R. D. (2013). Disconnection of the ascending arousal system in traumatic coma. Journal of Neuropathology & Experimental Neurology, 72, 505-523.

Fernandez, L. M., & Lüthi, A. (2020). Sleep spindles: mechanisms and functions. Physiological reviews, 100, 805-868.

Jacobs, B. L., & Fornal, C. A. (1991). Activity of brain serotonergic neurons in the behaving animal. Pharmacological reviews, 43, 563-578.

Jones, B. E. (2005). From waking to sleeping: neuronal and chemical substrates. Trends in pharmacological sciences, 26, 578-586.

Jones, B. E. (2011). Neurobiology of waking and sleeping. Handbook of clinical neurology, 98, 131-149.

Kovalzon, V. M. (2016). Ascending reticular activating system of the brain. Translational Neuroscience and Clinics, 2, 275-285.

Lee, M. G., Hassani, O. K., & Jones, B. E. (2005). Discharge of identified orexin/hypocretin neurons across the sleep-waking cycle. Journal of Neuroscience, 25, 6716-6720.

Lindsley, D. B., Bowden, J. W., & Magoun, H. W. (1949). Effect upon the EEG of acute injury to the brain stem activating system. Electroencephalography and clinical neurophysiology, 1, 475-486.

Lőrincz, M. L., & Adamantidis, A. R. (2017). Monoaminergic control of brain states and sensory processing: Existing knowledge and

recent insights obtained with optogenetics. Progress in neurobiology, 151, 237-253.

Maloney, K. J., Mainville, L., & Jones, B. E. (2002). c-Fos expression in dopaminergic and GABAergic neurons of the ventral mesencephalic tegmentum after paradoxical sleep deprivation and recovery. European Journal of Neuroscience, 15, 774-778.

Moruzzi, G., & Magoun, H. W. (1949). Brain stem reticular formation and activation of the EEG. Electroencephalography and clinical neurophysiology, 1, 455-473.

Saper, C. B., Chou, T. C., & Scammell, T. E. (2001). The sleep switch: hypothalamic control of sleep and wakefulness. Trends in neurosciences, 24, 726-731.

Saper, C. B., Fuller, P. M., Pedersen, N. P., Lu, J., & Scammell, T. E. (2010). Sleep state switching. Neuron, 68, 1023-1042.

Saper, C. B., & Fuller, P. M. (2017). Wake–sleep circuitry: an overview. Current opinion in neurobiology, 44, 186-192.

Scammell, T. E., Arrigoni, E., & Lipton, J. O. (2017). Neural circuitry of wakefulness and sleep. Neuron, 93, 747-765.

Shuman, T., Amendolara, B., & Golshani, P. (2017). Theta rhythmopathy as a cause of cognitive disability in TLE. Epilepsy currents, 17, 107-111.

Wijdicks, E. F. (2019). The ascending reticular activating system. Neurocritical care, 31, 419-422.

Zimmerman, J. E., Naidoo, N., Raizen, D. M., & Pack, A. I. (2008). Conservation of sleep: insights from non-mammalian model systems. Trends in neurosciences, 31, 371-376.

PART I. The cholinergic system and the Autosomal Dominant Sleep-related Hypermotor Epilepsy

Sleep-related Hypermotor Epilepsy and ADSHE

Sleep-related Hypermotor Epilepsy (SHE) is a partial epilepsy, characterized by focal seizures generally lasting no longer than two minutes and accompanied by stereotyped motor manifestations with sudden start and termination, mostly occurring during sleep. The minimum estimated incidence of this epilepsy is 1.8/100'000 individuals, meeting the definition of rare disease, but some patients may be misdiagnosed with other sleep disorders (Nobili et al. 2014). SHE affects both sexes and seizures often (but not necessarily) arise in childhood and adolescence. In the most severe cases, crises persist with high frequency (every night or every two), if not treated (Tinuper et al. 2016).

Seizures occur primarily during NREM sleep, particularly during N2 phase, during which the prevailing EEG rhythms are α (8-13 Hz) and β (14-30 Hz). N2 is also characterized by a progressive conversion of the thalamo-cortical transmission mode from single-spiking to bursting, which is linked to the appearance of the K complexes, large waves of depolarization followed by a rapid hyperpolarization, and of

sleep spindles, 12-16 Hz wave trains which last about two seconds (Siegel, 2002).

The semiology of hyperkinetic crises is varied. In some patients, a continuous spectrum of episodes is observed with increasing duration and severity during the single night. In general, the motor events are often preceded by a K complex and can be accompanied by vocalizations, fearful and strong emotional manifestations, autonomic activation (Tinuper et al. 2005). This symptomatology has been associated with epileptic foci located in the frontal and prefrontal, but also temporal and insular cortex, especially for more organized and strong motor attacks with emotional components. Symptomatic forms of SHE are also known, often associated with type II focal cortical dysplasia (Nobili et al. 2014).

The mendelian form of SHE, ADSHE, was defined as a unitary clinical disorder in the mid-1990s on the basis of a study carried out on five families from Australia, UK and Canada showing autosomal dominant inheritance pattern, a clinical phenotype of partial seizures and an incomplete penetrance (between 60 and 80%; Scheffer et al. 1995). The risk of misdiagnosis was immediately clear, due to the heterogeneity of symptoms in the individual patient or the different severity of the phenotype in the affected members of the same family. Another confounding element is the

similarity with the symptoms of other neurological or psychiatric conditions, such as benign nocturnal parasomnias, familial dyskinesias and pseudo-epileptic manifestations of hysteria (Scheffer et al. 1995).

The frontal origin of the seizures is mainly inferred from the seizure symptomatology, because only half of the patients show explicit EEG abnormalities in correspondence of the frontal lobes and a limited number of them is positive for frontal alterations when examined by functional imaging. Indeed, it was noted that ADSHE seizures can originate from the insula and can also expand to involve subcortical areas that disinhibit, in turn, automatic motor patterns (Ryvlin et al. 2006).

The first gene found to be linked to ADSHE is CHRNA4, coding for the α4 subunit of ACh nicotinic receptor (Steinlein et al. 1995). Subsequently ADSHE mutations were also found on CHRNB2 and CHRNA2, respectively coding for the β2 and α2 nAChR subunits. More recently other ADSHE genes were identified. The strongest evidence regards the subunit 1 of the sodium activated potassium channel (KCNT1), and the protein 5 containing the Disheveled domain, Egl-10 and Pleckstrin (DEPD5) (Nobili et al. 2014; Becchetti et al. 2015).

Mutations on CHRNA4, CHRNB2 or CHRNA2 are reported in 10-15% of ADSHE families and despite having different

effects on the ion channel functionality, they lead to rather homogeneous clinical symptoms, sometimes associated to mental retardation of varying severity (Ryvlin et al. 2006). Although there is a considerable body of knowledge on the different nAChR mutations, the pathogenetic mechanism remains unclear, especially regarding why seizures predominantly occur in the frontal lobe during NREM sleep and why they begin in childhood (Sutor et al. 2001; Combi et al. 2004).

However, patients bearing mutations in CHRNA4 or CHRNB2 showed an increase in the density of α4β2* nAChR by PET in the epithalamus, in the ventral midbrain and in the cerebellum, while a decrease was observed in the right dorsolateral prefrontal region. The right orbitofrontal cortex also appears to suffer from hypometabolism in patients compared to controls, indicating some disease-specific alterations in the PFC.

The first-line pharmacological treatment for ADSHE therapy is carbamazepine, a dibenzoazepine anticonvulsant that acts at different levels on neuronal excitability, i.e. reducing the frequency of action potentials by delaying the inactivation recovery of the voltage-gated sodium channels, inhibiting voltage-gated calcium channels and enhancing $GABA_A$ function. Carbamazepine also inhibits the α4β2, α2β2 and

α2β4* nAChRs, probably by open-channel block. Mutant subunits often show greater affinity for the drug compared to wild type ones (Picard et al. 1999). An alternative to carbamazepine is oxcarbazepine, which avoids the side effects associated with the metabolites of carbamazepine (Di Resta et al. 2010). However, 30% of patients have drug-resistant seizures. Only a fraction of these cases can be treated by surgical removal of the epileptic focus (Nobili et al. 2014).

The cholinergic system

The cholinergic system is composed of the neurons of the deep cholinergic nuclei, which are choline acetyl-transferase positive ($ChAT^+$), and sparse cholinergic neurons, that are intermingled between other neurochemically heterogeneous neurons in various regions, from the cortices to the striatum, and seem to have long range projections (Schäfer et al. 1996; Kandel et al. 2013). The deep cholinergic nuclei are the pedunculopontine, PPT, and laterodorsal tegmental, LDT, nuclei of the brainstem, and the magnocellular nucleus of the basal forebrain, BF. The basal forebrain nuclei innervate several paleo- and neocortical areas, the limbic system, the amygdala and the hippocampus (Mesulam et al. 1983), whereas the PPT and the LDT mainly project to the thalamus and the neocortex (densely to the PFC).

ACh enhances cortical arousal and regulates executive as well as cognitive functions, like the execution of attentive tasks, working memory and decision-making (Wallace and Bertrand, 2013). The PPT/LDT nuclei are typically active during wakefulness and at the transition between slow-wave and REM sleep (Jones et al. 2008; Lee et al. 2005; Siegel, 2002), while they are silent during NREM sleep. Therefore, the ACh stimulation of cortex is related to cognitive arousal rather than to behavioural or motor activity.

The cholinergic projections diffusely innervate large target areas and rarely end in proper synaptic contacts. Varicose axon arborisations contribute to diffuse volume transmission (Descarries et al. 1997), which modulates neurotransmitter release and somatic excitability of selected neuronal populations (Jing et al. 2018). ACh cooperates with the other neurotransmitters to finely control cortical rhythms (Couey et al. 2007; Jones et al. 2008) and the switch between different sleep states (Saper et al. 2010).

The prefrontal cortex (PFC) as a cholinergic innervation target

The human prefrontal cortex integrates the emotional salience of events, elaborates complex motor schemes, performs cognitive functions and processes, such as working memory, decision-making and planning of goal-oriented

behaviours (Fuster and Bressler, 2015; Hoover and Vertes, 2007). The rodents' PFC consists of the frontal region 2 (Fr2), the anterior cingulate cortex (ACC), the prelimbic (PrL) and the infralimbic (IL) area, that may also be generically named medial PFC (mPFC). Fr2, also known as secondary motor (M2) cortex (Franklin et al. 2011), could be particularly relevant in the context of ADSHE, whose typical hypermotor events suggest disinhibition of subcortical motor patterns. Fr2 is an associative cortex with premotor control functions and is considered homologous to the much larger human dorsolateral cortex (Uylings et al. 2003). It receives input from the primary motor and somatosensory cortices, and from subcortical structures as the thalamic and brain stem nuclei (Heidbreder and Groenewegen, 2003; Steriade and McCarley, 2005). It also projects to the primary motor cortex and to the dorsomedial striatum (Condé et al. 1995; Paxinos, 2015) and is especially involved in goal-oriented behaviour (Kargo et al. 2007).

In general, neocortical layer V is especially susceptible to develop epileptiform activity, at least in vitro (Telfeian and Connors, 1998). In Fr2, the thick layer V is characterized by large pyramidal cells with extensive apical dendrites that span through the superficial layers. These neurons constitute the main output channel to the subcortical regions, and they are tightly controlled by a dense network of GABAergic

interneurons (Ozeki et al. 2009; Shu et al. 2003). Two major GABAergic populations are those constituted by the parvalbumin-expressing fast-spiking (FS) interneurons, implicated in feed-back and feed-forward inhibition (e.g., Tremblay et al. 2016) and the somatostatin-expressing regular-spiking (RS) interneurons, involved in Py disinhibition and synchronization (Hilscher, et al. 2017; Jiang et al. 2015).

In general, the PFC local circuits are tightly controlled by the ascending regulatory systems, as PFC is anatomically connected with virtually all the neuromodulatory relays (Dembrow and Johnston, 2014). Overall, the cholinergic input produces excitatory effects through both muscarinic and nicotinic receptors, but the important contribution of the latter is increasingly recognized. A common effect is an increase in the excitatory post-synaptic current (EPSC) frequency in layer V and VI, suggesting higher glutamate release from presynaptic intracortical and thalamocortical terminals expressing α4 and β2* nAChR subunits. These excitatory effects seem to be present also in layer II-III Pys, at least in rats (Vidal e Changeux, 1993; Lambe et al. 2003; Kassam et al. 2008; Aracri et al. 2013). Besides expression on presynaptic terminals, PFC Pys can also express nAChRs on the soma, although the balance of nAChR subtypes expressed in different layers and species at different ages is still matter of debate (Couey et al. 2007; Kassam et al. 2008;

Zolles et al. 2009; Poorthuis et al. 2013). The inhibitory transmission on Pys is also increased by ACh, as inhibitory PSCs (IPSCs) frequency is increased in both layer II-III and V Pys (but not layer VI; Poorthuis et al. 2013). Some of these effects can be simply explained by an increased excitatory drive of FS neurons, which follows Py neuron excitation.

However, in layer V, reciprocal inhibition between distinct interneuronal classes has also been observed to be stimulated by α4β2* nAChR activation, which could produce a further excitatory effect by local disinhibition (Aracri et al. 2010). This suggests that nAChRs are also expressed by inhibitory interneurons, although evidence is still fragmentary. Layer V FS interneurons express α4β2* receptors in FVB mice, but not in C57BL6. However, in the latter strain, α7* have been identified in about half of the cells. LTS and RS interneurons in layer V express both receptor subtypes, although not in 100% of the cells. In layer II-III, on the other hand, the non-fast-spiking interneurons show a heterogeneous pattern of α4β2* and α7* nAChRs, and the FS express α7* receptors in 70% of cases (Couey et al. 2007; Poorthuis et al. 2013; Aracri et al. 2017). The contribution of other subunits, such as α2, is still uncertain (see Chapter 3).

The overall effect of ACh on the network was studied in slices of PFC using two-photon fluorescence imaging of calcium

transients, with single cell resolution: ACh induces a generalized increase in activity in all cortical layers through the β2* receptors, particularly in layer VI. More precisely, the activity of interneurons is increased uniformly, while in layers V and VI the activity of pyramidal neurons is the most affected one (Poorthuis et al. 2013).

References

Aracri, P., Consonni, S., Morini, R., Perrella, M., Rodighiero, S., Amadeo, A., & Becchetti, A. (2010). Tonic modulation of GABA release by nicotinic acetylcholine receptors in layer V of the murine prefrontal cortex. Cerebral Cortex, 20, 1539-1555.

Aracri, P., Amadeo, A., Pasini, M. E., Fascio, U., & Becchetti, A. (2013). Regulation of glutamate release by heteromeric nicotinic receptors in layer V of the secondary motor region (Fr2) in the dorsomedial shoulder of prefrontal cortex in mouse. Synapse, 67, 338-357.

Aracri, P., Meneghini, S., Coatti, A., Amadeo, A., & Becchetti, A. (2017). α4β2∗ nicotinic receptors stimulate GABA release onto fast-spiking cells in layer V of mouse prefrontal (Fr2) cortex. Neuroscience, 340, 48-61.

Becchetti, A., Aracri, P., Meneghini, S., Brusco, S., & Amadeo, A. (2015). The role of nicotinic acetylcholine receptors in autosomal dominant nocturnal frontal lobe epilepsy. Frontiers in physiology, 6, 22.

Combi, R., Dalprà, L., Tenchini, M. L., & Ferini-Strambi, L. (2004). Autosomal dominant nocturnal frontal lobe epilepsy. Journal of neurology, 251, 923-934.

Condé, F., Maire-lepoivre, E., Audinat, E., & Crepel, F. (1995). Afferent connections of the medial frontal cortex of the rat. II. Cortical and subcortical afferents. Journal of Comparative Neurology, 352, 567-593.

Couey, J. J., Meredith, R. M., Spijker, S., Poorthuis, R. B., Smit, A. B., Brussaard, A. B., & Mansvelder, H. D. (2007). Distributed network actions by nicotine increase the threshold for spike-timing-dependent plasticity in prefrontal cortex. Neuron, 54, 73-87.

Dembrow, N., & Johnston, D. (2014). Subcircuit-specific neuromodulation in the prefrontal cortex. Frontiers in neural circuits, 8, 54.

Descarries, L., Gisiger, V., & Steriade, M. (1997). Diffuse transmission by acetylcholine in the CNS. Progress in Neurobiology, 53, 603-625.

Di Resta, C., Ambrosi, P., Curia, G., & Becchetti, A. (2010). Effect of carbamazepine and oxcarbazepine on wild-type and mutant neuronal nicotinic acetylcholine receptors linked to nocturnal frontal lobe epilepsy. European journal of pharmacology, 643, 13-20.

Franklin, K. J. B., Chudasama, Y., Watson, C., Paxinos, G., & Puelles, L. (2011). The prefrontal cortex. In: The Mouse Nervous System, 727-735.

Fuster, J. M., & Bressler, S. L. (2015). Past makes future: role of pFC in prediction. Journal of cognitive neuroscience, 27, 639-654.

Heidbreder, C. A., & Groenewegen, H. J. (2003). The medial prefrontal cortex in the rat: evidence for a dorso-ventral distinction based upon functional and anatomical characteristics. Neuroscience & Biobehavioral Reviews, 27, 555-579.

Hoover, W. B., & Vertes, R. P. (2007). Anatomical analysis of afferent projections to the medial prefrontal cortex in the rat. Brain Structure and Function, 212, 149-179.

Jiang, X., Shen, S., Cadwell, C. R., Berens, P., Sinz, F., Ecker, A. S., ... & Tolias, A. S. (2015). Principles of connectivity among morphologically defined cell types in adult neocortex. Science, 350.

Jing, M., Zhang, P., Wang, G., Feng, J., Mesik, L., Zeng, J., ... & Li, Y. (2018). A genetically encoded fluorescent acetylcholine indicator for in vitro and in vivo studies. Nature biotechnology, 36, 726-737.

Jones, B. E. (2008). Modulation of cortical activation and behavioral arousal by cholinergic and orexinergic systems. Annals of the New York Academy of Sciences, 1129, 26-34.

Kandel, E. R., Schwartz, J. H., Jessell, T. M., Siegelbaum, S., Hudspeth, A. J., & Mack, S. (Eds.). (2000). Principles of neural science (Vol. 4, pp. 1227-1246). New York: McGraw-Hill.

Kargo, W. J., Szatmary, B., & Nitz, D. A. (2007). Adaptation of prefrontal cortical firing patterns and their fidelity to changes in action–reward contingencies. Journal of Neuroscience, 27, 3548-3559.

Kassam, S. M., Herman, P. M., Goodfellow, N. M., Alves, N. C., & Lambe, E. K. (2008). Developmental excitation of corticothalamic neurons by nicotinic acetylcholine receptors. Journal of Neuroscience, 28, 8756-8764.

Lambe, E. K., Picciotto, M. R., & Aghajanian, G. K. (2003). Nicotine induces glutamate release from thalamocortical terminals in prefrontal cortex. Neuropsychopharmacology, 28, 216-225.

Lee, M. G., Hassani, O. K., & Jones, B. E. (2005). Discharge of identified orexin/hypocretin neurons across the sleep-waking cycle. Journal of Neuroscience, 25, 6716-6720.

Mesulam, M. M., Mufson, E. J., Levey, A. I., & Wainer, B. H. (1983). Cholinergic innervation of cortex by the basal forebrain: cytochemistry and cortical connections of the septal area, diagonal band nuclei, nucleus basalis (substantia innominata), and hypothalamus in the rhesus monkey. Journal of Comparative Neurology, 214, 170-197.

Nobili, L., Proserpio, P., Combi, R., Provini, F., Plazzi, G., Bisulli, F., ... & Tinuper, P. (2014). Nocturnal frontal lobe epilepsy. Current neurology and neuroscience reports, 14, 424.

Ozeki, H., Finn, I. M., Schaffer, E. S., Miller, K. D., & Ferster, D. (2009). Inhibitory stabilization of the cortical network underlies visual surround suppression. Neuron, 62, 578-592.

Paxinos, G. (2015). Brain, behaviour and evolution. In *GeNeDis 2014* (pp. 1-1). Springer, Cham.

Picard, F., Bertrand, S., Steinlein, O. K., & Bertrand, D. (1999). Mutated nicotinic receptors responsible for autosomal dominant nocturnal frontal lobe epilepsy are more sensitive to carbamazepine. Epilepsia, 40, 1198-1209.

Picard, F., Bruel, D., Servent, D., Saba, W., Fruchart-Gaillard, C., Schöllhorn-Peyronneau, M. A., ... & Bottlaender, M. (2006). Alteration of the in vivo nicotinic receptor density in ADNFLE patients: a PET study. Brain, 129, 2047-2060.

Poorthuis, R. B., Bloem, B., Schak, B., Wester, J., de Kock, C. P., & Mansvelder, H. D. (2013). Layer-specific modulation of the prefrontal cortex by nicotinic acetylcholine receptors. Cerebral cortex, 23, 148-161.

Ryvlin, P., Rheims, S., & Risse, G. (2006). Nocturnal frontal lobe epilepsy. Epilepsia, 47, 83-86.

Schäfer, M. K. H., Weihe, E., Erickson, J. D., & Eiden, L. E. (1995). Human and monkey cholinergic neurons visualized in paraffin-embedded tissues by immunoreactivity for VAChT, the vesicular acetylcholine transporter. Journal of Molecular Neuroscience, 6, 225-235.

Scheffer, I. E., Bhatia, K. P., Lopes-Cendes, I., Fish, D. R., Marsden, C. D., Andermann, E., ... & Berkovic, S. F. (1995). Autosomal dominant nocturnal frontal lobe epilepsy: a distinctive clinical disorder. Brain, 118, 61-73.

Shu, Y., Hasenstaub, A., & McCormick, D. A. (2003). Turning on and off recurrent balanced cortical activity. Nature, 423, 288-293.

Siegel, J. (2002). The neural pathways that produce arousal. The Neural Control of Sleep and Waking, 47-52.

Steinlein, O. K., Mulley, J. C., Propping, P., Wallace, R. H., Phillips, H. A., Sutherland, G. R., ... & Berkovic, S. F. (1995). A missense mutation in the neuronal nicotinic acetylcholine receptor α4 subunit is associated with autosomal dominant nocturnal frontal lobe epilepsy. Nature genetics, 11, 201-203.

Steriade, M., & McCarley, R. W. (2005). Synchronized brain oscillations leading to neuronal plasticity during waking and sleep states. Brain control of wakefulness and sleep, 255-344.

Sutor, B., & Zolles, G. (2001). Neuronal nicotinic acetylcholine receptors and autosomal dominant nocturnal frontal lobe epilepsy: a critical review. Pflügers Archiv, 442, 642-651.

Telfeian, A.E., & Connors, B.W. (1998). Layer-specific pathways for the horizontal propagation of epileptiform discharges in neocortex. Epilepsia 39, 700-708.

Tinuper, P., Provini, F., Bisulli, F., & Lugaresi, E. (2005). Hyperkinetic manifestations in nocturnal frontal lobe epilepsy. Semeiological features and physiopathological hypothesis. Neurological Sciences, 26, s210-s214.

Tinuper, P., Provini, F., Bisulli, F., & Lugaresi, E. (2005). Hyperkinetic manifestations in nocturnal frontal lobe epilepsy. Semeiological features and physiopathological hypothesis. Neurological Sciences, 26, s210-s214.

Tremblay, R., Lee, S., & Rudy, B. (2016). GABAergic interneurons in the neocortex: from cellular properties to circuits. Neuron, 91, 260-292.

Uylings, H. B., Groenewegen, H. J., & Kolb, B. (2003). Do rats have a prefrontal cortex? Behavioural Brain Research, 146, 3-17.

Vidal, C., & Changeux, J. P. (1993). Nicotinic and muscarinic modulations of excitatory synaptic transmission in the rat prefrontal cortexin vitro. Neuroscience, 56, 23-32.

Wallace, T. L., & Bertrand, D. (2013). Importance of the nicotinic acetylcholine receptor system in the prefrontal cortex. Biochemical pharmacology, 85, 1713-1720.

Zolles, G., et al. (2009). Functional expression of nicotinic acetylcholine receptors in rat neocortical layer 5 pyramidal cells. Cereb Cortex 19, 1079-1091.

Chapter 2. CHRNA2 and nocturnal frontal lobe epilepsy: Identification and characterization of a novel loss of function mutation

The work presented in this chapter is an extract of the following paper:

Villa[1], C., Colombo[1], G., Meneghini, S., Gotti, C., Moretti, M., Ferini-Strambi, L., Chisci, E., Giovannoni, R., Becchetti, A., & Combi, R. (2019).

CHRNA2 and nocturnal frontal lobe epilepsy: Identification and characterization of a novel loss of function mutation.

Frontiers in Molecular Neuroscience, 12:17.

[1] These authors have contributed equally to this work

Abstract

Among ADSHE-linked mutations, some are found on CHRNA2, two of which have been previously characterized by our group (Conti et al. 2015; Aridon et al. 2006). They have contrasting functional effects, so we have continued to work on newly identified mutations on the same gene, to better define the pathogenic potential of altered α2* nAChR function.

By transient co-expression of α2 and $\alpha2^{Tyr252His}$ with either β2 or β4 in human embryonic kidney (HEK) cells, we assessed that the mutation reduced the maximal currents by approximately 80% in response to saturating concentrations of nicotine in homo- and heterozygous form, in both the α2β4 and α2β2 nAChR subtypes. The effect was caused by a strong right-shift of the concentration-response to nicotine, and was also observed with ACh. Negligible effects were produced by $\alpha2^{Tyr252His}$ on the current reversal potential. Moreover, a binding assay revealed an approximately 10-fold decrease of both affinity and total binding in cells expressing α2Tyr252His, which was not caused by a decrease in receptor expression. We concluded that mutations in CHRNA2 are more commonly linked to ADSHE than previously thought, and may cause a loss-of-function phenotype (Villa et al. 2019).

After this study, we also characterized other CHRNA2 mutations linked to epileptic syndromes. Firstly, we considered the $\alpha2^{Arg121Leu}$ mutated subunit, identified by Carlo Nobile and colleagues (CNR, Padua) as linked to Autosomal Dominant Lateral Temporal Lobe Epilepsy (ADLTE). In homozygous condition, $\alpha2^{Arg121Leu}$ decreased the peak current density evoked by saturating nicotine by ~40% (α2β2) or ~25% (α2β4), without altering the current reversal potential. As the current reduction is less marked when the nAChR

response is activated by ACh, our data only partly suggest that loss-of-function mutations in CHRNA2 could be associated with ADLTE.

We continued with the study of the mutated $\alpha2^{Leu313Phe}$ subunit found in a de novo case of epileptic encephalopathy with nocturnal seizures, characterized by a very early onset at four months of age. In the α2β4 subunit composition, the $\alpha2^{Leu313Phe}$* channels – both the pseudo-heterozygote and the fully mutant – had a strongly reduced current density at saturating nicotine concentrations: the maximal current density, evoked by 100 µM nicotine, was reduced by 71% in $\alpha2^{Leu313Phe}$β4* channels and by 48 % in $\alpha2^{Leu313Phe}$α2β4* channels compared to wild type α2β4 nAChRs. No alterations in the current kinetics have been found, indicating unaltered gating dynamics.

It seems, thus, likely that CHRNA2-affecting mutations are more commonly linked to epileptic syndromes than previously thought, especially loss-of-function ones, pointing to a specific implication of α2-expressing neurons in cortical rhythmogenesis.

Introduction

Autosomal dominant sleep-related hypermotor epilepsy (ADSHE) (Tinuper et al. 2016) is a familial idiopathic focal epilepsy with increased nocturnal instability (Sansoni et al.

2013), characterized by a wide spectrum of brief stereotyped hypermotor seizures, mostly occurring during non-rapid eye movement (NREM) sleep. About the 80% of individuals develop ADSHE in the first two decades of life and mean age of onset is 10 years (Nobili et al. 2014; Tinuper et al. 2016). Within a family, the manifestation of the disorder may vary considerably, and no clear difference between sexes is observed.

ADSHE was the first epilepsy to be recognized as a channelopathy, i.e., a disease resulting from ion channel dysfunction, after the identification of the first mutation in the CHRNA4 gene, coding for the a4 nAChR subunit (Steinlein et al. 1995). Subsequently, evidence has grown about the role of nAChRs in the pathophysiology of ADSHE (Ferini-Strambi et al. 2012). Nonetheless, mutations in nAChR genes are rare and the involvement of other genes implicated in ADSHE has been recognized since 2005 (Combi et al. 2005b). In fact, mutations were also found in KCNT1 (coding for a sodium-dependent KC channel) (Heron et al. 2012) as well as in genes not coding for ion channels, such as CRH (corticotropin-releasing hormone) (Combi et al. 2005a) and DEPDC5 (Disheveled, Egl-10 and Pleckstrin Domain-containing protein 5) (Ishida et al. 2013).

The nAChR is a pentameric ion channel formed by various combinations of α and β subunits, which determine the physiological and pharmacological properties of each subtype (Dani and Bertrand, 2007). Most ADSHE mutations of the nAChR were found in the genes coding the α4 (Steinlein et al. 1995), and β2 (De Fusco et al. 2000; Phillips et al. 2001) subunits, in agreement with the prevalence of the α4β2 subtype in the mammalian brain (Zoli et al. 2015). When expressed in *Xenopus laevis* oocytes or mammalian cell lines, mutant subunits tend to confer a gain-of-function phenotype, especially in the simulated heterozygote, because of increased receptor's sensitivity to the agonist or other kinetic alterations (Becchetti et al. 2015). Several hypotheses concerning the nAChR-dependent pathogenetic mechanism have been proposed (Nobili et al. 2014). These are difficult to demonstrate considering that nAChRs are expressed in the brain at pre-, post-, and extra-synaptic locations (Dani and Bertrand, 2007), and they regulate both excitatory and inhibitory transmission (Becchetti et al. 2015). In prefrontal regions, heteromeric nAChRs exert a widespread stimulatory effect on glutamatergic transmission (Vidal and Changeux, 1993; Lambe et al. 2003; Aracri et al. 2013). These receptors also regulate GABAergic interneurons (Porter et al. 1999; Alkondon et al. 2000; Couey et al. 2007) although the expression of heteromeric nAChRs

in these cells is more variable, depending on neuronal subtype and age (Porter et al. 1999; Couey et al. 2007; Aracri et al. 2010, 2017).

Understanding the nAChR-dependent pathogenesis of ADSHE is made even more complex by the involvement of CHRNA2. Two mutations with opposite effects on the channel functioning were previously reported in the CHRNA2 gene, coding for the nAChR α2 subunit. In particular, the p.Ile279Asn increases the receptor sensitivity to the agonists (Aridon et al. 2006), whereas the p.Ile297Phe mutation presents a strongly decreased current density as compared to the WT, but scarce alteration of the conductive properties and the sensitivity to nicotine (Conti et al. 2015). Mutations in the CHRNA2 are rare in the Italian ADSHE population (Combi et al. 2009). Hence, it is important to determine whether CHRNA2 mutations can be a significant etiologic factor in sleep-related hypermotor epilepsy, and what is the prevalent pathogenetic mechanism.

Materials and Methods

Culture and Transfection Procedure

Plasmids expressing wild-type (WT) or mutant α2β2 or α2β4 were transiently transfected in HEK293 cells (TsA subclone; American Type Culture Collection) as reported (Conti et al. 2015). In brief, cells were cultured in DMEM high glucose

(Dulbecco's modified Eagle medium high glucose; Euroclone, Pero, MI, Italy or Merck Life Sciences, Darmstadt, Germany) supplemented with 10% fetal bovine serum (Euroclone, Pero, MI, Italy or Merck Life Sciences, Darmstadt, Germany) and 2 mM L-glutamine, at 30°C and 5% CO2. For patch-clamp experiments, cells were seeded onto 35-mm culture dishes. Transfection was carried out with Lipofectamine 2000 (Life Technologies). To simulate the heterozygous state, equal amounts of WT and mutant plasmids were cotransfected. The DNA concentration in the transfection mixture was 1.33 ng/mL. Cells were incubated with the transfection mixture for 5 h, at 37°C, and kept at 30°C in 5% CO2 during the 24 h preceding the electrophysiological recordings, to enhance the surface receptor density (Cooper et al. 1999).

Patch-Clamp Recordings

Chemicals and drugs for intra- and extracellular solutions were purchased from Merck Life Sciences. The extracellular solution contained (mM): NaCl 130, KCl 5, CaCl2 2, MgCl2 2, HEPES 10, and D-glucose 5 (pH 7.3). Patch pipettes contained (mM): K-gluconate 140, KCl 5, MgCl2 1, BAPTA-KOH 0.5, HEPES 10, NaGTP 0.3, and MgATP 2 (pH 7.3). Stock solutions of nicotine (10 mM) were prepared weekly in our extracellular solution and kept refrigerated; acetylcholine (10 mM) and atropine (1 mM) were dissolved in extracellular solution, aliquoted and frozen until usage. Extracellular

solutions with the appropriate agonist concentration were prepared daily; pH was always checked after nicotine addition.

Whole-cell currents were registered 36–72 h after transfection, with an Axopatch 200B amplifier (Molecular Devices, Sunnyvale, CA, United States), at room temperature. Micropipettes (3–5 MΩ) were pulled from borosilicate capillaries (Corning Inc., NY, United States) with a P-97 Flaming/Brown Puller (Sutter Instruments, Novato, CA, United States). Cell capacitance and series resistance (up to 75%) were always compensated. When necessary, the cell capacitance value thus measured was used to calculate the cell current density (i.e., the peak whole-cell current at a given V_m and agonist concentration was divided by the cell capacitance). Because the cell capacitance is proportional to the cell surface area, the calculated values are proportional to the current per unit area. Fluorescent cells were identified with an inverted Eclipse TE200 microscope (Nikon) equipped with a TEFM epifluorescence attachment. Currents were low-pass-filtered at 2 kHz and acquired online at 10–20 kHz with pClamp 9 hardware and software (Molecular Devices). Drugs were applied with an RSC-160 Rapid Solution Changer (Bio-Logic Science Instruments, Claix, France).

Patch-clamp data were analyzed with OriginPro 9 (OriginLab), as previously described (Brusco et al. 2015). Theoretical curves best fitting the data were calculated by a Levenberg-Marquardt algorithm. The concentration-response data were fitted by using a two-components Hill-type equation (Covernton and Connolly, 2000), as follows:

$$\frac{I_L}{I_{max}} = \frac{A}{1 + \left(\frac{EC_{50high}}{[L]}\right)^{nH1}} + \frac{1 - A}{1 + \left(\frac{EC_{50low}}{[L]}\right)^{nH2}}$$

where I_{max} is the maximal current, I_L is the current at a given concentration L of agonist, A is the fraction of receptors in the high-affinity state; EC_{50high} and EC_{50low} are the agonist concentrations producing the half-maximal effect for the high and low affinity components, respectively; n_{H1} and n_{H2} are the Hill coefficients for the two components.

Statistical Analysis

Data are generally given as mean values ± standard error of the mean, with n representing the number of experiments (tested cells, in the case of patch-clamp experiments). Statistical comparisons between two populations of data were carried out with a Student's t-test for unpaired samples, after checking for data normality (QQ plots) and variance homogeneity (F-test). The Welch correction was applied in case of non-homogeneous variances. Multiple comparisons

were carried out with one-way ANOVA, followed by Tukey post hoc test, after checking for data normality (QQ plots) and variance homogeneity (Levene test). The level of statistical significance was set at $p < 0.05$.

Results

Patient and Mutation

The patient in which this mutation has been found was a 19-year-old right-handed man, referred to the sleep medical unit for nocturnal episodes with abnormal motor-behavioural phenomena occurring several times every night. The episodes started at the age of 13 years and most of them were characterized by sudden vocalization with grunting followed by dystonic posturing; in 2–3 episodes each week a deambulatory behaviour was reported. There was a family history of nocturnal confusional arousals in the mother during her adolescence: confusional arousal episodes occurred in the first part of the night (1–5 episodes for week, from age 13 to 16 years). Scalp EEG monitoring during wakefulness and the contrast-enhanced brain magnetic resonance imaging (MRI) were normal, as well as the neurological examination. The nocturnal video-PSG recording of the patient showed 13 epileptic episodes, 8 in stage N2 and 5 in stage N3, allowing the SHE diagnosis. The EEG before, during and after the episodes did not show any epileptiform activity, but in eight

episodes showed ictal rhythmic slow activity over anterior areas. A marked reduction of the nocturnal episodes was observed with the administration of carbamazepine (600 mg/day, single bedtime dose).

In order to identify possible genetic mutations linked to the disease, the coding regions, intron-exon boundaries and UTRs of CHRNA4, CHRNB2, CHRNA2, CRH, KCNT1 genes, previously associated with ADSHE, were amplified and Sanger sequenced. The patient proved to be heterozygote for a missense mutation in the CHRNA2 gene, consisting of a T>C transition at cDNA position 754 (c.754T>C), which leads to a non-conservative Tyr to His change at position 252 (p.Tyr252His) in the α2 subunit of the nAChR. This variant was not yet reported, and the segregation analysis showed that the mutation was present in the heterozygous state also in the affected proband's mother, qualifying the disease as ADSHE.

The bioinformatic analysis by Polyphen-2, SIFT or MutationTaster, predicted a possible damaging effect on the channel functionality. This would be related to the fact that the mutation causes the substitution in an important functional domain of a polar but not charged amino acid with an aromatic R group (the Tyr) with another (the His) with a positively charged R group.

Mutation effects on the Channel Function

Firstly, we tested if the mutation could affect the transcription of the α2 subunit. To this extent, the correct transcription of the expression vectors in HEK293 cells was verified by RT-PCR. No differences in transcription levels were observed between the WT and mutant CHRNA2 using both tricistronic vectors. In order to determine whether the mutation could affect different level of expression of receptor subtypes, we then performed Western Blotting (WB) analysis by loading on the gel the same amount of membrane proteins. The quantitative analysis of three independent preparations of WT α2β4 and $\alpha2^{Tyr252His}\beta4$ showed that the α2 and β4 subunit content was identical between cells transfected with α2β4 or $\alpha2^{Tyr252His}\beta4$.

Whole-cell currents were elicited at - 60 mV, by using nicotine or ACh. In Primate brain, the expression of α2 largely overlaps with that of both β2 and β4 (Han et al. 2000; Quik et al. 2000). Moreover, there is evidence of in vivo expression of α2β2* (Zoli et al. 2015), α2α4β2* (Quik et al. 2005), and α2β4* (Zoli et al. 1998). Therefore, we studied the functional effects of $\alpha2^{Tyr252His}$ on both α2β4 and α2β2 receptors. Representative current traces obtained from cells expressing α2β4 nAChRs are shown in Figure 2.1.

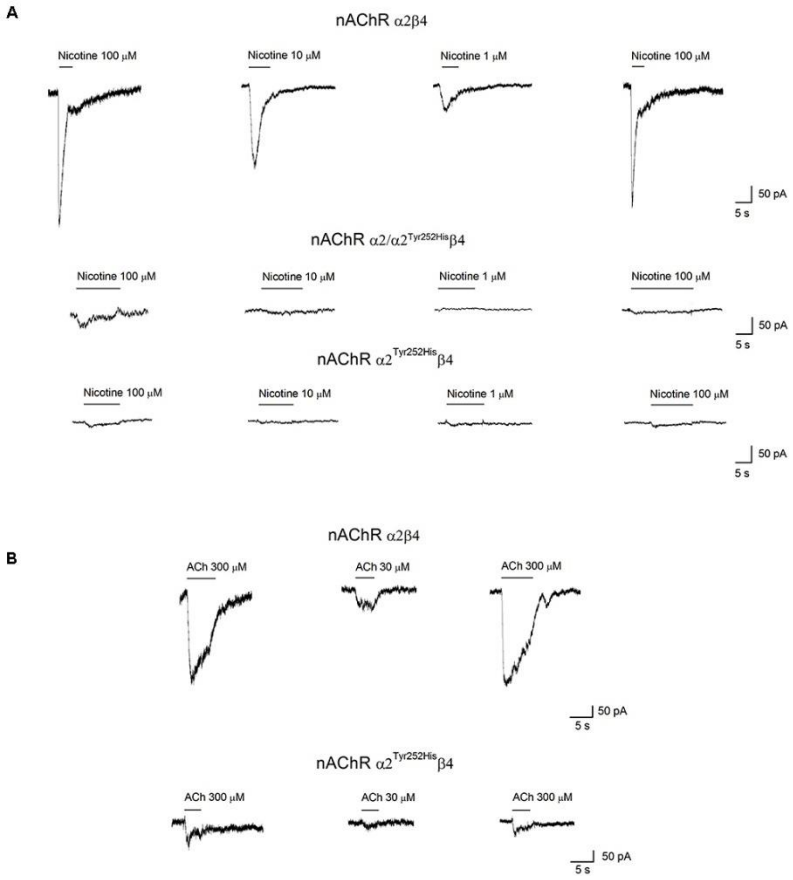

Figure 2.1. Whole-cell currents from nAChR receptors containing or not $\alpha 2^{Tyr252His}$. (A) Representative whole-cell current traces elicited at –60 mV by the indicated concentration of nicotine, in cells expressing α2/β4 (wild type), $\alpha 2^{Tyr252His}$/β4 (homozygote), or α2/ $\alpha 2^{Tyr252His}$/β4 (heterozygote) receptors, as indicated. The bars above the current traces mark the time of nicotine application. The time gaps between consecutive traces represents about 2 min in the absence of agonist. (B) Same as (A), except that ACh was used instead of nicotine, at the indicated concentrations. Cells expressed either α2/β4 (wild type), or $\alpha 2^{Tyr252His}$/β4 (homozygote) receptors.

The maximal currents were repeatedly measured during the experiment, to check for possible activity rundown. Saturating nicotine concentrations (100–300 mM) elicited the typical inward current with desensitization. Consecutive agonist applications were spaced at least 2 min apart, to allow full channel recovery from desensitization. Lower agonist concentrations elicited smaller currents, with a slower desensitization. Similar experiments were carried out on cells expressing $\alpha2^{Tyr252His}\alpha2\beta4$ receptors (simulated heterozygote; Figure 2.1 A, middle panel), or $\alpha2^{Tyr252His}\beta4$ (homozygote; Figure 2.1 A, bottom panel). The receptors containing $\alpha2^{Tyr252His}$ generally presented much lower current amplitudes, compared to the WT. Similar results were obtained by using the physiological agonist ACh, instead of nicotine. Representative current traces are shown in Figure 2.1 B. When using ACh, atropine (1 mM) was added to the extracellular solution, to avoid the possible interference of muscarinic ACh receptors.

Figure 2.2. $\alpha2^{Tyr252His}$ decreases the maximal current density, without altering V_{rev}. (A) Bars represent average peak whole-cell current densities measured at the indicated concentrations of nicotine or ACh, in cells expressing α2β4, $\alpha2^{Tyr252His}\beta4$, or $\alpha2^{Tyr252His}/\alpha2\beta4$. The results of representative measurements are shown for 1 μM nicotine (p = 0.00005 between WT, n = 17, and homozygotes, n = 12; p = 0.0002 between WT and heterozygotes, n = 8), 30 μM nicotine (p = 0.0075; n = 9 for WT and n = 20 for homozygotes), 100 μM nicotine (p = 0.02 between WT, n = 9, and homozygotes, n = 22; p = 0.007 between WT and heterozygotes, n = 21), 300 μM nicotine (p = 0.02 between WT, n = 8, and homozygotes, n = 22; p = 0.01 between WT and heterozygotes

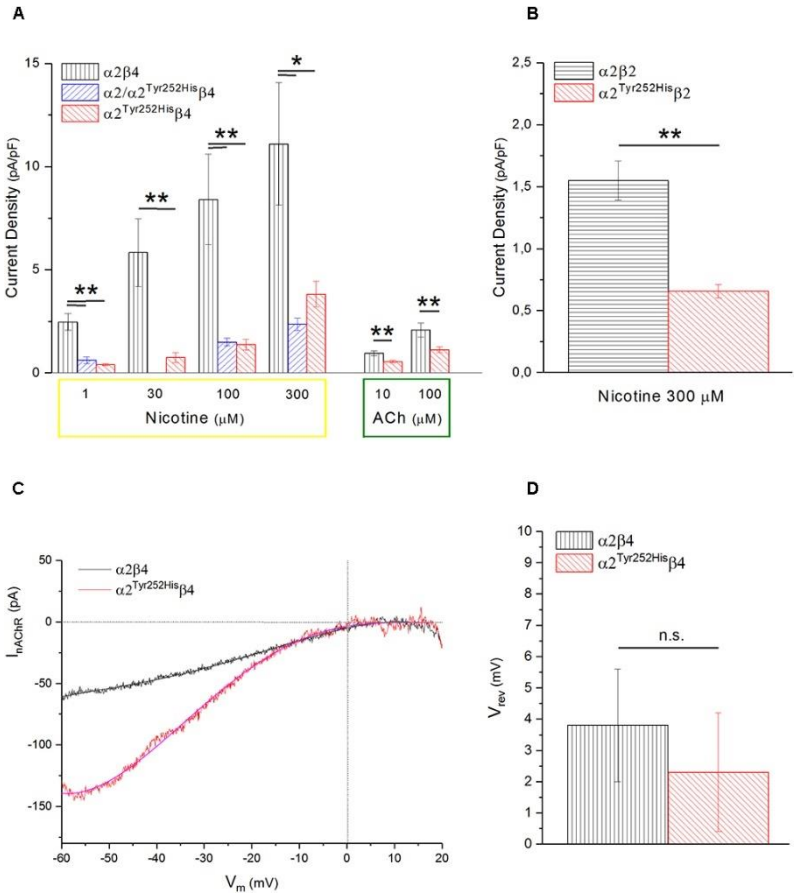

Figure 2.2. *(follows)*, n = 21), 10 μM ACh (p = 0.0023; n = 17 for WT and 15 for homozygotes), 100 μM ACh (p = 0.010; n = 22 for WT and n = 19 for homozygotes), ∗p < 0.05; ∗∗p < 0.01. (B) Same as (A), but for α2β2 and α2^{Tyr252His}β4 receptors. For 1 μM nicotine (p = 0.0004; n = 10 for WT and n = 7 for homozygotes), 10 μM nicotine (p = 0.0008; n = 11 for WT and n = 7 for homozygotes), 300 μM nicotine (p = 0.0006; n = 12 for WT and n = 11 for homozygotes). (B) Same as (A), but for α2β2 and α2^{Tyr252His}β4 receptors, tested with 300 μM nicotine (p = 0.0006; n = 12 for WT and n = 11 for homozygotes), ∗∗p < 0.01. (C) Representative current traces for the indicated receptor type, obtained by stimulating the cell with 1 s voltage ramps (–60 to +20 mV), in the

Figure 2.2. *(follows)* presence or absence of 600 μM nicotine. The background current was subtracted to the one obtained in the presence of nicotine. V_{rev} was estimated by fitting the currents with a polynomial function. (D) Average V_{rev} values measured in WT (n = 11) and mutant (n = 11) receptors. The reported values were not significantly different between WT and mutant (with unpaired t-test).

To compare the current amplitudes obtained in cells with different surface areas, we report in Figure 2.2 A the average peak whole-cell current densities (i.e., for each cell, the peak current was divided by the cell capacitance) obtained in the presence of the indicated concentrations of agonist, for the indicated α2β4 nAChR subtypes. The current density observed in the presence of nicotine was decreased by approximately 80% by $\alpha2^{Tyr252His}$, in both homozygous and heterozygous condition. In agreement with previous reports (Di Resta et al. 2010; Conti et al. 2015), the α2β2 nAChR subtype generally yielded lower functional expression in HEK293 cells, as compared to α2β4. Therefore, the maximal current densities for α2β2 receptors are reported for 300 mM nicotine (Figure 2.2 B). In this case, the presence of $\alpha2^{Tyr252His}$ brought the peak current density from 1.55 ± 0.3 pA/pF (WT; n = 12), to 0.67 ± 0.1 pA/pF (homozygote; n = 11). Similar results were obtained with the physiological agonist ACh. The average current densities measured at 10 and 100 mM ACh for WT and mutant receptors are shown in Figure 2.2 A.

To study whether $\alpha2^{Tyr252His}$ produced major alterations in the nAChR ion selectivity, we measured the reversal potential

(V_{rev}) of α2β4 and α2^{Tyr252His}β4 receptors, as previously described (Conti et al. 2015). In brief, current voltage relations were obtained by applying 1 s voltage ramps between - 60 and + 20 mV, in the presence or absence of nicotine. Three ramps were usually averaged in either condition. Next, to isolate the nicotinic current, the background current obtained in the absence of nicotine was subtracted to the current recorded in the presence of nicotine. The resulting current-voltage relations were fit by polynomial functions, to estimate the nAChR V_{rev}. In general, V_{rev} turned out to be close to 0 mV for both α2β4 and α2^{Tyr252His}β4 receptors, in agreement with the typical V_{rev} observed in mammalian heteromeric nAChRs (Becchetti et al. 2015). Representative current traces and the average V_{rev} values estimated in a series of similar experiments are shown, respectively, in Figure 2.2 C and D. These results suggest that major alterations in the ion selectivity are unlikely to be produced by α2^{Tyr252His}.

Figure 2.3. Concentration-response analysis. (A) Concentration-response relation derived from patch-clamp results for α2β4 receptors. Data points are average peak whole-cell currents, normalized to the current elicited by 300 μM nicotine in WT receptors. Continuous line is fit to equation (1). The relative estimated parameters were: EC_{50high}: 0.08 ± 0.027 μM; EC_{50low}: 24.7 ± 2.76 μM; nH1: 2.41 ± 2.6; nH2: 1.24 ± 0.15. (B) Same as (A), for α2^{Tyr252His}β4. In this case, peak currents are normalized to the current elicited by 800 μM nicotine. Representative currents are shown in the inset. Continuous line is fit to equation (1). The relative estimated parameters were: EC_{50high}: 23.4 ± 23 μM; EC_{50low}: 275.7 ± 12.5 μM; nH_1: 0.87 ± 0.27; nH_2: 3.44 ± 0.81.

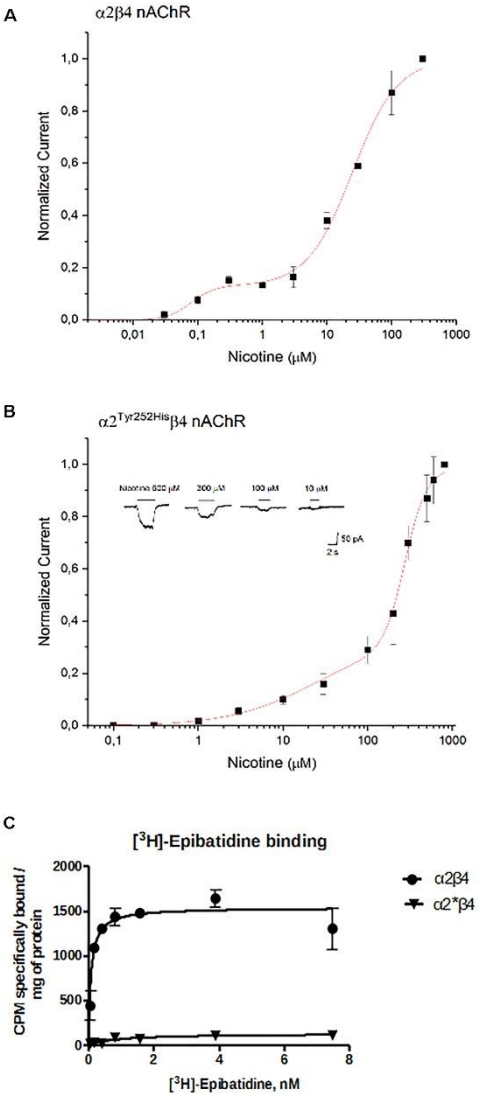

Figure 2.3. *(follows)* (C) Saturation binding experiments aimed to determine K_d and B_{max} of [3H] Epibatidine in cells transfected with α2β4, or $\alpha2^{Tyr252His}\beta4$ (α2∗β4), or non-transfected. Curves were obtained from two independent saturation experiments using a non-linear least squares analysis program using GraphPad Prism 6.

The concentration-response curves for nicotine were obtained by applying different concentrations of agonist at -60 mV. The peak currents thus obtained were normalized to

the current obtained at 300 mM (for α2β4), or 600 mM (for $\alpha2^{Tyr252His}\beta4$), and, respectively, plotted in Figures 2.3. At higher agonist concentrations, the peak currents tended to decrease. This is also observed with other nAChR subtypes and has been attributed to a blocked channel state at high concentrations of agonist (Maconochie and Knight, 1992). The presence of $\alpha2^{Tyr252His}$ strongly decreased the amplitude of the currents activated by nicotine, which were barely detectable at concentrations lower than 10 mM. In fact, $\alpha2^{Tyr252His}$ caused an approximately 10-fold right shift of the apparent EC_{50} of both the high and low affinity components of α2β4 receptors. In particular, EC_{50high} was 23 mM for $\alpha2^{Tyr252His}\beta4$, and 0.8 mM for α2β4 receptors, while EC_{50low} was 275 mM for $\alpha2^{Tyr252His}\beta4$, and 25 mM for α2β4 receptors. The patch-clamp results can be compared with the measurements carried out with [3H] Epibatidine (Figure 2.3 C). The binding affinities (K_d) of [3H] Epibatidine for transfected α2β4 and $\alpha2^{Tyr252His}\beta4$ subtypes, were determined by saturation binding experiments. The affinity (K_d) of [3H] Epibatidine for the α2β4 or $\alpha2^{Tyr252His}\beta4$ nAChR subtypes were, respectively, 0.085 and 0.89 nM, and were derived from the average value of two independent [3H] Epibatidine binding saturation experiments. In addition to the difference in K_d, analysis of the saturation curves also showed that the B_{max} of [3H] Epibatidine binding (expressed as cpm

specifically bound/mg of protein) is much lower for $\alpha 2^{Tyr252His}\beta 4$ receptors than for α2β4. In fact, fitting the saturation curves and calculating the cpm specifically bound by [3H] Epibatidine/mg of protein gave 1535 cpm for α2β4 and 127 for $\alpha^{2Tyr252His}\beta 4$ (Figure 2.3 C). Given that the Western Blot for α2 expression showed no significant differences, we conclude that the strong decrease produced by $\alpha 2^{Tyr252His}$ on both B_{max} and maximal whole-cell currents can be attributed to a conspicuous decrease in the number of channels bound to the agonist.

Discussion

When expressed in HEK293 cells, the receptors containing $\alpha 2^{Tyr252His}$ displayed a marked reduction of whole-cell currents, as compared to WT receptors, in all experimental conditions. Such a decrease was paralleled by a B_{max} decrease with [3H]-epibatidine. Moreover, the concentration-response curves determined by both methods showed that $\alpha 2^{Tyr252His}$ produced an approximate 10-fold decrease in the apparent affinity for the tested agonists of the α2β4 subtype (Figure 2.3). The decrease in maximal current and B_{max} could be caused by a smaller single-channel conductance, a more negative V_{rev}, a decrease of the average number of active channels onto the plasma membrane, or a combination thereof. Because V_{rev} was not altered by $\alpha 2^{Tyr252His}$ and

considering that Tyr252 is placed far from the pore region, we believe a major alteration of the channel's conductive properties is unlikely. Moreover, neither subunits' transcription nor membrane expression were altered by $\alpha2^{Tyr252His}$ (data not shown). Therefore, we attribute the overall reduction in the maximal response to the agonist, accompanied by a right-shift of the activation curve, to a strong decrease of the affinity of the ligand binding site for the agonist. Based on subunit sequence and what is known about the 3D structure of human α4β2 nAChRs (Morales-Perez et al. 2016; Walsh et al. 2018), as well as the extracellular domain of human α2 subunits (Kouvatsos et al. 2016), Tyr252 results to be located in the pre-M1 functional loop C. A simple explanation of our results is that adding a positively charged histidine in the binding site would cause an electrostatic repulsion for the positively charged agonists, which would lead to a lower binding affinity. It is also possible that altering the local structure of the pre-M1 region could considerably increase the energy required to transduce the conformational change from the ligand binding site to the pore region. Fully discriminating between these (not mutually exclusive) possibilities would require extensive single channel data. Regardless of the mechanistic details, our results suggest that, in the case of $\alpha2^{Tyr252His}$, a dominant negative effect is

probably responsible for the main pathophysiological consequences.

Appendix. Implication of CHRNA2 mutations in other epileptic syndromes?

$\alpha2^{Arg121Leu}$ Mutation

We next studied other CHRNA2 mutations linked to epileptic syndromes. I here present the functional characterization of the mutation c.362G>T on Chromosome 8:27324833, which leads to the amino-acid substitution α2Arg121Leu. This mutation was identified by Carlo Nobile and colleagues (CNR, Padua) as linked to Autosomal Dominant Lateral Temporal Lobe Epilepsy.

Lateral temporal epilepsies are a poorly studied group of conditions, covering lesional and non-lesional cases. Among the latter, ADLTE is a well-defined, albeit rare, condition characterized by onset in adolescence or early adulthood of lateral temporal seizures with prominent auditory auras sometimes triggered by external noises, normal conventional magnetic resonance imaging (MRI), good response to antiepileptic treatment, and overall benign outcome. ADLTE is thought to be underlied by considerable genetic heterogeneity, despite the relatively homogeneous clinical

picture (Michelucci et al. 2009; Manna et al. 2013). Mutations in the leucine-rich, glioma-inactivated 1 (LGI1) gene are found in about 50% of ADLTE families and 2% of sporadic cases. Different LGI1 mutations are associated with a rather homogeneous phenotype, with no obvious genotype-phenotype correlation. Both truncating and missense mutations appear to prevent secretion of mutant proteins, suggesting a loss of function effect of mutations. LGI1 shows no homology with known ion channel genes. Recent findings suggest that LGI1 may exert multiple functions, but their relation to lateral temporal epilepsy is unknown (Nobile et al. 2009). Moreover, causal mutations in the Reelin gene have been identified in seven ADLTE-affected families without LGI1 mutations. Reelin is a secreted protein which has important functions in both the developing and adult brain and is also found in the blood serum. ADLTE-related mutations significantly decrease serum levels of Reelin, suggesting an inhibitory effect of mutations on protein secretion. Moreover, Reelin and LGI1 co-localize in a subset of rat brain neurons, supporting an involvement of both proteins in a common molecular pathway underlying ADLTE (Dazzo et al. 2015). Finally, two ADLTE-causing variants in the molecule interacting with CasL (MICAL-1) 1 gene have been identified: a p.Gly150Ser substitution occurring in the enzymatically active monooxygenase (MO) domain and a p.Ala1065fs

frameshift indel in the C-terminal domain, which inhibits the oxidoreductase activity of the MO domain. Each variant segregated with ADLTE in a single family. In cell-based assays, both variants significantly increased MICAL-1 oxidoreductase activity and induced cell contraction in COS7 cells, which likely resulted from disassembly of actin filaments. This points to dysregulation of the actin cytoskeleton dynamics in developing and adult neurons as a likely mechanism by which MICAL-1 pathogenic variants lead to ADLTE (Dazzo et al. 2018).

The aminoacidic substitution $\alpha2^{Arg121Leu}$ is located in the extracellular domain, in the region devoted to agonist binding, so it may affect the opening dynamics or kinetics of the channel. In homozygous condition, $\alpha2^{Arg121Leu}$ decreased the peak current density evoked by saturating nicotine by ~40% (α2β2; from 1.11 ± 0.11 to 0.49 ± 0.08 pA/pF as shown in Fig. 2.4 B) or ~25% (α2β4; from 6.95 ± 2.77 to 1.44 ± 0.44 pA/pF, Fig. 2.4 A and D), without altering the current reversal potential, ruling out overt effects on the channel permeability to ions (Fig. 2.4 C). As the current reduction in the mutant was not observed when using ACh as agonist (Fig. 2.4 A), our data are compatible with, but does not allow to conclude that loss-of-function mutations in CHRNA2 could be associated with ADLTE.

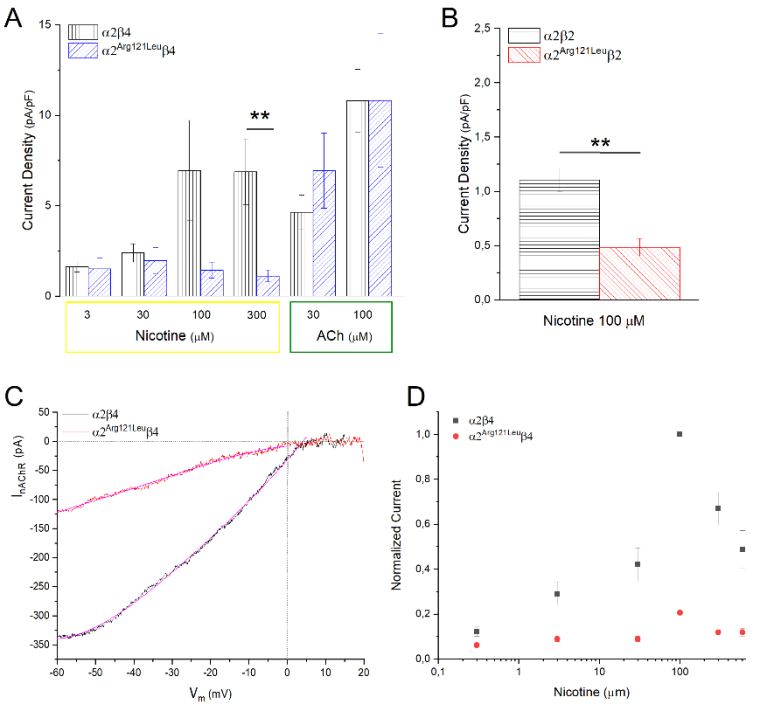

Figure 2.4. α2^{Arg121Leu} decreases the maximal current density evoked by nicotine, but not by ACh, without altering V_{rev}. (A) Bars represent average peak whole-cell current densities measured at the indicated concentrations of nicotine or ACh, in cells expressing α2β4 or α2^{Arg121Leu}β4. The results of representative measurements are shown for 3, 30, 100 and 300 μM nicotine ($p = 0{,}006$, $n = 17$ for WT, $n = 25$ for homozygotes), $*p < 0.05$; $**p < 0.01$. (B) Same as (A), but for α2β2 and α2^{Arg121Leu}β4 receptors. For 100 μM nicotine ($p = 0.0001$, $n = 10$ for WT, $n = 13$ for homozygotes). (C) Representative current traces for the indicated receptor type, obtained by stimulating the cell with 1 s voltage ramps (–60 to +20 mV), in the presence or absence of 300 μM nicotine. (D) Concentration-response relation derived from patch-clamp results for α2β4 receptors. Data points are average peak whole-cell currents, normalized to the current elicited by 300 μM nicotine in WT receptors.

Discussion

The $\alpha2^{Arg121Leu}$ subunit seems to have a similar phenotype compared to the $\alpha2^{Tyr252His}$ but with a smaller current density reduction with saturating nicotine. However, the fact that ACh effects were not comparable to those of nicotine on the same receptors laid doubt on the possible causative role of the mutation for ADLTE and we decided to discontinue the study. We cannot anyway exclude an allosteric alterative effect of this mutation in linkage with the pathology.

Taken together, the functional features conferred to the nAChR by the $\alpha2^{Tyr252His}$ or $\alpha2^{Arg121Leu}$ subunit resemble those previously observed with p.Ile297Phe (Conti et al. 2015), and differ from those of p.Ile279Asn (Aridon et al. 2006). These results support the notion that loss of receptor function may be a more common epileptogenic mechanism for mutant α2 nAChRs, as compared to other nicotinic subunits. We hypothesize that the reasons for this difference may depend on the different distribution of nAChR subunits in the brain. The specific role of each subunit is still uncertain (Zoli et al. 2015), and particularly so in the case of α2 (Baddick and Marks, 2011), despite its relatively widespread expression in the mammalian brain (Wada et al. 1989; Marks et al. 1992). Recent work in the mouse neocortex suggested that α2 nAChR subunits are specifically expressed in the Martinotti

cells, usually somatostatin^{+}, that project to layer I and can synchronize the thick-tufted pyramidal cells in layer V in the θ frequency range (Hilscher et al. 2017). The present uncertainties about the distribution of α2 subunits at the cellular level in the human brain prevent to bring the comparison too far. Nonetheless, we can hypothesize that a decreased cholinergic response in Martinotti cells could reduce their responsiveness and increase their inhibition, which could lead to pyramidal cell synchronous excitation through Martinotti rebound excitation after the inhibitory phase (Becchetti et al. 2015; Hilscher et al. 2017). This kind of widely spread time-locked activity is often causative of epileptic events and it could be a plausible pathogenetic mechanism for the epileptic diseases to which these mutations are linked to.

References

Alkondon, M., Pereira, E. F., Eisenberg, H. M., & Albuquerque, E. X. (2000). Nicotinic receptor activation in human cerebral cortical interneurons: a mechanism for inhibition and disinhibition of neuronal networks. Journal of Neuroscience, 20, 66-75.

Aracri, P., Consonni, S., Morini, R., Perrella, M., Rodighiero, S., Amadeo, A., & Becchetti, A. (2010). Tonic modulation of GABA release by nicotinic acetylcholine receptors in layer V of the murine prefrontal cortex. Cerebral Cortex, 20, 1539-1555.

Aracri, P., Amadeo, A., Pasini, M. E., Fascio, U., & Becchetti, A. (2013). Regulation of glutamate release by heteromeric nicotinic receptors in layer V of the secondary motor region (Fr2) in the

dorsomedial shoulder of prefrontal cortex in mouse. Synapse, 67, 338-357.

Aracri, P., Meneghini, S., Coatti, A., Amadeo, A., & Becchetti, A. (2017). α4β2∗ nicotinic receptors stimulate GABA release onto fast-spiking cells in layer V of mouse prefrontal (Fr2) cortex. Neuroscience, 340, 48-61.

Aridon, P., Marini, C., Di Resta, C., Brilli, E., De Fusco, M., Politi, F., ... & Casari, G. (2006). Increased sensitivity of the neuronal nicotinic receptor α2 subunit causes familial epilepsy with nocturnal wandering and ictal fear. The American Journal of Human Genetics, 79, 342-350.

Baddick, C. G., & Marks, M. J. (2011). An autoradiographic survey of mouse brain nicotinic acetylcholine receptors defined by null mutants. Biochemical pharmacology, 82, 828-841.

Becchetti, A., Aracri, P., Meneghini, S., Brusco, S., & Amadeo, A. (2015). The role of nicotinic acetylcholine receptors in autosomal dominant nocturnal frontal lobe epilepsy. Frontiers in physiology, 6, 22.

Brusco, S., Ambrosi, P., Meneghini, S., & Becchetti, A. (2015). Agonist and antagonist effects of tobacco-related nitrosamines on human α4β2 nicotinic acetylcholine receptors. Frontiers in pharmacology, 6, 201.

Combi, R., Dalprà, L., Ferini-Strambi, L., & Tenchini, M. L. (2005). Frontal lobe epilepsy and mutations of the corticotropin-releasing hormone gene. Annals of Neurology: Official Journal of the American Neurological Association and the Child Neurology Society, 58, 899-904.

Combi, R., Ferini-Strambi, L., Montruccoli, A., Bianchi, V., Malcovati, M., Zucconi, M., ... & Tenchini, M. L. (2005). Two new putative susceptibility loci for ADNFLE. Brain research bulletin, 67, 257-263.

Combi, R., Ferini-Strambi, L., & Tenchini, M. L. (2009). CHRNA2 mutations are rare in the NFLE population: evaluation of a large cohort of Italian patients. Sleep medicine, 10, 139-142.

Conti, V., Aracri, P., Chiti, L., Brusco, S., Mari, F., Marini, C., ... & Guerrini, R. (2015). Nocturnal frontal lobe epilepsy with paroxysmal arousals due to CHRNA2 loss of function. Neurology, 84, 1520-1528.

Cooper, S. T., Harkness, P. C., Baker, E. R., & Millar, N. S. (1999). Up-regulation of cell-surface α4β2 neuronal nicotinic receptors by lower temperature and expression of chimeric subunits. Journal of Biological Chemistry, 274, 27145-27152.

Couey, J. J., Meredith, R. M., Spijker, S., Poorthuis, R. B., Smit, A. B., Brussaard, A. B., & Mansvelder, H. D. (2007). Distributed network actions by nicotine increase the threshold for spike-timing-dependent plasticity in prefrontal cortex. Neuron, 54, 73-87.

Covernton, P. J., & Connolly, J. G. (2000). Multiple components in the agonist concentration–response relationships of neuronal nicotinic acetylcholine receptors. Journal of neuroscience methods, 96, 63-70.

Dani, J. A., & Bertrand, D. (2007). Nicotinic acetylcholine receptors and nicotinic cholinergic mechanisms of the central nervous system. Annu. Rev. Pharmacol. Toxicol., 47, 699-729.

Dazzo, E., Fanciulli, M., Serioli, E., Minervini, G., Pulitano, P., Binelli, S., ... & Nobile, C. (2015). Heterozygous reelin mutations cause autosomal-dominant lateral temporal epilepsy. The American Journal of Human Genetics, 96, 992-1000.

Dazzo, E., Rehberg, K., Michelucci, R., Passarelli, D., Boniver, C., Vianello Dri, V., ... & Nobile, C. (2018). Mutations in MICAL-1cause autosomal-dominant lateral temporal epilepsy. Annals of neurology, 83, 483-493.

De Fusco, M., Becchetti, A., Patrignani, A., Annesi, G., Gambardella, A., Quattrone, A., ... & Casari, G. (2000). The nicotinic receptor β2 subunit is mutant in nocturnal frontal lobe epilepsy. Nature genetics, 26, 275-276.

Di Resta, C., Ambrosi, P., Curia, G., & Becchetti, A. (2010). Effect of carbamazepine and oxcarbazepine on wild-type and mutant neuronal nicotinic acetylcholine receptors linked to nocturnal frontal lobe epilepsy. European journal of pharmacology, 643, 13-20.

Ferini-Strambi, L., Sansoni, V., & Combi, R. (2012). Nocturnal frontal lobe epilepsy and the acetylcholine receptor. The neurologist, 18, 343-349.

Han, Z. Y., Le Novère, N., Zoli, M., Hill Jr, J. A., Champtiaux, N., & Changeux, J. P. (2000). Localization of nAChR subunit mRNAs in the brain of Macaca mulatta. European Journal of Neuroscience, 12, 3664-3674.

Heron, S. E., Smith, K. R., Bahlo, M., Nobili, L., Kahana, E., Licchetta, L., ... & Dibbens, L. M. (2012). Missense mutations in the sodium-gated potassium channel gene KCNT1 cause severe autosomal dominant nocturnal frontal lobe epilepsy. Nature genetics, 44, 1188-1190.

Hilscher, M. M., Leão, R. N., Edwards, S. J., Leão, K. E., & Kullander, K. (2017). Chrna2-Martinotti cells synchronize layer 5 type A pyramidal cells via rebound excitation. PLoS biology, 15, e2001392.

Ishida, S., Picard, F., Rudolf, G., Noé, E., Achaz, G., Thomas, P., ... & Baulac, S. (2013). Mutations of DEPDC5 cause autosomal dominant focal epilepsies. Nature genetics, 45, 552-555.

Khan, S., & Al Baradie, R. (2012). Epileptic encephalopathies: an overview. Epilepsy Research and Treatment, 2012.

Kouvatsos, N., Giastas, P., Chroni-Tzartou, D., Poulopoulou, C., & Tzartos, S. J. (2016). Crystal structure of a human neuronal nAChR extracellular domain in pentameric assembly: Ligand-bound α2 homopentamer. Proceedings of the National Academy of Sciences, 113, 9635-9640.

Lambe, E. K., Picciotto, M. R., & Aghajanian, G. K. (2003). Nicotine induces glutamate release from thalamocortical terminals in prefrontal cortex. Neuropsychopharmacology, 28, 216-225.

Maconochie, D. J., & Knight, D. E. (1992). Markov modelling of ensemble current relaxations: bovine adrenal nicotinic receptor currents analysed. The Journal of physiology, 454, 155-182.

Manna, I., Mumoli, L., Labate, A., Citrigno, L., Ferlazzo, E., Aguglia, U., ... & Gambardella, A. (2014). Autosomal dominant lateral

temporal epilepsy (ADLTE): absence of chromosomal rearrangements in LGI1 gene. Epilepsy research, 108, 597-599.

Marks, M. J., Pauly, J. R., Gross, S. D., Deneris, E. S., Hermans-Borgmeyer, I., Heinemann, S. F., & Collins, A. C. (1992). Nicotine binding and nicotinic receptor subunit RNA after chronic nicotine treatment. Journal of Neuroscience, 12, 2765-2784.

Michelucci, R., Pasini, E., & Nobile, C. (2009). Lateral temporal lobe epilepsies: clinical and genetic features. Epilepsia, 50, 52-54.

Morales-Perez, C. L., Noviello, C. M., & Hibbs, R. E. (2016). X-ray structure of the human α4β2 nicotinic receptor. Nature, 538, 411-415.

Nobile, C., Michelucci, R., Andreazza, S., Pasini, E., Tosatto, S. C., & Striano, P. (2009). LGI1 mutations in autosomal dominant and sporadic lateral temporal epilepsy. Human mutation, 30, 530-536.

Nobili, L., Proserpio, P., Combi, R., Provini, F., Plazzi, G., Bisulli, F., ... & Tinuper, P. (2014). Nocturnal frontal lobe epilepsy. Current neurology and neuroscience reports, 14, 424.

Phillips, H. A., Favre, I., Kirkpatrick, M., Zuberi, S. M., Goudie, D., Heron, S. E., ... & Mulley, J. C. (2001). CHRNB2 is the second acetylcholine receptor subunit associated with autosomal dominant nocturnal frontal lobe epilepsy. The American Journal of Human Genetics, 68, 225-231.

Porter, J. T., Cauli, B., Tsuzuki, K., Lambolez, B., Rossier, J., & Audinat, E. (1999). Selective excitation of subtypes of neocortical interneurons by nicotinic receptors. Journal of Neuroscience, 19, 5228-5235.

Quik, M., Polonskaya, Y., Gillespie, A., Jakowec, M., Lloyd, G. K., & Langston, J. W. (2000). Localization of nicotinic receptor subunit mRNAs in monkey brain by in situ hybridization. Journal of Comparative Neurology, 425, 58-69.

Quik, M., Vailati, S., Bordia, T., Kulak, J. M., Fan, H., McIntosh, J. M., ... & Gotti, C. (2005). Subunit composition of nicotinic receptors in monkey striatum: effect of treatments with 1-methyl-4-phenyl-1, 2, 3, 6-tetrahydropyridine or L-DOPA. Molecular pharmacology, 67, 32-41.

Sansoni, V., Forcella, M., Mozzi, A., Fusi, P., Ambrosini, R., Ferini-Strambi, L., & Combi, R. (2013). Functional characterization of a CRH missense mutation identified in an ADNFLE family. PloS one, 8, e61306.

Steinlein, O. K., Mulley, J. C., Propping, P., Wallace, R. H., Phillips, H. A., Sutherland, G. R., ... & Berkovic, S. F. (1995). A missense mutation in the neuronal nicotinic acetylcholine receptor α4 subunit is associated with autosomal dominant nocturnal frontal lobe epilepsy. Nature genetics, 11, 201-203.

Tinuper, P., Bisulli, F., Cross, J. H., Hesdorffer, D., Kahane, P., Nobili, L., ... & Ottman, R. (2016). Definition and diagnostic criteria of sleep-related hypermotor epilepsy. Neurology, 86, 1834-1842.

Vidal, C., & Changeux, J. P. (1993). Nicotinic and muscarinic modulations of excitatory synaptic transmission in the rat prefrontal cortexin vitro. Neuroscience, 56, 23-32.

Wada, E., Wada, K., Boulter, J., Deneris, E., Heinemann, S., Patrick, J., et al. (1989). Distribution of alpha 2, alpha 3, alpha 4, and beta 2 neuronal nicotinic receptor subunit mRNAs in the central nervous system: a hybridization histochemical study in the rat. J Comp Neurol 284, 314–335.

Walsh, R. M., Roh, S. H., Gharpure, A., Morales-Perez, C. L., Teng, J., & Hibbs, R. E. (2018). Structural principles of distinct assemblies of the human α4β2 nicotinic receptor. Nature, 557, 261-265.

Zoli, M., Léna, C., Picciotto, M. R., & Changeux, J. P. (1998). Identification of four classes of brain nicotinic receptors using β2 mutant mice. Journal of Neuroscience, 18, 4461-4472.

Zoli, M., Pistillo, F., & Gotti, C. (2015). Diversity of native nicotinic receptor subtypes in mammalian brain. Neuropharmacology, 96, 302-311.

Chapter 3. Morpho-functional alterations in the prefrontal cortex layer V of mice conditionally expressing the ADSHE-linked β2^{V287L} nAChR subunit. Possible role of α2 subunits.

The work presented in this chapter is an extract of the following manuscript:

Meneghini, S., Modena, D., Colombo, G., Coatti, A., Milani, N., Madaschi, L., Amadeo, A., & Becchetti, A.

The β2^{V287L} nicotinic subunit linked to sleep-related epilepsy differently affects fast spiking and regular spiking somatostatin-expressing neurons in murine prefrontal cortex.

Submitted paper (2022).

Abstract

Mutant subunits of the neuronal nicotinic ACh receptor (nAChR) can cause Autosomal Dominant Sleep-related Hypermotor Epilepsy (ADSHE), characterized by frontal seizures during non-rapid eye movement (NREM) sleep. We studied the pathogenetic mechanism in mice conditionally expressing the ADSHE-linked β2^{V287L} nAChR subunit. These showed minor morphological alterations in pyramidal neurons' (Py) dendritic ramification, as well as a ~10%

decrease of prefrontal cortex thickness. The expression of $\beta2^{V287L}$ substantially decreased the glutamatergic input on FS neurons. The abnormal network hyperexcitability may thus depend on the permanent impairment of surround inhibition in prefrontal cortex. Moreover, $\beta2^{V287L}$ expression was correlated to larger somatic nicotinic currents in regular spiking interneurons expressing somatostatin (largely Martinotti cells). These results may explain why NREM sleep favours ADSHE seizures and why nicotine administration can be palliative in patients.

Introduction

In the mammalian brain, the most widespread heteromeric nAChR subtype is α4β2*, which is consistent with the observation that mutant CHRNA4 and CHRNB2, respectively coding for the α4 and β2 nAChR subunits, are linked to ADSHE (Steinlein et al. 1995; De Fusco et al. 2000). A widely studied ADSHE mutation is β2V287L, which in functional expression systems causes a ‘gain of function’ phenotype by slowing α4β2 nAChR desensitization (De Fusco et al. 2000) and increasing its sensitivity to the agonists (Son et al. 2009; Nichols et al. 2016; Indurthi et al. 2019). This is a common feature of ADSHE mutations falling on either CHRNA4 or CHRNB2 (Becchetti et al. 2015). Yet, the pathophysiological interpretation remains uncertain. As summarized earlier,

nAChRs regulate both excitatory and inhibitory transmission at the pre- and post--synaptic level, with a complex pattern that depends on brain region and cortical layer (Picciotto et al. 2012; Becchetti et al. 2015). Moreover, β2* nAChRs regulate synaptic maturation (Rossi et al. 2001; McLaughlin et al. 2003; Bailey et al. 2012; Lozada et al. 2012; Molas and Dierssen, 2014). Therefore, the functional alterations underlying ADSHE may also comprise a permanent synaptic unbalance arisen during late developmental stages. Finally, the implication of 'loss-of-function' CHRNA2 mutations remain a mistery (see Chapter 2).

To better understand ADSHE pathogenesis, several mutant subunits have been expressed in rodent strains (Klaassen et al. 2006; Teper et al. 2007; Zhu et al. 2008; Manfredi et al. 2009; Xu et al. 2011; O'Neill et al. 2013; Shiba et al. 2015; Fukuyama et al. 2020). Especially close to the human pathology is the phenotype displayed by a transgenic murine strain conditionally expressing $\beta2^{V287L}$ in a TET-off system (Manfredi et al. 2009). Mice expressing the transgene display brief spontaneous seizures (~25) during periods of increased EEG delta wave activity, which is typical of slow-wave sleep. Such phenotype is not observed if the transgene is silenced during brain development, until the end of the second postnatal week, even if expression is subsequently reactivated. This suggests that irreversible synaptic

alterations are caused by early action of the transgene (Manfredi et al. 2009).

We recently used Manfredi's strain to map the synaptic alterations produced by β2V287L in the mature prefrontal cortex (PFC). We analyzed pyramidal cells and the GABAergic interneuron populations more directly involved in controlling the spread of epileptiform activity in vitro, namely fast-spiking (FS) and regular spiking somatostatin (SOM)-expressing neurons (Trevelyan et al. 2006; Cammarota et al. 2013; Parrish et al. 2019). Electrophysiological experiments were focused on layer V of the dorsomedial shoulder region of murine PFC, also known as frontal area 2 (Fr2) which could be directly implicated in the generation of hypermotor seizures, as discussed earlier (Introduction of Part 2). In brief, we found that early expression of β2V287L leads to a stable decrease of the glutamatergic input on FS neurons, which would explain the permanent hyperexcitability. Moreover, nAChR stimulation partly rescues the effect, which would explain the somewhat paradoxical observation that 'gain of function' nAChR mutations facilitate seizures during NREM sleep, i.e. when the cholinergic tone is lowest (Jones, 2020).

Here, we focus on our results on the other main population of layer V GABAergic neurons (SOM+), which turn out to

express α2* nAChRs, at least in mice (Hilscher et al. 2017) and may thus help explain the role of this subunit in ADSHE.

Materials and Methods

Animals

Mice were kept in pathogen-free conditions, with a 12 h light-dark cycle, and water and food ad libitum. Animal handling and experimentation comply with the Italian law (2014/26, which implemented the 2010/63/UE) and were approved by the Animal Welfare Ethical Committee of Milano-Bicocca University and by the Italian Ministry of Health (101/2016-PR). We used the S3 line of double transgenic FVB-TG (tTA:Chrnb2V287L) strain, which expresses the $\beta2^{V287L}$ nAChR subunit in the brain, under the tetracycline-controlled transcriptional activator (tTA with the pan-neural promoter of prionic protein; TET-off system). When necessary, the transgene was silenced by adding doxycycline to drinking water (1 mg/ml, with sucrose to mask the bitter taste). In fact, when doxycycline binds tTA, it is no longer able to activate the transgene expression and only the endogenous nAChR subunits are expressed in the mouse brain. Genotyping was carried out following Manfredi et al. (2009). The double transgenic mice (hereafter $\beta2^{V287L}$) were compared with their littermates not expressing the transgene (Control), i.e. mice expressing the transactivator (tTA) or wild-type (WT), as

indicated. We used mice of either sex between the 1st and the 4th postnatal month. No evidence was found of a sex-dependent effect on synaptic transmission.

Tissue preparation and brain regions

For patch-clamp experiments, mice were anesthetized with isoflurane 5%. Brains were extracted by standard procedures and kept in ice-refrigerated solution containing (mM): 87 NaCl, 21 $NaHCO_3$, 1.25 NaH_2PO_4, 7 $MgCl_2$, 0.5 $CaCl_2$, 2.5 KCl, 25 D-glucose, 75 sucrose, and equilibrated with 95% O_2 and 5% CO_2 (pH 7.4), supplemented with ascorbic acid (79.2 mg/l). Coronal Fr2 slices (300 µm thick) were cut between +2.68 and +2.10 mm from bregma, as previously reported (Aracri et al. 2010), and incubated in the above solution (1 h at room temperature, RT), before being transferred to the recording chamber.

For immunohistochemistry, extracted brains were immersed in 4% paraformaldehyde in phosphate buffer (PB) for 24 h, at 4°C. By PFC, we refer to the entire secondary motor region (also known as M2 or Fr2) in the dorsomedial shoulder of prefrontal cortex. According to Franklin and Paxinos (2001), coronal PFC sections (50 µm thick) were cut with a VT1000S vibratome (Leica Microsystems) between +2.58 and -0.06 mm from bregma. For somatosensory cortex (SS), we sampled the extended SS region between +1.54 and -1.64

mm from bregma. Stereological cell counts of cholinergic neurons were carried out on coronal brain sections between -5.02 and -4.36 mm from bregma, for pedunculopontine (PPT) and laterodorsal tegmental (LDT) nuclei, and between -0.34 and -0.82 mm from bregma for nucleus basalis magnocellularis (NBM). Anatomical coordinates are summarized in Table 1.

Dendritic arborization and spine density

Mice were deeply anesthetized by intraperitoneal 4% chloral hydrate (2 ml/100 g), after isoflurane pre-anaesthesia, and sacrificed by intracardiac perfusion with NaCl 0.9%, following Aracri et al. (2013). We used the Golgi-Cox method to stain 300 µm thick slices from PFC (2.58 -1.14 mm from bregma) of 4 WT (2 ♀ and 2 ♂) and 4 $\beta2^{V287L}$ (3 ♀ and 1 ♂; all aged > P60). Sections were imaged by acquiring z-stacks with an Eclipse Ti2 confocal microscope (Nikon) at 40× magnification and 2048-pixel resolution. Analysis was carried out with Fiji ImageJ (Simple Neurite Tracer and Cell Count plugins). From 4 to 17 pyramidal neurons per cortical layer were considered in each mouse. Dendritic arbor complexity was quantified by Sholl analysis (Sholl, 1953) on z-stacks of pyramidal neurons having the most part of basal dendrites spared by the slice cut. The number of intersections were counted between dendrites and 10 µm-spaced concentric spherical surfaces centred on the soma. The ramification index was calculated

by dividing the maximal N of dendrites by the number of primary dendrites. Dendritic spines were counted every 10 µm on at least three dendrites per cell. The mean values for each cell were plotted against dendrite length to assess the spine distribution.

Chemicals and drugs

Chemicals were purchased from Sigma-Aldrich. Stock solutions were prepared in distilled water and stored at -20°C, and were diluted daily in artificial cerebrospinal fluid (ACSF) for use.

Whole-cell patch-clamp recordings in acute brain slices

Cells were examined with an Eclipse E600FN microscope with water immersion DIC objective (Nikon), equipped with IR digital CCD C8484-05G01 camera and HCImage Live acquisition software (Hamamatsu Photonics). Neurons were voltage- or current-clamped with a Multiclamp 700A amplifier (Molecular Devices), at 33-34°C. Borosilicate capillaries (Corning) were pulled with a P-97 Flaming/Brown Micropipette Puller (Sutter Instruments) to a final resistance of 2-3 MΩ. The cell capacitance and series resistance (up to ~75%) were always compensated. Experimental traces were low-pass filtered at 2 kHz and digitized at 10 kHz, with pClamp9/Digidata 1322A (Molecular Devices). For display, they were further low-pass filtered at ~300 Hz. Slices were

perfused at ~2 ml/min with ACSF (mM): 129 NaCl, 21 $NaHCO_3$, 1.6 $CaCl_2$, 3 KCl, 1.25 NaH_2PO_4, 1.8 $MgSO_4$, 10 D-glucose, aerated with 95% O_2 and 5% CO_2 (pH 7.4). For EPSC recording and action potential (AP) profiling, pipette contained (mM): 135 K-gluconate, 5 KCl, 1 $MgCl_2$, 2 MgATP, 0.3 Na_2GTP, 0.5 BAPTA, 10 HEPES (pH 7.25-7.3, adjusted with KOH). No correction for liquid junction potentials was applied to the V_m values reported in the text. Input resistance was measured by applying small stimuli around V_{rest} and was constantly monitored during the experiment. It was usually around 100 MΩ for pyramidal and regular spiking non pyramidal neurons in the second postnatal month. Drugs were applied in the bath and their effect usually reached the steady state within 2 min. EPSCs were registered for 2 to 5 min after obtaining the whole-cell configuration. Only one cell was treated per slice, to avoid long-term receptor inactivation. To locally administer 5-HT, we used a manual picospritzer by Narishige.

Analysis of APs

Analysis was carried out with Clampfit 9.2 (Molecular Devices), OriginPro 2018 (OriginLab Corporation), and Mini Analysis (Synaptosoft Inc.). Spike amplitude was calculated as the difference between AP threshold and peak. Spike width was calculated at half-amplitude. Adaptation was measured at a mean firing frequency of ~100 Hz. After-

hyperpolarization (AHP) was computed as the difference between spike threshold and the most negative V_m reached after repolarization.

Post-recording morphological characterization

Neurobiotin (1 mg/ml) was added to the pipette solution in a fraction of patch-clamp experiments. Slices were fixed post-recording in PB with 4% paraformaldehyde (24-48 h, at 4 °C). Next, they were washed with PBS and incubated with 0.05 M NH_4Cl for 30 min, to block the residual aldehyde groups from fixation. After treatment with 2% bovine serum albumin (BSA) and 0.05% Triton X-100 in PBS (2 h, RT), sections were incubated with Alexa-488-labeled streptavidin (1:200; Molecular Probes, Eugene, OR) in the same solution (3 h, RT). After washing with PBS, slices were transiently mounted on slides with PBS/glycerol. After verifying the success of cell labeling, they were incubated at 4°C overnight with anti-PV (1:2000) and anti-SOM (1:100-200), in PBS with 2% BSA and 0.05% Triton X-100. After rinsing, slices were incubated with the secondary antibodies (3 h, RT): CFTM568-conjugated donkey anti-mouse (Sigma) and Cy5-conjugated donkey anti-rabbit (Jackson ImmunoResearch), both at 1:200 in PBS with 2% BSA. Finally, sections were washed with PBS and mounted on gelatin-coated slides with Vectashield supplemented with DAPI (VectorLabs, Burlingame, CA) for analysis with a Nikon Ti-E/A1+ high performance inverted

confocal laser scanning microscope (Nikon, Tokyo, Japan). 3D neuron reconstruction was performed using the Simple Neurite Tracer plugin in Fiji ImageJ on the green channel Z-stack, holding the signal for Alexa-488-labeled streptavidin.

Statistical analysis

Unless otherwise indicated, data are given as mean values ± SEM. Comparisons between two populations of data were conducted with paired or unpaired Student's t-test, as indicated, after verifying normality (Shapiro-Wilk test and Q-Q Plots) and variance homogeneity (F test). In case of unequal variances, the Welch's correction was applied. Multiple comparisons were analysed with one-way ANOVA followed by Bonferroni's post-hoc test, after verifying variance homogeneity (Levene test). For synaptic events recorded in individual cells, the non-normal distributions of events' amplitudes and inter-event intervals under different treatments were compared with the Kolmogorov-Smirnov (KS) test for two samples. The level of statistical significance is indicated as follows: NS: not significant; $0.01 < p^* < 0.05$; $0.001 < p^{**} \leq 0.01$; $p^{***} \leq 0.001$.

Results

$\beta2^{V287L}$ effects on Fr2 layer V interneurons

From an electrophysiological standpoint, three populations of neurons largely prevail in Fr2 layer V: regular spiking

pyramidal neurons, FS interneurons and regular spiking non-pyramidal (RSNP) cells. Pyramidal neurons display classic firing properties, with no difference between Control and $\beta2^{V287L}$ (Amadeo et al. 2018). FS neurons are PV^{+} cells (Aracri et al. 2017) and presented no major electrophysiological difference between genotypes (Table 3.1). RSNP neurons have V_{rest} around -70 mV; AP frequency of ~50 Hz (200 pA stimulus), with more pronounced adaptation compared to FS cells; spike width of ~1.8 ms (at half-maximal amplitude) and shallow after-hyperpolarization (Table 3.1).

Table 3.1. Expression of $\beta2^{V287L}$ did not alter V_{rest} and firing of FS and RSNP cells. The indicated electrophysiological parameters were measured in a representative sample of Fr2 slices from Control and $\beta2^{V287L}$ mice, in their second postnatal month of life. The ratio between the 4th and the 1st spike interval was calculated under a 200 pA stimulation. No statistical difference was observed between Control and $\beta2^{V287L}$, in any of the measured parameters (unpaired t-test). AHP: after-hyperpolarization.

Type		**Vrest** (mV)	**Spike width** (ms)	**4th spike interval/ 1st spike interval**	**AHP** (mV)	**N**
FS	Ctrl	-70.1 ± 0.33	0.84 ± 0.05	1.18 ± 0.04	-13.8 ± 0.96	15
	$\beta2^{V287L}$	-70.8 ± 1.03	0.89 ± 0.05	1.18 ± 0.03	-12.9 ± 1.03	12

RSNP	Ctrl	-71.3 ± 0.48	1.78 ± 0.09	2.58 ± 0.28	-7.3 ± 0.6	14
	$\beta2^{V287L}$	-72.1 ± 0.57	1.84 ± 0.08	2.51 ± 0.31	-6.3 ± 0.56	14

In analogy with other neocortex regions (Tremblay et al. 2016), a similar number of PV^+ and SOM^+ cells were observed in Fr2 layer V (Fig. 3.1 A), which led us to hypothesize the common RSNP cells belonged to the SOM^+ population. In fact, post-recording morphological characterization revealed a bitufted or multipolar shape accompanied by SOM immunoreactivity (Fig. 3.1 B). Typical RSNP cell firing and the average stimulus-frequency relationship for a population of age-matched Control and $\beta2^{V287L}$ cell are shown in Fig. 3.1 D and E, revealing no major

Figure 3.1. Characterization of RSNP SOM^+ neurons in Fr2 layer V. (A) Representative 3D image reconstructed from a section with triple immunolabeling of VAChT (green), SOM (red) and PV (light blue) in PFC layer V of a Control mouse. The confocal microscope z-stack was 10.5 µm thick (63×, zoom 2). Notice the numerosity of PV^+ and SOM^+ cells was comparable in layer V. Calibration bar: 10 µm. (B) Post-recording 3D reconstruction of an RSNP cell loaded with neurobiotin and identified by Alexa-488-streptavidin labelling (10.8 µm z-stack, 40×). Calibration bar: 10 µm. (C) Post-recording reconstruction of a SOM^+ RSNP neuron, merged channels (max projection of a 10.4 µm max projection of a 10.4 µm zstack, 60×). C', DAPI labeling to identify the nucleus (the neuron shape is outlined). C'', biocytin labeling (green). C''', SOM labeling (red). Calibration bar: 10 µm. (D) Firing pattern of the cell illustrated in B. Stimulus was 200 pA for 500 ms. (E) Average stimulus-frequency relation from a representative group of RSNP neurons from age-matched (P50-P60) mice: Control (black; n = 6), β2V287L (white, n = 4). The indicated stimuli were applied for 500 ms. No statistical difference was observed between genotypes. (F) Focal application of 5-HT onto the RSNP cell body caused no appreciable whole-cell current response (Vm = -68 mV).

difference between genotypes in firing features (Table 3.1). Finally, RSNP cells generally displayed no response to 100 µM 5-HT focally applied onto the cell soma (Fig. 3.1 F). In conclusion, we classify RSNP cells as a SOM^+ GABAergic population not expressing the ionotropic serotonin receptor 5HT3a (5HT3aR), likely constituted by the Martinotti 'fanning out' group. In fact, the SOM^+ interneurons of cortical layer V can be subdivided into groups based on firing properties and morphology, each showing a specific innervation pattern; the 'fanning out' group targets layer V pyramidal neurons' dendrites in layer II-III (Nigro et al. 2018).

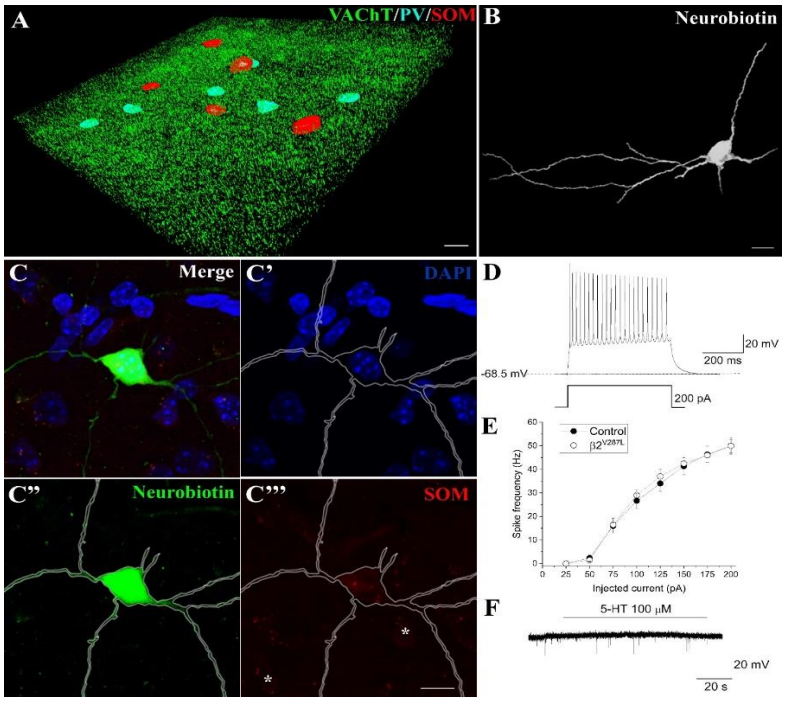

Expression of heteromeric nAChRs on layer V interneurons

Somatic nicotinic currents were identified as inward desensitizing whole-cell currents, at -70 mV. In mice, somatic nicotinic currents in pyramidal and FS neurons are common during the first postnatal month, but progressively subside during the second month (e.g., Aracri et al. 2017). In fact, they were observed in ~20% of pyramidal neurons (with average current amplitudes in the order of 30 pA) and less than 10% of FS cells (average current amplitudes ~15 pA), with scarce difference between genotypes. On the other hand, the sensitivity of synaptic events to nAChR stimulation is maintained in mature prefrontal networks. In pyramidal neurons, a substantial increase of EPSC frequency was observed in both genotypes, in agreement with the wide distribution of α4β2 nAChRs in glutamatergic terminals in Fr2 layer V (Aracri et al. 2013). Nicotine also stimulated IPSC frequency, in pyramidal cells: the increase was ~30% in Control and ~70% in $\beta2^{V287L}$, suggesting that nAChR stimulation was comparatively more effective in dampening pyramidal cell excitability in mice carrying the transgene.

In fact, testing the excitatory input onto FS neurons showed that the basal EPSC frequency in FS neurons was substantially smaller in $\beta2^{V287L}$ and nicotine (10 µM) increased the EPSC frequency in both genotypes, but the effect was considerably stronger in $\beta2^{V287L}$ (approximately +21% in

Control and +56% in $\beta2^{V287L}$), with no significant effect on EPSC amplitudes. So, nicotine produced a stronger stimulus of glutamatergic input onto FS neurons in $\beta2^{V287L}$, which was accompanied by an increased inhibitory input onto pyramidal cells. Hence, nAChR stimulation partly rescues the FS cell deficit observed in prefrontal circuits expressing $\beta2^{V287L}$, thus bringing synaptic balance in layer V closer to the Control level.

Differently from pyramidal and FS neurons, in >90% of RSNP neurons nicotine elicited somatic inward currents with slow desensitization even in mature networks. The average peak whole-cell current densities are plotted in Fig. 3.2 for each genotype. The peak current density in the presence of nicotine was approximately doubled in mice carrying the transgene, which is consistent with the 'gain of function' properties conferred by $\beta2^{V287L}$ on α4β2 nAChRs expressed in heterologous systems (De Fusco et al. 2000; Son et al. 2009; Nichols et al. 2016; Indurthi et al. 2019). To better define the heteromeric nAChRs expressed by RSNP cells, we tested the effect of 1 μM DHβE, which is known to block α4* nAChRs. Differently from what is generally observed in pyramidal and FS cells (Aracri et al. 2010; 2013), 1 μM DHβE did not block the current elicited by nicotine in RSNP cells. Full current block was only obtained by applying 30 μM DHβE (Fig. 3.2 E). The poor sensitivity to DHβE of the nAChRs

expressed in RSNP cells can be interpreted in the light of recent results obtained in mouse neocortex, showing that layer V Martinotti cells mainly express heteromeric α2* nAChRs (Hilscher et al. 2017). This receptor subtype is blocked by DHβE concentrations >10 μM, when tested with 10 μM nicotine (Chavez-Noriega et al. 1997). It can be concluded that RSNP neurons express somatic non-α4* nAChRs up to the adult age, and the ensuing whole-cell nicotinic currents are larger in mice carrying $\beta2^{V287L}$. This effect could increase the inhibition produced by these cells on

pyramidal neurons when the cholinergic tone is high.

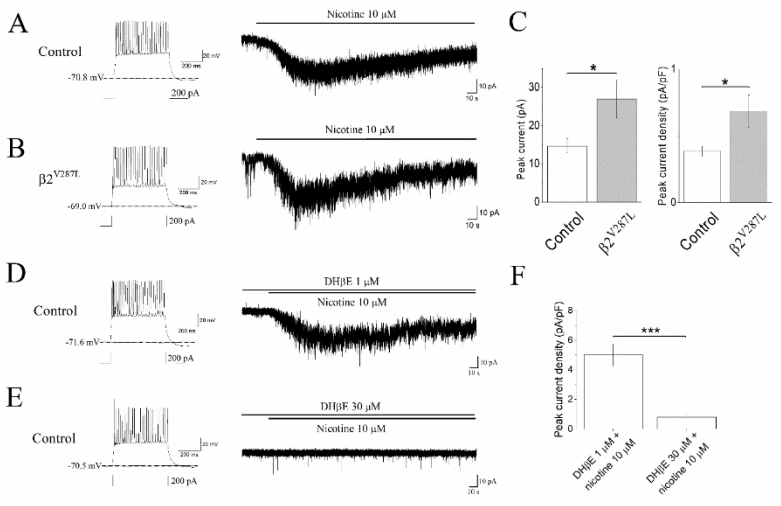

Figure 3.2. Somatic nicotinic currents in RSNP SOM+ cells. A, A Control RSNP neuron was identified by the firing profile (left panel). The current trace (right panel) shows whole-cell continuous recording at -70 mV, in the presence and absence of nicotine (10 µM). Continuous line indicates the time of nicotine application. B, Same as A, in a neuron carrying $\beta2^{V287L}$. C, Left panel: average peak whole-cell currents elicited by 10 µM nicotine on cells from the indicated genotype. Control, 14.7 ± 1.85 pA (n = 14); $\beta2^{V287L}$, 26.9 ± 4.9 pA/pF (n = 12; p = 0.035, unpaired t-test). The corresponding peak current densities are reported in the right panel: Control, 0.386 ± 0.04 pA/pF (n = 14); $\beta2^{V287L}$, 0.687 ± 0.12 pA/pF (n = 12; p = 0.027, with unpaired t-test). D, Same as A, but nicotine was applied in the presence of

Figure 3.2. *(follows)* DHβE (1 μM). Continuous lines indicate the time of DHβE application, and the time during which nicotine (10 μM) was added to DHβE, as indicated. DHβE was unable to block nAChR currents. E, Same as D, but using 30 μM DHβE, as indicated. In the presence of 30 μM DHβE, no evidence of somatic nAChR activation was ever observed in RSNP cells. F, Average peak current densities elicited by 10 μM nicotine, in the presence of 1 μM DHβE (5.0 ± 0.74 pA/pF; n = 7), and 30 μM DHβE (0.81 ± 0.22 pA/pF; n = 10; $p < 0.0001$, unpaired t-test).

Effects of $\beta2^{V287L}$ on neocortical and pyramidal neuron morphology

Neocortex thinning in frontal regions has been observed in children with frontal lobe epilepsy (Lawson et al. 2002; Widjaja et al. 2011; Rahatli et al. 2020), but not investigated in depth in murine models of ADSHE. The analysis of cortical thickness and neuronal populations in mice from P9 to P120 showed that, in SS, thickness was similar in different genotypes, whereas in PFC $\beta2^{V287L}$ presented a ~10% thickness decrease as early as P12 (Fig. 3.3B). The

Figure 3.3. Effect of $\beta2^{V287L}$ on PFC thickness and layer V neuronal population. A, Thionin PFC staining was used for the analysis of cortical thickness and cell count. Roman numbers indicate cortical layers, in PFC of a Control mouse (P60). Calibration bar: 100 μm. B, Average PFC thickness in Control and $\beta2^{V287L}$, at the indicated postnatal ages. A significant decrease was observed since P12 in $\beta2^{V287L}$. P9: 1349.3 ± 40.4 μm (Control) and 1293.7 ± 41.4 μm ($\beta2^{V287L}$; NS with unpaired t-test; n = 5 mice per genotype); P12: 1418.4 ± 20.1 μm (Control) and 1311.5 ± 19.2 μm ($\beta2^{V287L}$, **p = 0.0085 with t-test; n = 4 mice per genotype); P60: 1437.1 ± 24.3 μm (Control) and 1294.9 ± 41.9 μm ($\beta2^{V287L}$, *p = 0.0189 with t-test; n = 5 mice per genotype); P120: 1421.9 ± 3.0 μm (Control) and 1318.8 ± 14.98 μm ($\beta2^{V287L}$, **p = 0.0016 with t-test; n = 4 mice per genotype). For comparison, the corresponding values in SS at P60 were: Control: 1300 ± 49 μm, $\beta2^{V287L}$: 1310 ± 57 μm (NS with unpaired t-test; n = 5 mice per genotype). C, As in A, but at a higher magnification to highlight layer V. Neurons were counted by

quantification of the neuronal populations in layer V at P60, by stereological cell counts on sections stained with thionine to estimate the total neuronal population on the whole section volume showed in both SS and PFC no significant differences were observed between genotypes.

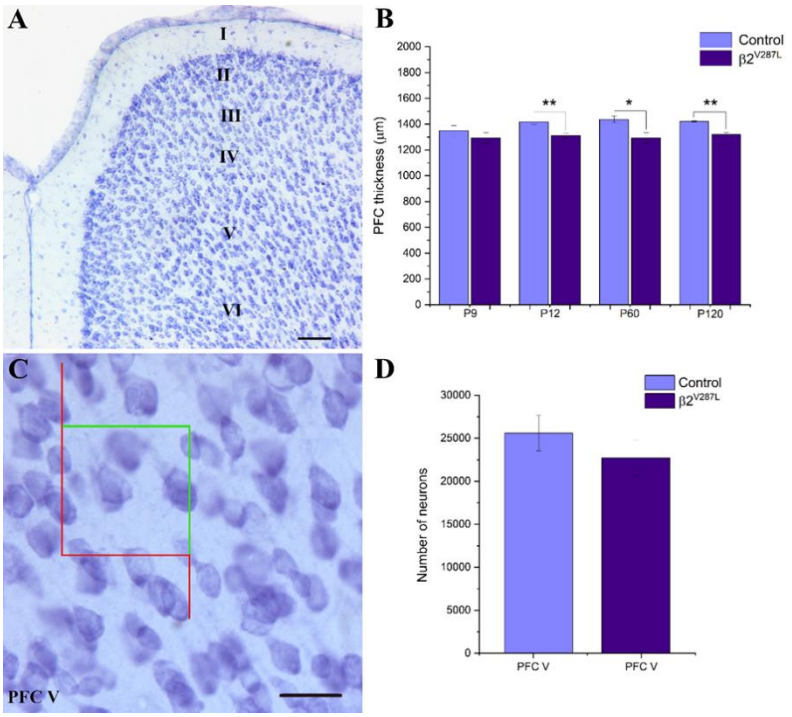

Figure 3.3. *(follows)* stereology. Calibration bar: 25 µm. D, Neuronal counts in PFC layer V of Control and $\beta2^{V287L}$ (P60): Control, 25667 ± 2000; $\beta2^{V287L}$, 22730 ± 2136 (NS with unpaired t-test; n = 5 mice per genotype). For comparison, in SS we estimated 61250 ± 3190 neurons in Control and 58000 ± 4255 in β2V287L (NS with unpaired t-test; n = 5 mice per genotype). The higher cell count in SS is consistent with previous observations in mammals (e.g., Charvet et al, 2015).

In parallel, I have investigated the alterations in dendrite morphology and spine density of Pys by FIJI analysis on confocal stacks of Golgi-Cox stained thick sections. In Fr2 layers II-III and V, Sholl analysis of dendrite arbors shows a tendency towards a decrease in complexity (measured as intersections per radius length of the imaginary sphere centred on the soma, Fig. 3.4, and Schönen ramification index, Fig. 3.5) in transgenic mice but unaltered spine density over dendrite length (Fig. 3.6). The data on primary somatosensory cortex (barrel field), as a control region, highlight a similar tendency for ramification index and a reduction in distal spine density in layer II-III of transgenic mice (p-value = 0.0001, two-way ANOVA with genotype as factor, Fig. 3.6). These results suggest that $\beta2^{V287L}$* nAChRs may decrease the dendrite complexity and modify the dendritic spine density with different patterns according to cortical region. This points to a still poorly defined role of β2* nAChRs in the morphofunctional maturation of cortical Py, with possible implications in network pathology. This probable reduction in dendrite complexity could also be connected to the decrease in PFC thickness in $\beta2^{V287L}$ mice.

Figure 3.4. Effect of $\beta2^{V287L}$ on Py's dendritic arborization complexity in Fr2 and in SS1 cortex – Sholl Analysis. Data points represent the number of intersections with dendrites within spherical shells at increasing distance from the soma. (A) Fr2 layer II-III (WT: 21 cells from 4 mice; $\beta2^{V287L}$: 22 cells from 3 mice), (B) Fr2 layer V III (WT: 20 cells from 4 mice; $\beta2^{V287L}$: 25 cells from 3 mice) (C) SS1 barrel field layer II-III (WT: 39 cells from 4 mice; $\beta2^{V287L}$: 19 cells from 2 mice) (D) SS1 barrel field layer V (WT: 37 cells from 4 mice; $\beta2^{V287L}$: 21 cells from 2 mice).

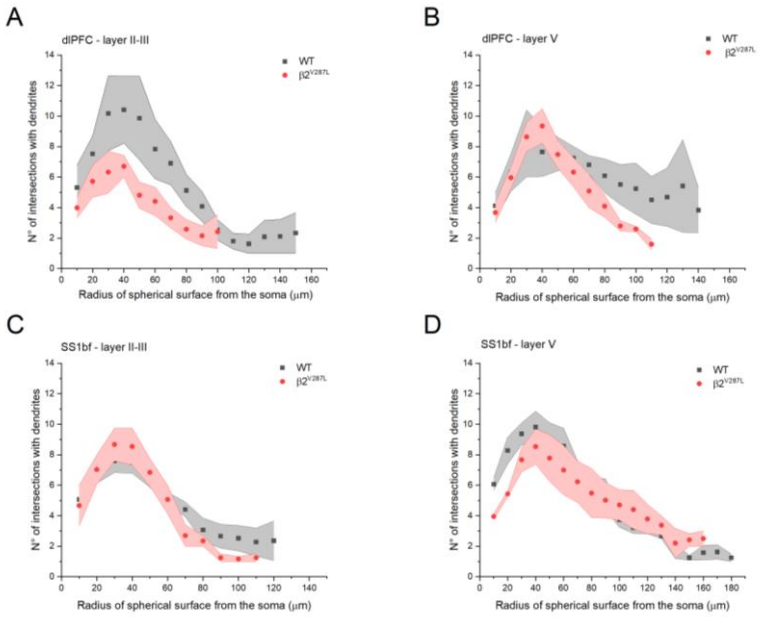

Figure 3.5. Effect of $\beta2^{V287L}$ on Py's dendritic arborization complexity in Fr2 and in SS1 cortex – Schönen Ramification Index (RI). RI is a measure of ramification given by the ratio between the max number of intersections found by Sholl analysis and the number of primary branches of the dendritic tree. (A) RI in Fr2 layer II-III and V (same cells as in 3.4) (B) RI in SS1 – bf layer II-III and V (same cells as in 3.4).

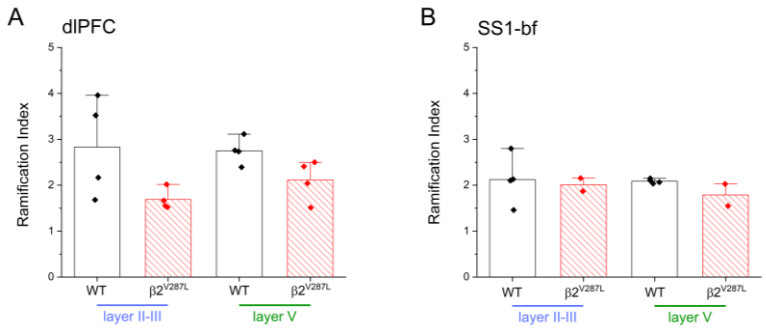

Figure 3.6. Effect of $\beta2^{V287L}$ on Py's dendritic spine density in Fr2 and in SS1 cortex. The spine density is reported as a data point each 10 µm of dendrite length. (A) Fr2 layer II-III (WT: 15 cells from 4 mice; $\beta2^{V287L}$: 13 cells from 4 mice) (B) Fr2 layer V (WT: 16 cells from 4 mice; $\beta2^{V287L}$: 16 cells from 4 mice) (C) SS1 – bf layer II-III (WT: 23 cells from 4 mice; $\beta2^{V287L}$: 13 cells from 2 mice) In the distal dendrites the spine density is significantly reduced, indicating a possible synaptic deficit in this area (p-value = 0,0001, ANOVA) (D) SS1 – bf layer V (WT: 29 cells from 4 mice; $\beta2^{V287L}$: 17 cells from 2 mice).

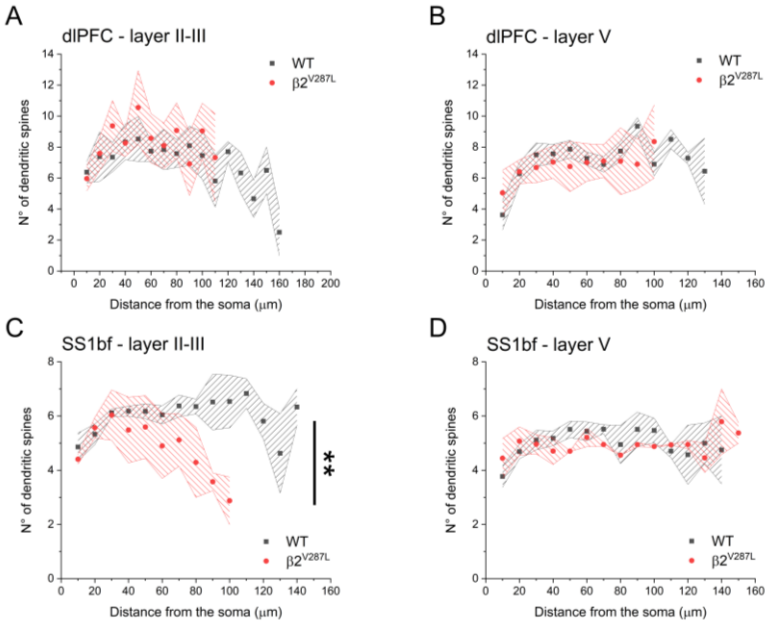

Discussion

We analysed synaptic transmission and excitability in prefrontal layer V, in a murine model of ADSHE that displays a central feature of the human pathology, namely sleep-related seizures. Expression of $\beta2^{V287L}$ throughout development led to a selective modification of the glutamatergic input on layer V FS cells, which was accompanied by a higher sensitivity of regular spiking Martinotti cells to nAChR activation. These functional alterations were associated to prefrontal network hyperexcitability and spontaneous sleep-related seizures (Manfredi et al. 2009). In analogy with other ADSHE models, mice carrying the transgene did not show major morphological changes in the brain, but for a surprising ~10% decrease of PFC thickness, which resembles the frontal cortex thinning observed in young patients (Lawson et al. 2002; Widjaja et al. 2011; Rahatli et al. 2020).

The possible role of α2 nAChRs in ADSHE seizures*

The results shown in the present chapter are relevant in the context of the evidence discussed earlier about the implication in sleep-related epilepsy of mutations on CHRNA2, coding for the α2 nAChR subunit (Aridon et al. 2006; Conti et al. 2015; Villa et al. 2019).

Recent work that PV^+ and SOM^+ GABAergic neurons cooperate in controlling feedforward inhibition at the front of epileptiform waves in vitro (Parrish et al. 2019). We found that, differently from FS cells, somatic nicotinic currents are detectable in the vast majority of SOM^+ RSNP cells, and their amplitude was larger in cells carrying $\beta2^{V287L}$. Hence, nAChR activation can potentiate the inhibition produced by these cells on pyramidal cell dendrites. Moreover, the effect of nicotine on RSNP cells was weakly sensitive to DHβE, which shows that non-α4 nAChRs are expressed by these neurons. In fact, recent work demonstrated that α2* nAChRs are selectively expressed in layer V Martinotti cells (Hilscher et al. 2017), at least in mice. Hence, the simplest interpretation of our results is that in RSNP cells β2 mainly participates in α2β2 receptors, although specific antagonists for this nAChR subtype are not available. Nevertheless, the present observations point to layer V SOM^+ GABAergic neurons as possible culprits of α2-dependent ADSHE. A possible explanation is that loss-of-function α2* nAChRs could decrease the efficacy of pyramidal cell inhibition produced by SOM^+ cells, thus partially disinhibiting the local network. Whether the effect of α2* nAChRs could be exerted during network maturation, to produce permanent circuit alteration, remains to be determined.

References

Amadeo, A., Coatti, A., Aracri, P., Ascagni, M., Iannantuoni, D., Modena, D., ... & Becchetti, A. (2018). Postnatal changes in K+/Cl− cotransporter-2 expression in the forebrain of Mice Bearing a Mutant Nicotinic Subunit Linked to Sleep-Related Epilepsy. Neuroscience, 386, 91-107.

Aracri, P., Amadeo, A., Pasini, M. E., Fascio, U., & Becchetti, A. (2013). Regulation of glutamate release by heteromeric nicotinic receptors in layer V of the secondary motor region (Fr2) in the dorsomedial shoulder of prefrontal cortex in mouse. Synapse, 67, 338-357.

Aracri, P., Consonni, S., Morini, R., Perrella, M., Rodighiero, S., Amadeo, A., & Becchetti, A. (2010). Tonic modulation of GABA release by nicotinic acetylcholine receptors in layer V of the murine prefrontal cortex. Cerebral Cortex, 20, 1539-1555.

Aracri, P., Meneghini, S., Coatti, A., Amadeo, A., Becchetti, A. (2017). A4β2* nicotinic receptors stimulate GABA release onto fast-spiking cells in layer V of mouse prefrontal (Fr2) cortex. Neuroscience, 340, 48-61.

Aridon, P., Marini, C., Di Resta, C., Brilli, E., De Fusco, M., Politi, F., ... & Casari, G. (2006). Increased sensitivity of the neuronal nicotinic receptor α2 subunit causes familial epilepsy with nocturnal wandering and ictal fear. The American Journal of Human Genetics, 79, 342-350.

Bailey, C. D., Alves, N. C., Nashmi, R., De Biasi, M., & Lambe, E. K. (2012). Nicotinic α5 subunits drive developmental changes in the activation and morphology of prefrontal cortex layer VI neurons. Biological psychiatry, 71, 120-128.

Becchetti, A., Aracri, P., Meneghini, S., Brusco, S., & Amadeo, A. (2015). The role of nicotinic acetylcholine receptors in autosomal dominant nocturnal frontal lobe epilepsy. Frontiers in physiology, 6, 22.

Cammarota, M., Losi, G., Chiavegato, A., Zonta, M., & Carmignoto, G. (2013). Fast spiking interneuron control of seizure propagation

in a cortical slice model of focal epilepsy. The Journal of physiology, 591, 807-822.

Chavez-Noriega, L. E., Crona, J. H., Washburn, M. S., Urrutia, A., Elliott, K. J., & Johnson, E. C. (1997). Pharmacological characterization of recombinant human neuronal nicotinic acetylcholine receptors hα2β2, hα2β4, hα3β2, hα3β4, hα4β2, hα4β4 and hα7 expressed in Xenopus oocytes. Journal of Pharmacology and Experimental Therapeutics, 280, 346-356.

Conti, V., Aracri, P., Chiti, L., Brusco, S., Mari, F., Marini, C., ... & Guerrini, R. (2015). Nocturnal frontal lobe epilepsy with paroxysmal arousals due to CHRNA2 loss of function. Neurology, 84, 1520-1528.

De Fusco, M., Becchetti, A., Patrignani, A., Annesi, G., Gambardella, A., Quattrone, A., ... & Casari, G. (2000). The nicotinic receptor β2 subunit is mutant in nocturnal frontal lobe epilepsy. Nature genetics, 26, 275-276.

Franklin, K.B.J. & Paxinos, G. (2008). The Mouse Brain in Stereotaxic Coordinates, third ed. Elsevier Academic Press, San Diego.

Fukuyama, K., Fukuzawa, M., Shiroyama, T., & Okada, M. (2020). Pathogenesis and pathophysiology of autosomal dominant sleep-related hypermotor epilepsy with S284L-mutant α4 subunit of nicotinic ACh receptor. British journal of pharmacology, 177, 2143-2162.

Hilscher, M. M., Leão, R. N., Edwards, S. J., Leão, K. E., & Kullander, K. (2017). Chrna2-Martinotti cells synchronize layer 5 type A pyramidal cells via rebound excitation. PLoS biology, 15, e2001392.

Indurthi, D. C., Qudah, T., Liao, V. W., Ahring, P. K., Lewis, T. M., Balle, T., ... & Absalom, N. L. (2019). Revisiting autosomal dominant nocturnal frontal lobe epilepsy (ADNFLE) mutations in the nicotinic acetylcholine receptor reveal an increase in efficacy regardless of stochiometry. Pharmacological research, 139, 215-227.

Jones, B.E., (2020). Arousal and sleep circuits. Neuropsychopharmacology, 45, 6-20.

Klaassen, A., Glykys, J., Maguire, J., Labarca, C., Mody, I., & Boulter, J. (2006). Seizures and enhanced cortical GABAergic inhibition in two mouse models of human autosomal dominant nocturnal frontal lobe epilepsy. Proceedings of the National Academy of Sciences, 103, 19152-19157.

Lawson, J. A., Cook, M. J., Vogrin, S., Litewka, L., Strong, D., Bleasel, A. F., & Bye, A. M. E. (2002). Clinical, EEG, and quantitative MRI differences in pediatric frontal and temporal lobe epilepsy. Neurology, 58, 723-729.

Lozada, A. F., Wang, X., Gounko, N. V., Massey, K. A., Duan, J., Liu, Z., & Berg, D. K. (2012). Induction of dendritic spines by β2-containing nicotinic receptors. Journal of Neuroscience, 32, 8391-8400.

Manfredi, I., Zani, A. D., Rampoldi, L., Pegorini, S., Bernascone, I., Moretti, M., ... & Casari, G. (2009). Expression of mutant β2 nicotinic receptors during development is crucial for epileptogenesis. Human molecular genetics, 18, 1075-1088.

McLaughlin, T., Torborg, C. L., Feller, M. B., & O'Leary, D. D. (2003). Retinotopic map refinement requires spontaneous retinal waves during a brief critical period of development. Neuron, 40, 1147-1160.

Molas, S., & Dierssen, M. (2014). The role of nicotinic receptors in shaping and functioning of the glutamatergic system: A window into cognitive pathology. Neuroscience & Biobehavioral Reviews, 46, 315-325.

Nichols, W. A., Henderson, B. J., Marotta, C. B., Yu, C. Y., Richards, C., Dougherty, D. A., ... & Cohen, B. N. (2016). Mutation linked to autosomal dominant nocturnal frontal lobe epilepsy reduces low-sensitivity α4β2, and increases α5α4β2, nicotinic receptor surface expression. PloS one, 11, e0158032.

Nigro, M. J., Hashikawa-Yamasaki, Y., & Rudy, B. (2018). Diversity and connectivity of layer 5 somatostatin-expressing interneurons in the mouse barrel cortex. Journal of Neuroscience, 38, 1622-1633.

O'Neill, H. C., Laverty, D. C., Patzlaff, N. E., Cohen, B. N., Fonck, C., McKinney, S., ... & Marks, M. J. (2013). Mice expressing the ADNFLE valine 287 leucine mutation of the β2 nicotinic

acetylcholine receptor subunit display increased sensitivity to acute nicotine administration and altered presynaptic nicotinic receptor function. Pharmacology Biochemistry and Behavior, 103, 603-621.

Parrish, R. R., Codadu, N. K., Mackenzie-Gray Scott, C., & Trevelyan, A. J. (2019). Feedforward inhibition ahead of ictal wavefronts is provided by both parvalbumin-and somatostatin-expressing interneurons. The Journal of physiology, 597, 2297-2314.

Picciotto, M. R., Higley, M. J., & Mineur, Y. S. (2012). Acetylcholine as a neuromodulator: cholinergic signaling shapes nervous system function and behavior. Neuron, 76, 116-129.

Rahatli, F. K., Sezer, T., Has, A. C., & Agildere, A. M. (2020). Evaluation of cortical thickness and brain volume on 3 Tesla magnetic resonance imaging in children with frontal lobe epilepsy. Neurological Sciences, 41, 825-833.

Rossi, F. M., Pizzorusso, T., Porciatti, V., Marubio, L. M., Maffei, L., & Changeux, J. P. (2001). Requirement of the nicotinic acetylcholine receptor β2 subunit for the anatomical and functional development of the visual system. Proceedings of the National Academy of Sciences, 98, 6453-6458.

Shiba, Y., Mori, F., Yamada, J., Migita, K., Nikaido, Y., Wakabayashi, K., ... & Ueno, S. (2015). Spontaneous epileptic seizures in transgenic rats harboring a human ADNFLE missense mutation in the β2-subunit of the nicotinic acetylcholine receptor. Neuroscience research, 100, 46-54.

Sholl, D. A. (1953). Dendritic organization in the neurons of the visual and motor cortices of the cat. Journal of anatomy, 87, 387.

Son, C. D., Moss, F. J., Cohen, B. N., & Lester, H. A. (2009). Nicotine normalizes intracellular subunit stoichiometry of nicotinic receptors carrying mutations linked to autosomal dominant nocturnal frontal lobe epilepsy. Molecular pharmacology, 75, 1137-1148.

Steinlein, O. K., Mulley, J. C., Propping, P., Wallace, R. H., Phillips, H. A., Sutherland, G. R., ... & Berkovic, S. F. (1995). A missense mutation in the neuronal nicotinic acetylcholine receptor α4 subunit

is associated with autosomal dominant nocturnal frontal lobe epilepsy. Nature genetics, 11, 201-203.

Teper, Y., Whyte, D., Cahir, E., Lester, H. A., Grady, S. R., Marks, M. J., ... & Drago, J. (2007). Nicotine-induced dystonic arousal complex in a mouse line harboring a human autosomal-dominant nocturnal frontal lobe epilepsy mutation. Journal of Neuroscience, 27, 10128-10142.

Tremblay, R., Lee, S., & Rudy, B. (2016). GABAergic interneurons in the neocortex: from cellular properties to circuits. Neuron, 91, 260-292.

Trevelyan, A. J., Sussillo, D., Watson, B. O., & Yuste, R. (2006). Modular propagation of epileptiform activity: evidence for an inhibitory veto in neocortex. Journal of Neuroscience, 26, 12447-12455.

Villa, C., Colombo, G., Meneghini, S., Gotti, C., Moretti, M., Ferini-Strambi, L., ... & Combi, R. (2019). CHRNA2 and nocturnal frontal lobe epilepsy: Identification and characterization of a novel loss of function mutation. Frontiers in molecular neuroscience, 12, 17.

Widjaja, E., Mahmoodabadi, S. Z., Snead III, O. C., Almehdar, A., & Smith, M. L. (2011). Widespread cortical thinning in children with frontal lobe epilepsy. Epilepsia, 52, 1685-1691.

Xu, J., Cohen, B. N., Zhu, Y., Dziewczapolski, G., Panda, S., Lester, H. A., ... & Contractor, A. (2011). Altered activity–rest patterns in mice with a human autosomal-dominant nocturnal frontal lobe epilepsy mutation in the β2 nicotinic receptor. Molecular psychiatry, 16, 1048-1061.

Zhu, G., Okada, M., Yoshida, S., Ueno, S., Mori, F., Takahara, T., ... & Hirose, S. (2008). Rats harboring S284L Chrna4 mutation show attenuation of synaptic and extrasynaptic GABAergic transmission and exhibit the nocturnal frontal lobe epilepsy phenotype. Journal of Neuroscience, 28, 12465-12476.

PART II. The orexinergic system and narcolepsy with cataplexy

The orexinergic system

Orexin A and B (Sakurai et al. 1998; Orx), also known as hypocretin 1 and 2 (de Lecea et al. 1998), are neuropeptides produced by a group of neurons in the lateral and posterior hypothalamus (Sakurai, 2007). Orexins act through G protein coupled receptors (Ox1R and 2R), leading to intracellular second messenger cascades, such as protein kinase C activation (Kukkonen and Leonard, 2014), which in turn regulate neuronal activity e. g. by inhibiting voltage-gated K^+ channels (Xia et al. 2005) or hyperpolarization-activated HCN channels (Li et al. 2010). Ox1R preferentially binds OrxA (with an EC_{50} of 30 nM, compared to OrxB with 2.5 μM EC_{50} value), while Ox2R indistinctly binds both OrxA and B (with, respectively, 34 nM and 60 nM EC_{50} values; Ammoun et al. 2003; Sakurai, et al. 1998). The overall OrxRs distribution is complex and depends on brain area and cell type. In the rat brain, they have a widespread and partly overlapping pattern of expression (Hervieu et al. 2001; Marcus et al. 2001).

The orexins were initially implicated in feeding behaviour, but they were also found to regulate cortical arousal and the sleep/wake cycle. Orx neurons discharge during active

waking and cease firing during sleep (Lee et al. 2005; Mileykovskiy et al. 2005; Jones, 2008). Their axons innervate the brain ascending activating system nuclei in brainstem, basal forebrain, and hypothalamus (Peyron et al. 1998; Hagan et al. 1999; Horvath et al. 1999; Bayer et al. 2001; Eggermann et al. 2001; Eriksson et al. 2001; Liu et al. 2002; Yamanaka et al. 2002). More precisely, the orexins excite all the subcortical arousal nuclei (Sutcliffe and de Lecea, 2002), thereby increasing the release of cortical neuromodulators, such as ACh (Fadel et al. 2005). Moreover, Orx neurons directly regulate wakefulness: selective optogenetic stimulation of these cells in the lateral hypothalamus induces an increase in awakening probability (Adamantidis et al. 2007). Wide evidence assigns to orexins a role in arousal, feeding behaviour, metabolic regulation, and stress response (Sakurai et al. 1998; Sakurai 2007; Boutrel et al. 2010; Kukkonen, 2013). A possible unifying hypothesis is that Orx neurons contribute to set the proper level of arousal necessary for exploratory and goal-oriented behaviours, in response to different physiological or psychological drives (Boutrel et al. 2010).

Narcolepsy with cataplexy and orexinergic transmission

Narcolepsy with cataplexy (also called narcolepsy type 1) is a neurological disease specifically affecting normal sleep architecture by causing two major symptoms: cataplexy and excessive daytime sleepiness (EDS). Cataplexy is defined as a sudden loss of muscle tone during wakefulness (Vassalli, et al. 2013; Scammell, 2015) and is triggered by strong emotions (e.g., laughter in humans, sound of a barking dog in sheep, food in dogs, or exploration and exposure to palatable treats in mice and rats; Blouin, et al. 2013). Narcolepsy with cataplexy affects up to 0.05% of the adult population in the world (Dauvilliers, et al. 2014).

A disputed hypothesis interprets cataplexy as the outcome of a dysregulation of rapid eye movement (REM) sleep since its abrupt intrusion in normal wakefulness results in a state with similarities to REM sleep, albeit with preserved consciousness (Adamantidis, et al. 2020). EDS on the other hand can be considered as a dysregulation of NREM sleep which manifests as inability to maintain stable vigilance with irresistible sleepiness during the day, culminating in so-called sleep attacks (Vassalli, et al. 2013; Hasegawa, et al. 2014; Dauvilliers, et al. 2007). Although EDS can lead to sleep onset REM periods (SOREMPs) in other conditions and even

in normal subjects, the occurrence of SOREMPs in narcolepsy and direct REM episodes in animal models of narcolepsy, results from abnormal transitions between vigilance states (Broughton, et al. 1986; Schoch, et al. 2017) and remains unaffected by successful treatment of EDS by stimulants. Therefore, the neural mechanisms underlying cataplexy and EDS appear to be different.

The disruption of orexin system leads to narcolepsy with cataplexy in humans as well as in animal models (Chemelli, et al. 1999; Lin, et al. 1999; Peyron, et al. 2000; Thannickal, et al. 2000; Gerashchenko, et al. 2003). In fact, nearly all narcoleptic patients were found to have a low or undetectable level of OrxA peptide in the cerebrospinal fluid, establishing Orx signalling as a major player in the control of wakefulness and cataplexy protection, and narcolepsy as a result of the loss of $OrxA^{+}$ neurons in the lateral hypothalamus in animal models (Peyron, et al. 2000; Liblau, et al. 2015; Nishino, et al. 2000).

Cataplexy is the pathognomonic and most striking symptom of narcolepsy. It has originally been, and still is now, widely considered as an abnormal manifestation of REM sleep during wakefulness due to the typical muscle atonia. The neurocircuits of cataplexy, originally confined to the brainstem as those of REM sleep atonia, now include the

hypothalamus, dorsal raphe, amygdala and frontal cortex, and its neurochemistry, originally focused on catecholamines and acetylcholine, now includes orexin and other neuromodulators.

In the canine model, the genetic loss-of-function of Ox2R causes cataplexy, while pharmacology shows that noradrenergic hypoactivity is a key component of cataplexy regulation (with noradrenergic agonists improving and antagonists aggravating the dogs' cataplexies). However, NA neurons do not express Ox2R, but rather Ox1R in the dog. It's been shown that decreased NA tone can be a major factor in aggravating cataplexy, but it is not sufficient to cause it (Burgess & Peever, 2013), suggesting the involvement of other neurotransmitters such as 5-HT, DA, GABA or glycine. A possible explanation would be that a yet unidentified cell group, critically controlled by Ox2R signalling, is necessary for NA activation. Nonetheless, why Ox1R malfunction is insufficient to cause cataplexy remains to be explained (Seifinejad et al. 2021).

Other studies shifted the spotlight from NA onto serotonergic neurons as major Orx effectors in the pathophysiology of narcolepsy with cataplexy, while further establishing the fundamental difference between cataplexy and REM sleep. To test whether an increase in 5-HT levels could rescue the

symptoms of Orx-deficient narcoleptic mice, Seifinejad et al. (2020), inactivated the serotonin transporter in an Orx null background: these mice displayed a profound decrease in cataplexy incidence, while time spent in REM sleep was markedly increased. In the same study, acute deletion of Orx receptors in the dorsal raphe consolidated REM sleep, but did not induce cataplexy, which indicated that additional pathways are necessary to trigger cataplexy in normal mice, while suppressing cataplexy in narcoleptic mice could be achieved by ablating a single pathway. Regulations of cataplexy and REM sleep can therefore be dissociated and operate in opposite manner (Seifinejad et al. 2021).

As for the dopaminergic contribution, both Orx receptors are expressed in the ventral tegmental area (VTA), one of the major brain regions to contain dopaminergic cell bodies (Lu, et al. 2000; Korotkova, et al. 2003) and anatomical studies suggest that Orx neurons regulate DA neurons via LH-to-VTA projections (Fadel & Deutch, 2002). Blockers of the dopamine transporter, such as cocaine, increase extracellular DA and have potent wake-promoting activity, and activation of dopaminergic cells in the VTA triggers locomotor activity associated with strong arousal. In vitro, application of OrxA results in increased firing frequency of dopaminergic and non-dopaminergic cells within the VTA (Korotkova, et al. 2003; Wisor, et al. 2001). It's been repeatedly shown, in narcoleptic

dogs, that agonists or antagonists of central D2 receptors, respectively, aggravate or suppress cataplexy without affecting REM sleep (Nishino, et al. 1991; Reid, et al. 1996; Okura, et al. 2000). Because D2/D3 receptors are inhibitory, and can act as autoreceptors on dopaminergic cells, and indeed local administration of D2/D3 agonists into the VTA is known to reduce the firing rate of dopaminergic neurons, these observations suggested that dopamine might have a protective role on cataplexy. In further support of this concept, Burgess et al. (2010) reported that pharmacological activation of D2-like receptors in $Orx^{KO/KO}$ mice increased cataplectic attacks, and blockade of the same receptors suppressed them. The latter study furthermore demonstrated that cataplexies and sleep attacks are differentially modulated by dopaminergic transmission, as D2/D3 drugs had no effect on sleep attacks, whereas the activation, or blockade of D1-like receptors, respectively, decreased or increased sleep attacks, without affecting cataplexies. Altogether these results hinted to a pronounced role of D2-like receptors in the pathophysiology of cataplexy. But since the effects of D2-like receptors were seen in narcoleptic dogs with a loss-of-function of Ox2R, or in $Orx^{KO/KO}$ mice, these effects appear to be independent of Orx signaling. Unlike Orx neuron-ablated mice, $Orx^{KO/KO}$ mice are however known to host cells with an otherwise Orx neuronal identity, therefore

dopaminergic receptors may be acting through other neurotransmitters produced by Orx neurons, such as glutamate or dynorphin. Alternatively, D2/D3 receptors might be acting downstream of Orx neurons, which remain the cell population at the core of any scenario of cataplexy induction (Vassalli, et al. 2021).

The GABAergic transmission, too, seems to have a role in cataplexy: $GABA_B$ agonists decrease cataplexy, suggesting a protective role of GABA neurotransmission in the control of cataplexy (Black, et al. 2014). The site of action of these drugs is unknown but may be speculated to be the amygdala as reported in a study showing that activation of GABA neurons within the central amygdala produced a marked increase in cataplexy attacks. However, this effect was mainly on cataplexy numbers rather than duration, indicating again that cataplexy initiation and maintenance are differentially regulated (Snow, et al. 2017). It can also be concluded that serotonin neurons in the DR mediate the anticataplectic action of Orx neurons by reducing the activity of GABA cells within central amygdala (Hasegawa, et al. 2017; Snow, et al. 2017). Moreover, while dopaminergic neurons of the *pars compacta* portion of the substantia nigra may not respond to orexins (Korotkova, et al. 2002), GABAergic cells of the substantia nigra pars reticulata were shown to be strongly excited by OrxA and B. The latter cells seem important for the

regulation of muscle tone and discharge at high frequency during both wakefulness and REM sleep. Activation of these neurons by Orxs potentially explains their fast firing rate during wake, and lower excitability in individuals lacking Orx may result in cataplexy. Fine-tuning of these GABAergic neurons of the reticulate part of substantia nigra seems to be essential, as their hyperexcitability leads to another pathology called catalepsy, characterized by muscle rigidity and inability to initiate movement (Boulay, et al. 2000). Another study also showed that there is a small number of neurons in the reticular formation that are positive for both GAD and Ox2R. Orx may thus excite these locally or caudally projecting GABAergic neurons to hold REM sleep effector neurons under inhibition during wakefulness (Brischoux, Mainville & Jones, 2008).

Theta-dominated wakefulness and cataplexy

Recently, Anne Vassalli and Paul Franken have algorithmically identified a theta-dominated wakefulness (TDW) substate underlying motivated behaviours and typically preceding cataplexy in $Orx^{KO/KO}$ mice. They reformulated the classic sleep homeostasis model by linking the rise of homeostatic pressure exclusively to TDW rather than to all waking, and this approach can predict δ power dynamics both in $Orx^{KO/KO}$ and WT mice. They demonstrated

that spontaneous TDW stability relies on Orx to sustain θ/fast-γ network activity and associated plasticity, whereas other arousal circuits sustain TDW during sleep deprivation (Vassalli & Franken, 2017). Therefore, TDW can be identified as a discrete global brain activity mode that is regulated by context-dependent neuromodulators and acts as a major driver of sleep homeostasis. In fact, Orx loss in $Orx^{KO/KO}$ mice, which mimics the orexin depletion associated to narcolepsy, causes impaired TDW maintenance in baseline wake and blunted δ power in SWS, reproducing, respectively, excessive daytime sleepiness and poor sleep quality seen in narcolepsy.

Recently, several lines of evidence introduced new neural substrates for cataplexy, such as the PFC and the amygdala. Using EEG and in-depth recording analysis of the brain activity of $Orx^{KO/KO}$ mice, the occurrence of stereotypical ~2-s-long very high-amplitude hypersynchronous paroxysmal theta (HSPT) bursts was uncovered in the PFC of mice at the onset of cataplexy attacks, preceding the hippocampal θ activity commonly associated with cataplexy and REM sleep (Vassalli, et al. 2013). This finding suggested that cataplexy is not simply the sudden emergence of REM sleep into wakefulness, but it also implicates paroxysmal cortical oscillations, suggestive of a cortical microcircuit deregulation. Similar paroxysmal θ bursting events were evidenced during

cataplexy attacks of narcoleptic children. This study raised the question of the circuits involved in these early cataplexy cortical hypersynchronies, as the mPFC is known to be densely innervated directly by Orx neurons (Peyron, et al. 1998). Involvement of the mPFC was confirmed using a different approach whereby palatable foods, such as chocolate, markedly increased cataplexy incidence in $Orx^{KO/KO}$ mice, and activated neurons in mPFC. Strikingly, when mPFC neuronal activity was repressed by the expression of an engineered chloride channel, chocolate-induced cataplexies were substantially reduced while spontaneous cataplexies appeared unaffected (Oishi, et al. 2013). The involvement of the amygdala in cataplexy onset was demonstrated, on the other hand, by anterograde and retrograde tracing in mice, which showed that neurons important for the maintenance of motor tone during wakefulness, such as ventrolateral periaqueductal gray, LC and DR cells, are innervated by GABAergic neurons from the central nucleus of the amygdala (Burgess, et al. 2013). Amygdala lesions markedly reduced the cataplexy events of $Orx^{KO/KO}$ mice, in particular in conditions associated with high arousal and positive emotions. Altogether these data substantiate the importance of the PFC and the amygdala in cataplexy pathophysiology. This raises the question as to whether impaired Orx signalling directly deregulates PFC

functioning, or the involvement of the PFC is secondary, and due to the lack of normal projections of Orx to the brainstem resulting in altered PFC-brainstem circuits (Vassalli, et al. 2021). In fact, narcoleptic patients display specific attention deficits related to the prefrontal executive functions that cannot be merely attributed to sleepiness (Rieger, et al. 2003).

Since all the above-mentioned pathways strongly affect cataplexy, one may wonder why, amongst the six major known wake-promoting neurotransmitters, the lack of only one of them generates cataplexy in narcolepsy subjects. DA, NA, HA, 5HT, ACh and Orx neurons all organize a widely diverging axonal network to broadcast the information that a salient context necessitates a resetting of arousal. ACh is particular in that cholinergic neurons are both wake- and REM sleep-active. Mice selectively lacking DA cells are severely hypoactive and behaviourally apathic (Zhou & Palmiter, 1995). Mice lacking HA have reduced EEG θ oscillations in wakefulness and a profoundly reduced vigilance (Parmentier, et al. 2002). As θ-dominated wakefulness (TDW) appears to be the obligatory trigger for cataplexy (Vassalli, et al. 2013), it is not surprising that apathetic mice do not exhibit cataplexy. On the other hand, $Orx^{KO/KO}$ mice are perfectly able to spontaneously express enhanced arousal and enter the TDW state, even though TDW bouts are pronouncedly shorter.

Thus, Orx is necessary for TDW to last and maintain coupling to muscle tone. Cataplexy being the signature of Orx loss, it is tempting to speculate that although the DA, NA, HA, 5-HT, and Orx connectomes are all wake-active and essentially silent during sleep, they may induce distinct arousal states, and Orx neuronal activation mediates a unique state transition (Seifinejad et al. 2021).

References

Adamantidis, A. R., Schmidt, M. H., Carter, M. E., Burdakov, D., Peyron, C., & Scammell, T. E. (2020). A circuit perspective on narcolepsy. Sleep, 43, zsz296.

Aracri, P., Banfi, D., Pasini, M.E., Amadeo, A., & Becchetti, A. (2015). Orexin (hypocretin) regulates glutamate input to fast-spiking interneurons in layer V of the Fr2 region of the murine prefrontal cortex. Cerebral Cortex, 25, 1330-1347.

Black, S. W., Morairty, S. R., Chen, T. M., Leung, A. K., Wisor, J. P., Yamanaka, A., & Kilduff, T. S. (2014). GABAB agonism promotes sleep and reduces cataplexy in murine narcolepsy. Journal of Neuroscience, 34, 6485-6494.

Blouin, A. M., Fried, I., Wilson, C. L., Staba, R. J., Behnke, E. J., Lam, H. A., ... & Siegel, J. M. (2013). Human hypocretin and melanin-concentrating hormone levels are linked to emotion and social interaction. Nature communications, 4, 1-9.

Boulay, D., Depoortere, R., Oblin, A., Sanger, D. J., Schoemaker, H., & Perrault, G. (2000). Haloperidol-induced catalepsy is absent in dopamine D2, but maintained in dopamine D3 receptor knock-out mice. European journal of pharmacology, 391, 63-73.

Brischoux, F., Mainville, L., & Jones, B. E. (2008). Muscarinic-2 and orexin-2 receptors on GABAergic and other neurons in the rat mesopontine tegmentum and their potential role in sleep–wake state control. Journal of Comparative Neurology, 510, 607-630.

Broughton, R., Valley, V., Aguirre, M., Roberts, J., Suwalski, W., & Dunham, W. (1986). Excessive daytime sleepiness and the pathophysiology of narcolepsy-cataplexy: a laboratory perspective. Sleep, 9, 205-215.

Burgess, C. R., Tse, G., Gillis, L., & Peever, J. H. (2010). Dopaminergic regulation of sleep and cataplexy in a murine model of narcolepsy. Sleep, 33, 1295-1304.

Burgess, C. R., & Peever, J. H. (2013). A noradrenergic mechanism functions to couple motor behavior with arousal state. Current Biology, 23, 1719-1725.

Dauvilliers, Y., Arnulf, I., & Mignot, E. (2007). Narcolepsy with cataplexy. The Lancet, 369, 499-511.

Dauvilliers, Y., Siegel, J. M., Lopez, R., Torontali, Z. A., & Peever, J. H. (2014). Cataplexy—clinical aspects, pathophysiology and management strategy. Nature Reviews Neurology, 10, 386-395.

Fadel, J., & Deutch, A. Y. (2002). Anatomical substrates of orexin–dopamine interactions: lateral hypothalamic projections to the ventral tegmental area. Neuroscience, 111, 379-387.

Hasegawa, E., Yanagisawa, M., Sakurai, T., & Mieda, M. (2014). Orexin neurons suppress narcolepsy via 2 distinct efferent pathways. The Journal of clinical investigation, 124, 604-616.

Koike, B. D. V., Farias, K. S., Billwiller, F., Almeida-Filho, D., Libourel, P. A., Tiran-Cappello, A., ... & Queiroz, C. M. (2017). Electrophysiological evidence that the retrosplenial cortex displays a strong and specific activation phased with hippocampal theta during paradoxical (REM) sleep. Journal of Neuroscience, 37, 8003-8013.

Korotkova, T. M., Eriksson, K. S., Haas, H. L., & Brown, R. E. (2002). Selective excitation of GABAergic neurons in the substantia nigra of the rat by orexin/hypocretin in vitro. Regulatory peptides, 104, 83-89.

Korotkova, T. M., Sergeeva, O. A., Eriksson, K. S., Haas, H. L., & Brown, R. E. (2003). Excitation of ventral tegmental area dopaminergic and nondopaminergic neurons by orexins/hypocretins. Journal of Neuroscience, 23, 7-11.

Lambe, E. K., & Aghajanian, G. K. (2003). Hypocretin (orexin) induces calcium transients in single spines postsynaptic to identified thalamocortical boutons in prefrontal slice. Neuron, 40, 139-150.

Lambe, E. K., Olausson, P., Horst, N. K., Taylor, J. R., & Aghajanian, G. K. (2005). Hypocretin and nicotine excite the same thalamocortical synapses in prefrontal cortex: correlation with improved attention in rat. Journal of Neuroscience, 25, 5225-5229.

Liblau, R. S., Vassalli, A., Seifinejad, A., & Tafti, M. (2015). Hypocretin (orexin) biology and the pathophysiology of narcolepsy with cataplexy. The Lancet Neurology, 14, 318-328.

Lu, X. Y., Bagnol, D., Burke, S., Akil, H., & Watson, S. J. (2000). Differential distribution and regulation of OX1 and OX2 orexin/hypocretin receptor messenger RNA in the brain upon fasting. Hormones and behavior, 37, 335-344.

Mileykovskiy, B. Y., Kiyashchenko, L. I., & Siegel, J. M. (2005). Behavioral correlates of activity in identified hypocretin/orexin neurons. Neuron, 46, 787-798.

Nishino, S., Arrigoni, J., Valtier, D., Miller, J. D., Guilleminault, C., Dement, W. C., & Mignot, E. (1991). Dopamine D2 mechanisms in canine narcolepsy. Journal of Neuroscience, 11, 2666-2671.

Nishino, S., Ripley, B., Overeem, S., Lammers, G. J., & Mignot, E. (2000). Hypocretin (orexin) deficiency in human narcolepsy. The Lancet, 355, 39-40.

Oishi, Y., Williams, R. H., Agostinelli, L., Arrigoni, E., Fuller, P. M., Mochizuki, T., ... & Scammell, T. E. (2013). Role of the medial prefrontal cortex in cataplexy. Journal of Neuroscience, 33, 9743-9751.

Okura, M., Riehl, J., Mignot, E., & Nishino, S. (2000). Sulpiride, a D2/D3 blocker, reduces cataplexy but not REM sleep in canine narcolepsy. Neuropsychopharmacology, 23, 528-538.

Parmentier, R., Ohtsu, H., Djebbara-Hannas, Z., Valatx, J. L., Watanabe, T., & Lin, J. S. (2002). Anatomical, physiological, and pharmacological characteristics of histidine decarboxylase knock-

out mice: evidence for the role of brain histamine in behavioral and sleep–wake control. Journal of Neuroscience, 22, 7695-7711.

Peyron, C., Tighe, D. K., Van Den Pol, A. N., De Lecea, L., Heller, H. C., Sutcliffe, J. G., & Kilduff, T. S. (1998). Neurons containing hypocretin (orexin) project to multiple neuronal systems. Journal of Neuroscience, 18, 9996-10015.

Peyron, C., Faraco, J., Rogers, W., Ripley, B., Overeem, S., Charnay, Y., ... & Mignot, E. (2000). A mutation in a case of early onset narcolepsy and a generalized absence of hypocretin peptides in human narcoleptic brains. Nature medicine, 6, 991-997.

Reid, M. S., Tafti, M., Nishino, S., Sampathkumaran, R., Siegel, J. M., & Mignot, E. (1996). Local administration of dopaminergic drugs into the ventral tegmental area modulates cataplexy in the narcoleptic canine. Brain research, 733, 83-100.

Scammell, T. E. (2015). Narcolepsy. New England Journal of Medicine, 373, 2654-2662.

Schoch, S. F., Werth, E., Poryazova, R., Scammell, T. E., Baumann, C. R., & Imbach, L. L. (2017). Dysregulation of sleep behavioral states in narcolepsy. Sleep, 40, zsx170.

Seifinejad, A., Li, S., Possovre, M. L., Vassalli, A., & Tafti, M. (2020). Hypocretinergic interactions with the serotonergic system regulate REM sleep and cataplexy. Nature communications, 11, 1-12.

Seifinejad, A., Vassalli, A., & Tafti, M. (2021). Neurobiology of cataplexy. Sleep medicine reviews, 60, 101546.

Snow, M. B., Fraigne, J. J., Thibault-Messier, G., Chuen, V. L., Thomasian, A., Horner, R. L., & Peever, J. (2017). GABA cells in the central nucleus of the amygdala promote cataplexy. Journal of Neuroscience, 37, 4007-4022.

Vassalli, A., Dellepiane, J. M., Emmenegger, Y., Jimenez, S., Vandi, S., Plazzi, G., ... & Tafti, M. (2013). Electroencephalogram paroxysmal theta characterizes cataplexy in mice and children. Brain, 136, 1592-1608.

Wisor, J. P., Nishino, S., Sora, I., Uhl, G. H., Mignot, E., & Edgar, D. M. (2001). Dopaminergic role in stimulant-induced wakefulness. Journal of Neuroscience, 21, 1787-1794.

Zhou, Q. Y., & Palmiter, R. D. (1995). Dopamine-deficient mice are severely hypoactive, adipsic, and aphagic. Cell, 83, 1197-1209.

Chapter 4. Physiological validation of the Orexin Receptor 2 CKO mouse model

Abstract

Orexin deficiency causes narcolepsy. The causal link with the disease is poorly understood, as is the physiological role of these neuropeptides, and, especially, the differential role of the two orexin receptors. To better dissect the relative contributions of Ox1R and Ox2R in different circuits and brain areas, their coding genes were engineered to create for each receptor a Cre-dependent conditional KO (OrxR-flox) allele, where GFP can replace OrxR upon crossing with a proper CRE mouse line (Ox2R-Δ). To test the effective functional deletion of Ox2R in Ox2R-Δ mice and to assess if the Ox2R-flox mice had functionally equivalent Ox2R as ctrl mice, I assessed the responses to Ox2R agonists of the classical Ox2R-expressing neuronal type: the histaminergic neurons of the ventral tuberomammillary nucleus (vTMN) of the hypothalamus. Bath application of Ox2R agonists triggers a long train of approximately 2 Hz APs in the neurons from the C57BL6/J (ctrl) and Ox2R-floxed mice but not in neurons from the Ox2R-Δ mice. Conversely, TCS-OX2-029 10 μM, a specific Ox2R antagonist, blocked the effects of either OrxB 100 nM or OrxB-AL 200 nM, in 80-100% of the ctrl or Ox2R-flox cells, showing that the excitatory effect is specifically

Ox2R-dependent. Overall, the data confirm the functional equivalence of Ox2Rs in ctrl and Ox2R-flox mice, as well as its functional ablation in Ox2R-Δ mice.

Introduction

Deficiency in OrxA and OrxB (Orx) causes narcolepsy. Neither the mechanisms by which loss of these neuropeptides causes the wide symptomatic range, nor Orx's roles in normal behaviour, are fully solved. The narcolepsy dog model, that harbours mutations in Ox2R (Lin et al. 1999), led to discover the Orx role in wake/sleep control, but whether similar mutations in mice or humans cause narcolepsy is unclear (Liblau et al. 2015; Kornum et al. 2017; Miyagawa & Tokunaga, 2019). In fact, Ox2R genetic lesions cause severe cataplexy in dogs, but a milder phenotype in mice. Using novel EEG and cataplexy-defining criteria, OrxKO mice were revisited and priorly unrecognized cataplexy traits in mice and narcoleptic children were discovered (Vassalli et al. 2013). To functionally dissect the Orx circuits into simpler components, the 2 genes for the Orx receptors, Ox1R and 2, were engineered by our collaborator Anne Vassalli (University of Lausanne) in embryonic stem cells to create for each receptor a Cre-dependent conditional KO (CKO) (OrxR-flox), and a global KO and GFP-reporter (OrxRKO-Gfp or Ox2R-Δ)

mouse line, where GFP replaces OrxR (Vassalli et al. 2015; Li et al. 2018).

To generate the Ox2R-flox allele, a loxP site was targeted in Ox2R exon 1 between the transcription start site and the START codon, and a second loxP site followed by a promoter-less GFP open reading frame cassette in the first intron (Fig. 4.1). Ox1R and 2 floxed alleles were designed such that CRE/lox recombination replaces the coding region of the Orx receptor by the one of GFP and terminates downstream transcription. This marks with GFP the cells which would physiologically express the receptor but no longer have its sequence in the genome, as they successfully underwent genomic recombination. This CKO mouse models were further validated by using the 1-cell embryo expressed EIIa-Cre transgene to generate whole-body KO lines for each gene (Ox1R and 2 delta alleles), intercrossing the 2 lines and showing that the compound homozygous $Ox1R^{del/del}$; $Ox2R^{del/del}$ mice manifest cataplexies with similar characteristics and frequency as $Orx^{KO/KO}$ mice.

Figure 4.1. Schematic representation of Ox2R targeting strategy used to generate the conditional KO (“floxed”) alleles, and, after Neo excision and Cre-mediated recombination, the Δ-GFP KO alleles.

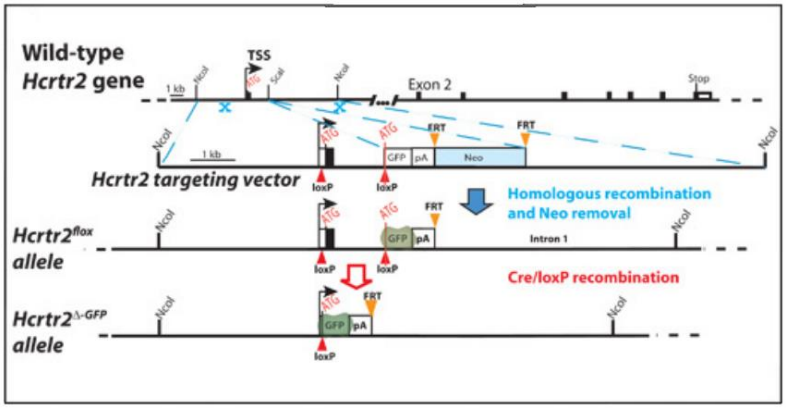

To test the effective functional deletion of Ox2R in Ox2R-Δ mice and to assess if the Ox2R-flox mice had functionally equivalent Ox2R as ctrl mice, I patch-clamped histaminergic neurons in the ventral tuberomammillary nucleus (vTMN) of the hypothalamus and verified their response to Ox2R agonists, in presence or absence of its specific blocker, TCS-OX2-029. We chose histaminergic vTMN neurons because they are the classical neuronal type with selective Ox2R expression (Marcus et al. 2001; Eriksson et al. 2001; Yamanaka et al. 2002; Schöne et al. 2014; Ikeno & Yan, 2018) and their specific responsiveness to Ox2R agonists has been used in literature to verify the effective knockout of the receptor (Willie et al. 2003).

Materials and Methods

Brain slices

A total of 16 young adult C57BL6/J mice (Charles River, USA), 13 Ox2R-floxed mice, and 17 Ox2R-Δ mice (University of Lausanne) of both sexes (7 males and 9 females, 6+7, and 9+8, respectively), ranging from P21 to P49, were kept in pathogen-free conditions, with free access to food and water, and a 12 h light-dark cycle. The described procedures followed the Italian law (2014/26, implementing the 2010/63/UE) and were approved by the local Ethical Committee and the Italian Ministry of Health (68/2021-PR).

After a deep anaesthesia with 5% isoflurane, mice were decapitated and the brains were rapidly extracted and placed in ice-cold solution, containing (mM): 87 NaCl, 21 $NaHCO_3$, 1.25 NaH_2PO_4, 7 $MgCl_2$, 0.5 $CaCl_2$, 2.5 KCl, 25 D-glucose, 75 sucrose, 0.8 ascorbic acid, and aerated with 95% O_2 and 5% CO_2 (pH 7.4). Coronal slices (300 µm thick) from the tuberomammillary nucleus (TMN) were cut between -2.18 mm and -2.92 mm from bregma (Franklin & Paxinos, 2008), with a VT1000S vibratome (Leica Microsystems) and then maintained at 30°C in the above solution for at least 1h before being transferred to the recording chamber.

Whole-cell recordings

Cells were examined with an Eclipse E600FN microscope, as reported (Aracri et al. 2017). Stimulation and recording were carried out with a Multiclamp 700A (Molecular Devices), at 32-34°C. Micropipettes (2-4 MΩ) were pulled from borosilicate capillaries (Science Products GmbH, GE) with a P-97 Flaming/Brown Micropipette Puller (Sutter Instruments Co., UK). The cell capacitance and series resistance were always compensated (up to 75%). Series resistance was generally below 10 MΩ. Neurons were both voltage- and current-clamped in whole-cell configuration and the input resistance was usually between 30 and 70 MΩ. Slices were perfused at 1.8-2 mL/min with artificial cerebrospinal fluid (ACSF) containing (mM): 129 NaCl, 21 $NaHCO_3$, 1.6 $CaCl_2$, 3 KCl, 1.25 NaH_2PO_4, 1.8 $MgSO_4$, 10 D-glucose, aerated with 95% O_2 and 5% CO_2 (pH 7.4). Pipettes contained (mM): 140 K-gluconate, 5 KCl, 1 $MgCl_2$, 0.1 BAPTA, 2 MgATP, 0.3 NaGTP, 10 HEPES (pH 7.25). In some experiments, 0.15% biocytin was added for post-recording staining and morphological reconstruction (Eriksson et al. 2001).

Traces were low-pass Bessel filtered at 2 kHz and digitized at 10 kHz, with pClamp9/Digidata 1322A (Molecular Devices). The resting membrane potential (V_{rest}) was measured in open circuit mode, soon after obtaining the whole-cell configuration. No correction was applied for liquid

junction potentials. Drugs were perfused in the bath and their effects on cell firing were measured for 2 min after reaching the maximal effect, which – in the case of Ox2R agonists – usually occurred at least 30 seconds after the drug was removed (Yamanaka et al. 2002; Eriksson et al. 2001). Only one neuron was sampled in each slice, to avoid uncontrolled long-term effects of neuromodulators (e.g. on receptor desensitization).

Drugs and solutions

Orexin B (OrxB), [Ala^{11},D-Leu^{15}]-OrexinB (OrxB-AL) and TCS-Ox2-29 (TCS) were purchased from Tocris Bioscience (Bristol, UK). They were dissolved in distilled water and stored at -20°C.

Analysis of patch-clamp data

Data were analysed off-line by using Clampfit 9.2 (Molecular Devices), and OriginPro 2019 (OriginLab Corporation, Northampton, MA, USA). The action potential (AP) features were analysed during the first step of current injection that was able to trigger four APs (usually 150 pA). AP amplitude, width, rise and decay slope, threshold, and triggering slope were measured on the first AP of the induced train. Spike width was calculated at half-amplitude, spike amplitude was computed as the difference between the AP threshold and the peak. Adaptation was measured as the ratio between the

fourth and the first spike interval. Spike intervals were measured between consecutive peaks. After hyperpolarization (AHP) was measured as the difference between the AP threshold and the most negative V_m reached on repolarization. Finally, the triggering depolarization slope was the difference between the most negative V_m reached on repolarization and the following AP threshold, divided by the relative time. The time constants of membrane charging, and discharging were estimated by mono-exponential fit to the passive response to -100 pA injection, whereas the time constant of the I_h-related sag was analogously fitted to the reduction in steady-state current upon -50 pA injection, from the negative peak to the end of the 0.5 s current pulse.

Statistics

The results from multiple experiments are given as mean values ± SEM. The number of experiments (N) refers to the number of tested neurons (in different brain slices). Data normality and variance homogeneity were respectively verified with the Q-Q plot inspection and the F test. Statistical comparison between genotypes was carried out with one-way ANOVA test and Tukey Test for multiple mean comparison, at the indicated level of significance (p).

Results

Putative histaminergic neurons in the hypothalamic TMN were identified based on their typical electrophysiological properties (Fig. 4.2), such as the approximately 2 Hz spontaneous firing, the late-spiking profile (Fig. 4.2 A), the I_h-related sag upon hyperpolarizing pulses, the resting potential around -50 mV (Fig. 4.2 D) and the cell capacitance around 20 pF (Fig.4.2 C; Haas & Reiner, 1988; Michael et al. 2020). The passive membrane properties, including τ membrane charging (Fig. 4.2 E), τ membrane discharging and τ sag (Fig. 4.2 F), were similar across genotypes.

Figure 4.2. Identification of putative histaminergic neurons in the hypothalamic TMN. (A) Putative histaminergic neurons were characterized by testing the firing response to consecutive depolarizing current steps, lasting 500 ms. The responses to the -100 pA and the 100 pA steps for a representative neuron show the classical hyperpolarization-triggered sag, attributed to Ih, and the low-frequency late firing. (B) Relation between injected current and firing frequency for putative histaminergic neurons (25, 16, 20 cells for Ctrl, Ox2R-flox and Ox2R-Δ, respectively). Data points are average firing frequencies calculated from a coherent ensemble of neurons and plotted as a function of injected current. Passive membrane properties are coherent with those reported by Haas and Reiner, J Physiol, 1988 (C) Cell capacitance (D) V_{rest} (E) $\tau_{membrane\ charging}$ (F) τ_{sag} as a quantifying parameter for the I_h amplitude (WT: 24, Ox2R-flox: 18, Ox2R-Δ: 20 cells).

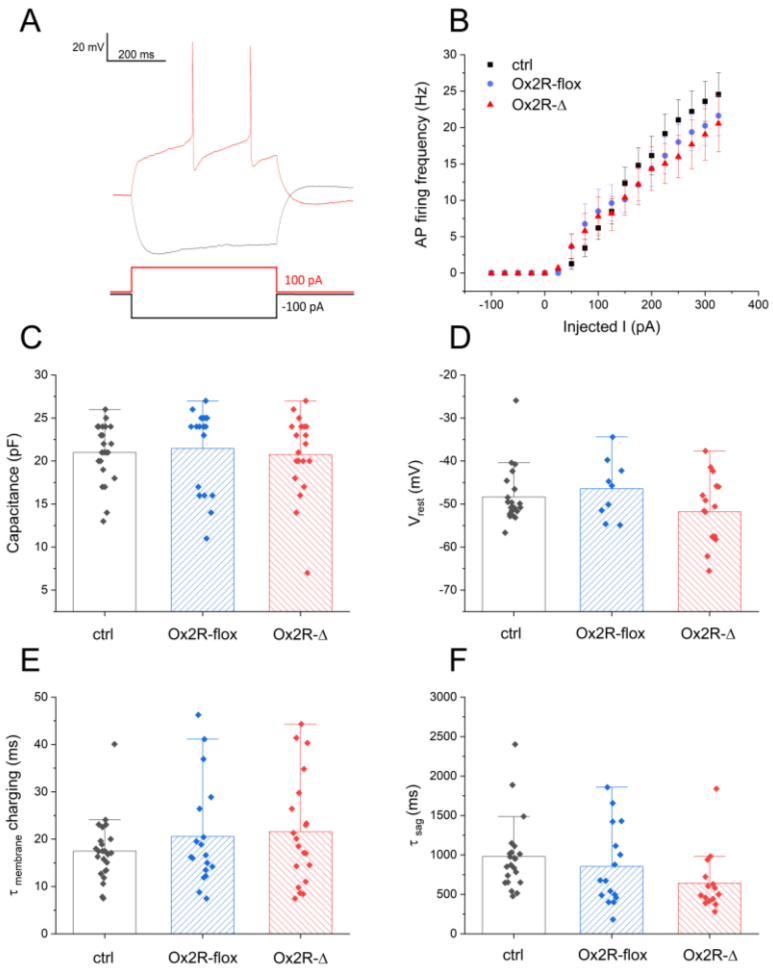

In a fraction of experiments, biocytin filling allowed the morphological reconstruction of patched cells, which confirmed the large diameter (20-30 µm) and multipolar shape of histaminergic TMN neurons (Fig 4.3; Eriksson et al. 2001).

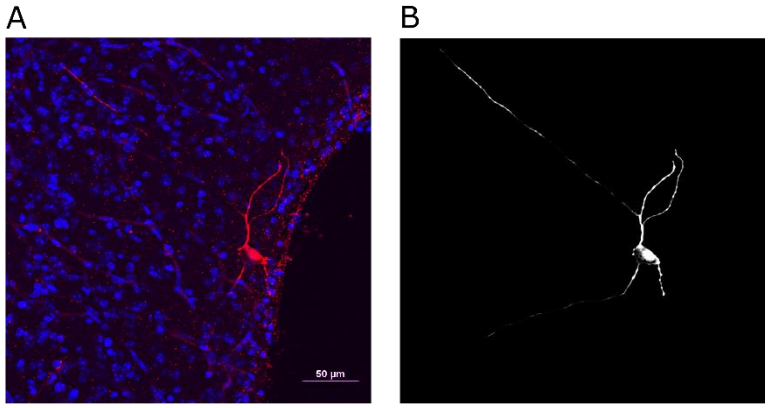

Figure 4.3. Morphology of putative histaminergic neurons in the hypothalamic ventral TMN. (A) Maximal intensity projection of a 40x Z-stack of a 300 µM slice processed for IHF against biocytin (Rhodamine RedX streptavidin), injected during the recording, and DAPI. (B) Projection of the 3D reconstruction of the putative histaminergic neuron. Scale bar 50 µM.

On the other hand, some action potential (AP) features were different between Ctrl and Ox2R-Δ cells (Fig 4.4): AP amplitude was reduced and more variable in Ox2R-Δ (p-value = 0.01097; Fig. 4.4 A), AP half-width was increased and was more variable (p-value = 0.01294; Fig. 4.4 C), both AP rise slope (p-value = 0.01026; Fig. 4.4 E) and AP decay slope decreased (p-value = 0.0431; Fig. 4.4 F). These small changes lead to a slightly slower AP dynamics and suggest a partly reduced maturation of histaminergic cells in Ox2R-Δ mice.

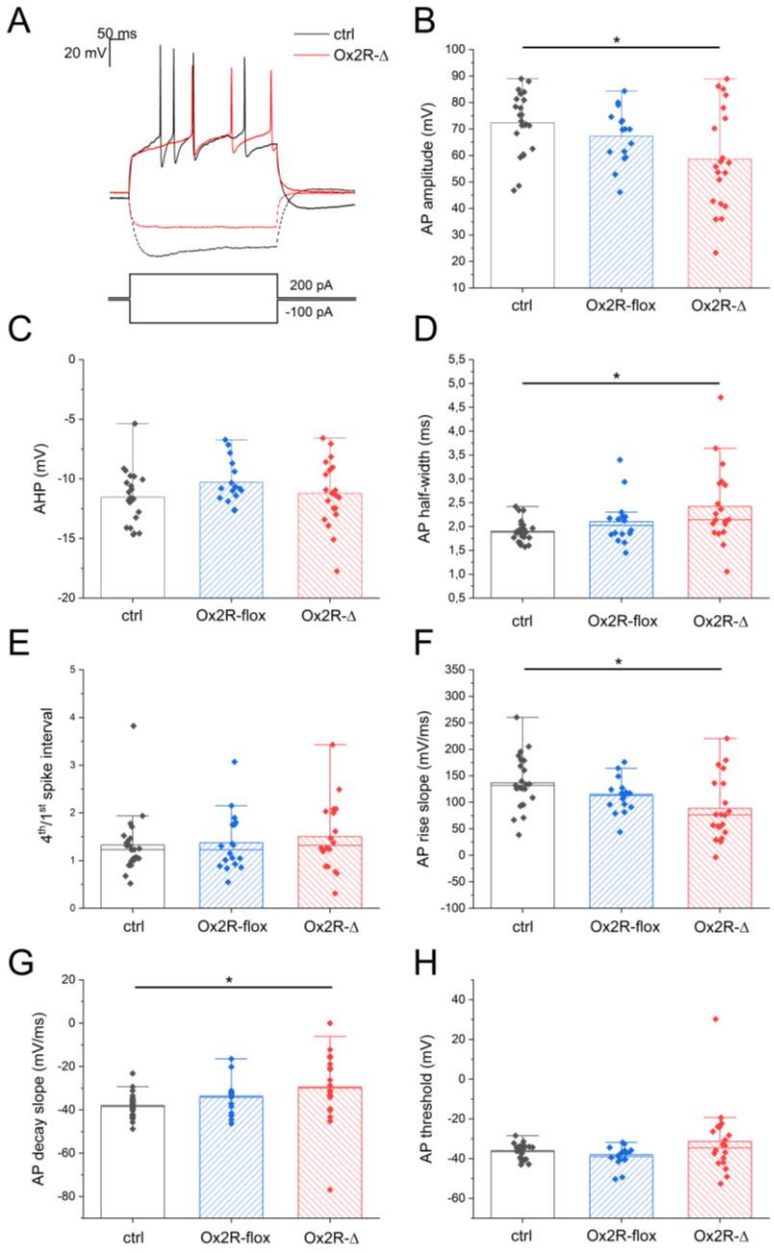
A
50 ms
20 mV
ctrl
Ox2R-Δ
200 pA
-100 pA
B
AP amplitude (mV)
C
AHP (mV)
D
AP half-width (ms)
E
4th/1st spike interval
F
AP rise slope (mV/ms)
G
AP decay slope (mV/ms)
H
AP threshold (mV)
ctrl
Ox2R-flox
Ox2R-Δ
*

Figure 4.4. Electrophysiological features of putative histaminergic neurons in the hypothalamic TMN. AP features of Ctrl and Ox2R-floxed neurons are both in line with classical evidence, but Ox2R-Δ cells display a reduced mean and more variable AP amplitude (B, p-value = 0.01097), an increased mean and more variable AP half-width (D, p-value = 0.01294), a reduced AP rise slope (F, p-value = 0.01026) and an increased AP decay slope (G, p-value = 0.0431). These small changes lead to a slightly slower AP dynamics (A) and suggest a partly reduced excitability of histaminergic cells in Ox2R-Δ mice, that could be related to a possible role of Ox2R in the developmental specification of the histaminergic neuronal phenotype. (C) after-hyperpolarization (E) $4^{th}/1^{st}$ spike interval, a measure of AP frequency adaptation (H) AP threshold (WT: 23, Ox2R-flox: 16, Ox2R-Δ: 20 cells).

Spontaneous voltage oscillations were recorded from putative histaminergic neurons in the hypothalamic TMN, held at around −50 mV in current-clamp (Fig. 4.5). Two-minutes long OrxB-AL 200 nM bath application triggered a long train of approximately 2 Hz APs in 88% of the neurons from the C57BL6/J and in 100% from the Ox2R-flox mice but was not effective in 91% of the neurons from the Ox2R-Δ mice (total cell number: 17, 3, 11, respectively). Similar results were obtained with OrxB 100 nM (total cell number: 19, 4, 10). Moreover, the specific Ox2R antagonist TCS-OX2-029 (10 μM) blocked the effect of either OrxB 100 nM or OrxB-AL 200 nM, in 80-100% of the ctrl or Ox2R-floxed cells (total cell number: 8, 5, 5; and 5, 6, 5), confirming that the responses are Ox2R-specific. Thus, it can be concluded that the Ox2Rs are functionally active in Ox2R-flox mice, comparably to ctrls, and they are inactive in Ox2R-Δ mice.

Figure 4.5. Ox2Rs are functionally inactive in Ox2R-Δ mice. (A) Spontaneous voltage oscillations were recorded from putative histaminergic neurons in the hypothalamic TMN, held at around −50 mV in current-clamp. Voltage traces represent 5 minutes continuous recording, before, during (red line), and after OrxB-AL 200 nM application. OrxB-AL triggered a long train of approximately 2 Hz APs in neurons from both the C57BL6/J and the Ox2R-floxed mouse but was not able to do it in the neuron from the Ox2R-Δ mouse. (B) Percentage of neurons responding to different drugs for each genotype. Treatments: OrxB 100 nM, OrxB-AL 200 nM, TCS OX2 029

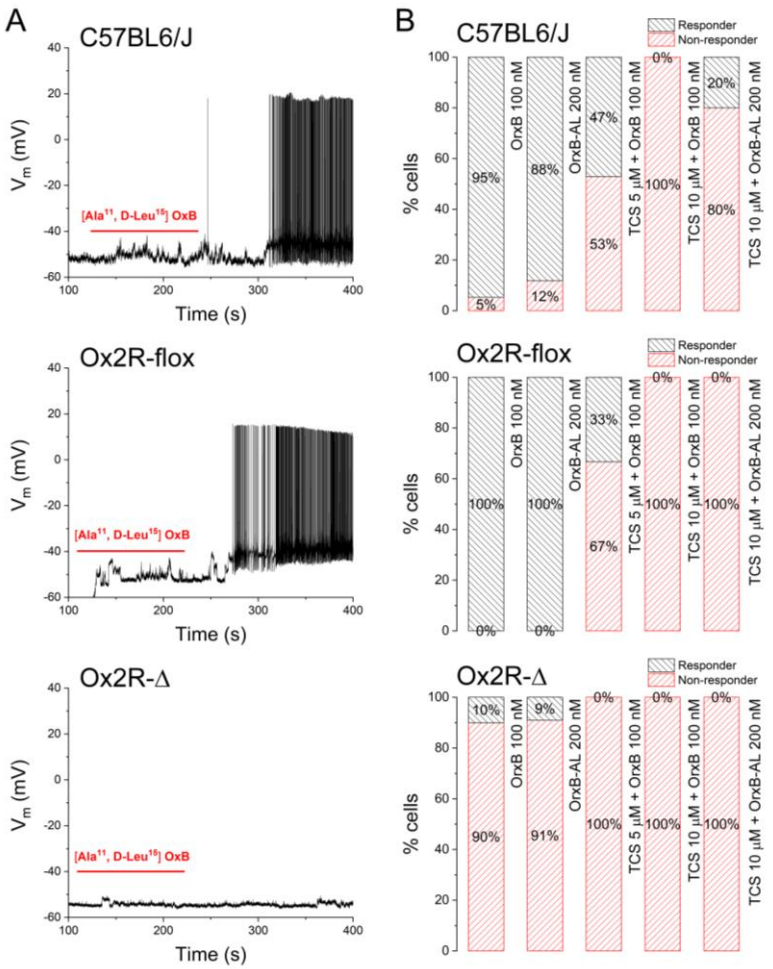

Figure 4.5. *(follows)* 5 μM + OrxB 100 nM, TCS OX2 029 10 μM + OrxB 100 nM, TCS OX2 029 10 μM + OrxB-AL 200 nM. Total number of neurons, respectively: C57BL6/J (Ctrl) 19, 17, 17, 8, 5; Ox2R-floxed 4, 3, 6, 5, 6; Ox2R-Δ 10, 11, 7, 5, 5.

Discussion

The Cre-lox OxRs allele engineering approach allowed the creation of a very flexible conditional mouse model, which may potentially allow to evaluate the role of OxRs in any cerebral subcircuit, by crossing with a proper CRE mouse line. Thanks to these mouse models, in fact, a fundamental role for Ox1R has been established in the noradrenergic circuit as related to alertness, motivation and θ/γ rhythmogenesis regulation (Li et al. 2018), and more investigations are ongoing on the role of Ox2R in the dopaminergic circuit (Chapter 5 & 6).

Overall, the data above reported demonstrate that the Ox2R-flox conditional KO allele remains functional, but that CRE recombination creates a null phenotype (Ox2R-Δ). They highlight, as well, some small changes in the active properties of histaminergic neurons of the vTMN in the Ox2R-Δ mouse. These features lead to slightly slower AP dynamics, suggesting a partly reduced maturation of histaminergic cells in Ox2R-Δ mice, that may be related to a possible role of Ox2R in the developmental specification of the histaminergic neuronal phenotype. Such subtle changes may, in fact,

indicate a not fully mature phenotype since it's known that AP amplitude increases and AP duration decreases along the neuronal development and differentiation in many cell types, from Cajal-Retzius cortical layer I neurons (Zhou & Hablitz, 1996) to CA1 pyramidal neurons (Spigelman et al. 1992, Sánchez-Aguilera et al. 2020). Moreover, a study on narcoleptic human tissue showed an increased number of histaminergic neurons, which was not present in dog and mouse models of narcolepsy, suggesting a possible implication of the histaminergic system in the human pathogenesis of the disease and/or of the orexinergic system in the histaminergic one development, even if with enigmatic mechanisms (John et al. 2013). However, the role of Ox2R in neuronal maturation still needs further investigation, and, if confirmed, this would be, to our best knowledge, its first evidence.

References

Aracri, P., Meneghini, S., Coatti, A., Amadeo, A., & Becchetti, A. (2017). α4β2∗ nicotinic receptors stimulate GABA release onto fast-spiking cells in layer V of mouse prefrontal (Fr2) cortex. Neuroscience, 340, 48-61.

Eriksson, K. S., Sergeeva, O., Brown, R. E., & Haas, H. L. (2001). Orexin/hypocretin excites the histaminergic neurons of the tuberomammillary nucleus. Journal of Neuroscience, 21, 9273-9279.

Paxinos, G., & Franklin, K. B. (2008). Paxinos and Franklin's the mouse brain in stereotaxic coordinates. Academic press.

Haas, H. L., & Reiner, P. B. (1988). Membrane properties of histaminergic tuberomammillary neurones of the rat hypothalamus in vitro. The Journal of Physiology, 399, 633-646.

Ikeno, T., & Yan, L. (2018). A comparison of the orexin receptor distribution in the brain between diurnal Nile grass rats (Arvicanthis niloticus) and nocturnal mice (Mus musculus). Brain research, 1690, 89-95.

John, J., Thannickal, T. C., McGregor, R., Ramanathan, L., Ohtsu, H., Nishino, S., ... & Siegel, J. M. (2013). Greatly increased numbers of histamine cells in human narcolepsy with cataplexy. Annals of neurology, 74, 786-793.

Kornum, B. R., Knudsen, S., Ollila, H. M., Pizza, F., Jennum, P. J., Dauvilliers, Y., & Overeem, S. (2017). Narcolepsy. Nature reviews Disease primers, 3, 1-19.

Li, S., Franken, P., & Vassalli, A. (2018). Bidirectional and context-dependent changes in theta and gamma oscillatory brain activity in noradrenergic cell-specific Hypocretin/Orexin receptor 1-KO mice. Scientific reports, 8, 1-24.

Lin, L., Faraco, J., Li, R., Kadotani, H., Rogers, W., Lin, X., ... & Mignot, E. (1999). The sleep disorder canine narcolepsy is caused by a mutation in the hypocretin (orexin) receptor 2 gene. Cell, 98, 365-376.

Liblau, R. S., Vassalli, A., Seifinejad, A., & Tafti, M. (2015). Hypocretin (orexin) biology and the pathophysiology of narcolepsy with cataplexy. The Lancet Neurology, 14, 318-328.

Marcus, J. N., Aschkenasi, C. J., Lee, C. E., Chemelli, R. M., Saper, C. B., Yanagisawa, M., & Elmquist, J. K. (2001). Differential expression of orexin receptors 1 and 2 in the rat brain. Journal of Comparative Neurology, 435, 6-25.

Michael, N. J., Zigman, J. M., Williams, K. W., & Elmquist, J. K. (2020). Electrophysiological Properties of Genetically Identified Histaminergic Neurons. Neuroscience, 444, 183-195.

Miyagawa, T., & Tokunaga, K. (2019). Genetics of narcolepsy. Human genome variation, 6, 1-8.

Sánchez-Aguilera, A., Monedero, G., Colino, A., & Vicente-Torres, M. Á. (2020). Development of action potential waveform in hippocampal CA1 pyramidal neurons. Neuroscience, 442, 151-167.

Schöne, C., Apergis-Schoute, J., Sakurai, T., Adamantidis, A., & Burdakov, D. (2014). Coreleased orexin and glutamate evoke nonredundant spike outputs and computations in histamine neurons. Cell reports, 7, 697-704.

Spigelman, I. G. O. R., Zhang, L. I. A. N. G., & Carlen, P. L. (1992). Patch-clamp study of postnatal development of CA1 neurons in rat hippocampal slices: membrane excitability and K+ currents. Journal of Neurophysiology, 68, 55-69.

Vassalli, A., Dellepiane, J. M., Emmenegger, Y., Jimenez, S., Vandi, S., Plazzi, G., ... & Tafti, M. (2013). Electroencephalogram paroxysmal theta characterizes cataplexy in mice and children. Brain, 136, 1592-1608.

Vassalli, A., Li, S., & Tafti, M. (2015). Comment on “Antibodies to influenza nucleoprotein cross-react with human hypocretin receptor 2”. Science translational medicine, 7, 314le2-314le2.

Willie, J. T., Chemelli, R. M., Sinton, C. M., Tokita, S., Williams, S. C., Kisanuki, Y. Y., ... & Yanagisawa, M. (2003). Distinct narcolepsy syndromes in Orexin receptor-2 and Orexin null mice: molecular genetic dissection of Non-REM and REM sleep regulatory processes. Neuron, 38, 715-730.

Yamanaka, A., Tsujino, N., Funahashi, H., Honda, K., Guan, J. L., Wang, Q. P., ... & Sakurai, T. (2002). Orexins activate histaminergic neurons via the orexin 2 receptor. Biochemical and biophysical research communications, 290, 1237-1245.

Zhou, F. M., & Hablitz, J. J. (1996). Postnatal development of membrane properties of layer I neurons in rat neocortex. Journal of Neuroscience, 16, 1131-1139.

Chapter 5. Orexinergic modulation of the microcircuit activity in the prefrontal cortex: a possible source of θ rhythmogenesis

Abstract

Hypersynchronous paroxysmal θ activities are highly enriched during cataplexy in orexin knockout mice and narcoleptic children, and they are independent of hippocampal θ, rather involving the frontal cortex. However, little is known about how Orxs regulate the activity of associative cortices. We studied the Orx modulation of pyramidal and interneuronal microcircuits of Fr2 and medial PFC. OrxA stimulated EPSCs on layer V pyramidal neurons. The effect is mainly mediated by Ox1Rs, and depends on a presynaptic mechanism involving Ca_V channel-dependent and independent mechanisms. The stimulatory effect of OrxA is observed in both FVB and C57BL6/J. This allows to use our murine strains conditionally expressing Ox1R and Ox2R in C57BL6/J background, to assess the relative contribution of either. OrxB and OrxB-AL do not seem to be significantly involved in the excitatory transmission regulation on Pys, suggesting a secondary role for Ox2Rs. Immunocytochemistry showed a diffuse Ox2R distribution on both cell bodies and neuropil, with no clear PFC subregion or layer-specific staining. Nonetheless, colocalization analysis

showed i) denser orexinergic innervation of SOM^+ GABAergic interneurons, as compared to PV^+ cells; ii) higher expression of Ox2R on SOM^+ neurons. These interneurons have been shown to contribute to the generation of θ band rhythm in the neocortex and hippocampus. Hence, these results lead us to hypothesize that orexins could regulate θ rhytmogenesis in the PFC by a dual mechanism: stimulation of pyramidal neurons (mainly through Ox1R), and SOM^+ cells (mainly through Ox2R). Orx deficiency may also be linked to the abnormal θ activity observed in narcoleptic patients, especially related to cataplexy.

Introduction

During Orx-mediated awakening, the oscillatory activity of cortical and subcortical networks undergoes dramatic changes as global brain state switches from SWS to wakefulness, and the EEG spectral profile exhibits major changes in dominant frequencies. The underlying neuronal synchronization processes constitute a critical system-level mechanism which likely coordinates neural processing, and facilitates inter-area information transfer (Sakurai, 2014; Soya & Sakurai, 2020).

The molecular and electrophysiological mechanisms by which neuromodulators mediate these effects are poorly defined, especially in associative cortices. Both intra and

extracortical mechanisms contribute to neocortex oscillations (Wang, 2010), whose origin and relationship with attentive and exploratory states is currently not fully resolved. The θ rhythm arises from a combination of multiple intrinsic θ oscillators and their interaction with hippocampal networks. Thus, both intra and extracortical mechanisms contribute to the observed oscillations (Wang, 2010). One of these oscillators is thought to be the mPFC of rodents and primates, including humans (Cohen, 2014). Consistently, as discussed earlier, the hypersynchronous paroxysmal θ waves observed during cataplexy in hypocretin/orexin knockout mice and narcoleptic children are independent of hippocampal θ and involve the frontal cortex (Vassalli et al. 2013).

The θ rhythm is generally attributed to the activity of pyramidal (Py) cells, particularly of deep layers, whose sub-threshold and bursting activity occur at frequencies that tend to cluster around θ (Wang, 2010). These waves can also be generated in cortical slices in the absence of subcortical input (Silva et al. 1991; Castro-Alamancos et al. 2007). Nonetheless, the resonant properties of Py cells make them maximally sensitive to θ frequency drive from subcortical nuclei (Wang, 2010), including GABAergic populations of the nucleus basalis in basal forebrain (BF; Alonso et al. 1996). Importantly, from the present perspective, SOM^+ interneurons have also been recently implicated in the

generation of θ-band rhythm activity in neocortex pyramidal neurons (Hilscher et al. 2017) as well as in the hippocampus (Amilhon, et al. 2015; Mikulovic, 2016; Mikulovic, et al. 2018). Moreover, chemogenetic activation of SOM^+ interneurons increases EEG θ activity in the premotor M2 region, overlapping with Fr2 (Funk, et al. 2017).

In summary, orexins could affect neocortex rhythms in two ways:

1) By exciting the wake-promoting nuclei of brainstem, hypothalamus, and BF (Peyron et al. 1998; Sutcliffe & de Lecea, 2002), which in turn innervate the neocortex. They also excite the unspecific thalamocortical neurons of the midline-intralaminar thalamic nuclei (Peyron et al. 1998; Bayer et al. 2002), which project to the PFC, where they form the final synapse of the ascending arousal pathway.

2) By directly activating neuronal populations in PFC (Peyron et al. 1998; Fadel & Deutch 2002). Several lines of evidence showed that Orx exerts excitatory effects in the medial PFC (mPFC; Lambe & Aghajanian, 2003: Lambe et al. 2005; Li et al. 2010; He et al. 2015), and primary sensory cortex (Wenger Combremont et al. 2016). Moreover, Orx stimulates glutamate release in the PFC Fr2, thereby indirectly stimulating Fast-Spiking (FS) interneurons (Aracri et al.

2015), suggesting a complex contribution of Orxs to local rhythmogenesis.

Here, I investigated the Orx modulation of pyramidal and interneuronal microcircuits in PFC layer V, to elucidate the possible intrinsic Orx-dependent mechanisms for θ regulation in the PFC circuits.

Materials and Methods

For the experiments carried out at the University of Milano-Bicocca, a total of 24 adult FVB mice (Charles River, USA), 7 C57BL6/J mice (Charles River, USA) and 6 Ox2R-Δ mice (University of Lausanne) of both sexes (10 males and 14 females, 2 and 5, and 3 and 3, respectively), ranging from P30 to P69, were kept in pathogen-free conditions, with free access to food and water, and a 12 h light-dark cycle.

Patch-clamp recording and data analysis

Most procedures were carried out as illustrated in Chapter 3. For EPSC recording, cells were voltage-clamped at -68 mV. ACSF-high K^+ recipe was the following (mM): 116 NaCl, 21 $NaHCO_3$, 1.6 $CaCl_2$, 20 KCl, 1.25 NaH_2PO_4, 1.8 $MgSO_4$, 10 D-glucose, aerated with 95% O_2 and 5% CO_2 (pH 7.4). Analysis of synaptic events was carried out with Mini Analysis (Synaptosoft Inc.). Events were analyzed one by one within segments of continuous recording (2 min), in the different experimental conditions. The analyzed time segments

usually included hundreds (often thousands) of synaptic events. The baseline noise was generally < 5 pA (peak-to-peak). The detection threshold was usually set at ~5 pA, which is the minimal expected amplitude of synaptic events.

Drugs and solutions were the same as in Chapter 4.

Tissue preparation for immunohistochemistry

Eight P105 mice (4 Ox2R-flox and Ox2R-Δ, 2 males and 2 females of each genotype) were anesthetized with isoflurane and intraperitoneal 4% chloral hydrate (2 ml/100 g, for adult mice), and sacrificed by intracardiac perfusion as described (Aracri et al. 2013). The brains were extracted and immersed in 4% paraformaldehyde in phosphate buffer (PB), for 24-48 h at 4°C. Serial coronal brain sections (50 µm thick) were cut with a Leica VT1000S vibratome.

Primary antibodies

Anti-OrxA: polyclonal antibody, made in sheep, against the synthetic peptide corresponding to amino acids P(2) LPD CCRQKTCSC(14) of human OrxA conjugated to KLH (Thermo-Fisher Scientific; catalogue n° PA1-85744; diluted 1: 300). Anti-PV (parvalbumin): monoclonal, made in mouse, against the recombinant protein corresponding to AA 1 to 110 from rat PV (Synaptic Systems; catalogue n° 195 011; diluted 1:250). Anti-SOM (somatostatin): monoclonal, made in rat myeloma cell line against human SOM conjugated to

thyroglobulin (BioRad; catalogue n° 8330-0009; diluted 1:250). Anti-Ox2R (orexin receptor 2): polyclonal, made in rabbit against the synthetic peptide (C)DRLARGRTSTESRKS, corresponding to amino acid residues 391-405 of rat OX2R (Alomone Labs; catalogue n° AOR-002; diluted 1:100). Anti-GFP (green fluorescent protein): polyclonal, made in chicken against recombinant GFP expressed in *Escherichia coli* (Alomone Labs; catalogue n° GFP-1020; diluted 1:500). The reaction specificity for the anti-Ox2R Ab was assessed by negative controls, such as IHF on tissue from Ox2R-Δ mice and IHF on tissue from Ox2R-flox mice with the specific Ab blocking peptide (Alomone Labs; catalogue n° BLP-OR002; diluted 1:50).

Immunofluorescence histochemistry

Sections were permeabilized and blocked for 45' in the following solution: 2% BSA (bovine serum albumin, Jackson Immunoresearch), 5% normal donkey serum (Jackson Immunoresearch), 0.1% Tween-20 in TBS pH 7.4 (50 mM Tris HCl, 150 mM NaCl). They were next incubated over night at 4°C in the primary antibody mixture (1% BSA, 0.1% Tween-20 in TBS). After washing in TBS, sections were incubated in the following mixture of secondary fluorescent antibodies: Alexa Fluor® 488-AffiniPure Donkey Anti-Sheep IgG (cat. n° 713-545-147), Rhodamine Red-X-AffiniPure Donkey Anti-Rat IgG (cat. n° 712-295-153) or Rhodamine

Red-X-AffiniPure Donkey Anti-Mouse IgG (cat. n° 715-295-151), Alexa Fluor® 680-AffiniPure Donkey Anti-Rabbit IgG (cat. n° 711-625-152) or Alexa Fluor® 680-AffiniPure Donkey Anti-Chicken IgG (cat. n° 703-625-155; Jackson Immunoresearch; 1:500), for 1 hour at room temperature. After rinsing in TBS, samples were mounted on coverslips with Vectashield® antifade mounting medium with DAPI (as a nuclear marker; Vector Laboratories, catalogue n° H-1200-10) and inspected with a Nikon Ti laser scanning confocal microscope, to visualize the quadruple fluorescent labelling.

Signal intensity and colocalization analysis

All confocal stacks were acquired at 40X with a Nikon Ti laser scanning confocal microscope and analysed with ImageJ. Coherent parameters were used to acquire images from PFC regions, and for the colocalization analysis of PV or SOM with OrxA or Ox2R, following Aracri et al. (2013). In brief, nonoverlapping stacks were acquired in 2-4 different sections for each neocortical region, at least one per layer (II-III and V). For two-channel colocalization analysis, tissues were excited at 488 and 568 nm or 680 and 568 nm. To avoid crosstalk, the fluorescent signals of Alexa Fluor® 488 (green), Rhodamine Red-X (red) and Alexa Fluor® 680 (far red) were detected sequentially.

To measure the total signal intensity of the far red channel in Image J, we used the SUM projection of the stack, that collects the total summed intensities of all planes, and measured the total intensity of the signal in grayscale values of pixels (Measure → Integrated density). Conversely, to assess the percentage of Ox2R^{+} pixels, we used the colocalization analysis threshold for that channel and, after image binarization, we measured the volume % of positive pixels in the stack with Analyze particles. The volume % was calculated as:

$$\frac{\sum_{i=1}^{n} area_{pixels^{+}}}{total\ pixel\ n°\ per\ plane \cdot\ n} \cdot 100$$

where *n* is the number of planes and the total pixel number per plane is 1048576 (1024 x 1024).

The colocalization of PV or SOM with either OrxA or Ox2R was determined by calculating the Manders' coefficients and performing the Intensity correlation analysis (ICA) in ImageJ (Bolte and Cordeliéres, 2006; Li et al. 2004).

The Manders' overlap coefficient is based on the Pearson's correlation coefficient and varies from 0 to 1, the former corresponding to non-overlapping images and the latter reflecting 100% colocalization between both images. M1 is defined as the ratio of the 'summed intensities of pixels from the first image for which the intensity in the other channel is

above zero' to the 'total intensity in the first channel' and M2 is defined conversely for the second channel. Therefore, M1 (or M2) is a good indicator of the proportion of the channel 1 signal coincident with a signal in channel 2 over its total intensity, and vice versa for M2. Given that the effect of the background noise is relevant for the parameters' calculation and that it is not possible to distinguish between complete and partial colocalization with the M1 and M2 coefficients, I have manually set the thresholds and added another analysis approach, Li's Intensity correlation analysis (ICA, Li et al. 2004). ICA aims to an interpretable representation of colocalization to discriminate coincidental events in a heterogeneous situation. It is assumed that the overall difference of pixel intensities from the mean intensity of the channel – each channel being taken individually – is equal to zero: $\sum_{i=1}^{n}(A_i - a) = 0$ and $\sum_{i=1}^{n}(B_i - b) = 0$ where *n* is the number of pixels, A_i is the i^{th} pixel's signal intensity in channel A, B_i is the i^{th} pixel's signal intensity in channel B, *a* is the mean signal intensity in channel A and *b* is the mean signal intensity in channel B. So:

$$\sum_{i=1}^{n}(A_i - a) \cdot \sum_{i=1}^{n}(B_i - b) \rightarrow 0$$

and, for colocalizing pixels, $\sum_{i=1}^{n}(A_i - a) \cdot \sum_{i=1}^{n}(B_i - b) \geq 0$ as each difference from the

mean is of the same sign. The differences of intensities between both channels are scaled down by fitting the histogram of both images to a 0-1 scale. ICA results are presented as a set of two graphs, each showing the normalized intensities (from 0 to 1) of each channel as a function of the product $(A_i - a) \cdot (B_i - b)$, that is directly proportional to the covariance of the two channels' intensities, defined as $\sigma_{A,B} = \frac{1}{n}\sum_{i=1}^{n}(A_i - a) \cdot (B_i - b)$. Hence, on the x axis is reported a value directly proportional to the covariance of channels A and B. On the y axis the intensity distribution is reported of channel A. The same applies to the graph about channel B. In the case of colocalization the dot cloud is mostly concentrated on the right side of the y axis, although adopting a C shape, and its spread is dependent on the intensity distribution of the current channel as a function of the covariance of both channels' intensities. On the other hand, non-colocalizing pixels are found on the left side of the plot and partial colocalization spreads the pixel cloud within the right side of the plot. Moreover, the intensity correlation quotient (ICQ) is also calculated:

$P = \sum_{i=1}^{m}(A_i - a) \cdot (B_i - b)$ where m are the pixels for which $(A_i - a) \cdot (B_i - b) > 0$

$$ICQ = \frac{P}{\sum_{i=1}^{n}(A_i - a) \cdot (B_i - b)} - 0.5$$

ICQ varies from 0.5 (colocalization) to −0.5 (exclusion), whereas random staining and images impeded by noise will give a value close to zero.

Results

OrxA stimulates glutamatergic transmission in PFC

Previous studies by our laboratory, using FVB mice, showed that OrxA 500 nM has no direct effect on pyramidal neurons' Vrest or action potential features (Coatti, 2017), even if Ox1R immunoreactivity is widely observed in layer V neuronal cell bodies (Aracri et al. 2015).

However, OrxA (500 nM) modulates the excitatory input on layer V pyramidal neurons by increasing the spontaneous EPSCs frequency recorded at -68 mV (Coatti, 2017). This suggests that orexin promotes glutamate release from excitatory terminals, in agreement with the fact that Ox1R is widely expressed in intracortical glutamatergic synaptic terminals (Aracri et al. 2015). Local presynaptic effects on neurotransmitter release are typically tested by studying miniature EPSCs (mEPSCs), revealed by application of 1 μM TTX, which blocks voltage-gated sodium channels and thus action potential-dependent vesicular release.

However, because of the subtleness of neuropeptide effects, it resulted to be difficult to study the effect of OrxA on

mEPSCs (Coatti, 2017). To overcome this limitation, I increased $[K^+]$ in the extracellular solution to 20 mM, to shift the K^+ equilibrium potential to -55 mV. We hypothesized that the ensuing partial neuronal depolarization would partially activate presynaptic calcium channels, thus allowing to reveal even subtle effects of OrxA on vesicle release. We therefore applied the following protocol to pyramidal cells voltage-clamped at -70 mV: 3 min of control recording in ACSF, 5 min in ACSF-high K^+ to disinhibit the network to a steady state of persistent depolarization, 5 min of TTX 1 µM in ACSF high K^+ to induce the AP block, 5 min of TTX 1 µM + OrxA 50 nM in ACSF-high K^+ as treatment, and a progressive washout of 3 min TTX 1 µM in ACSF high K^+, 3 min in ACSF high K^+ and 3 min in ACSF. In these conditions (Fig. 5.1), ACSF-high K^+ more than doubled the EPSC frequency (from 12.32 ± 2.36 Hz to 29.75 ± 3.77 Hz, n = 11; p-value = 0.00053). Subsequent addition of TTX only slightly reduced EPSC frequency (28.12 ± 4.51 Hz, n = 16), indicating that in high $[K^+]_o$ most of the excitatory transmission is composed of miniature events and that depolarization itself blocks firing activity, probably by increasing the fraction of inactivated V-gated Na channels. Next, OrxA 50 nM increased the mEPSC frequency by approximately 44% (40.50 ± 4.63 Hz, n = 16; p-value = 0.00176) in a reversible way (Fig. 5.3) and their median amplitude (from 9.75 ± 0.69 in TTX 1 µM + ACSF high

K^+ to 10.75 ± 0.81 pA, n = 16; p-value = 0.02647), suggesting that it may cause not only a presynaptic effect, but also a postsynaptic enhancement of glutamatergic signals.

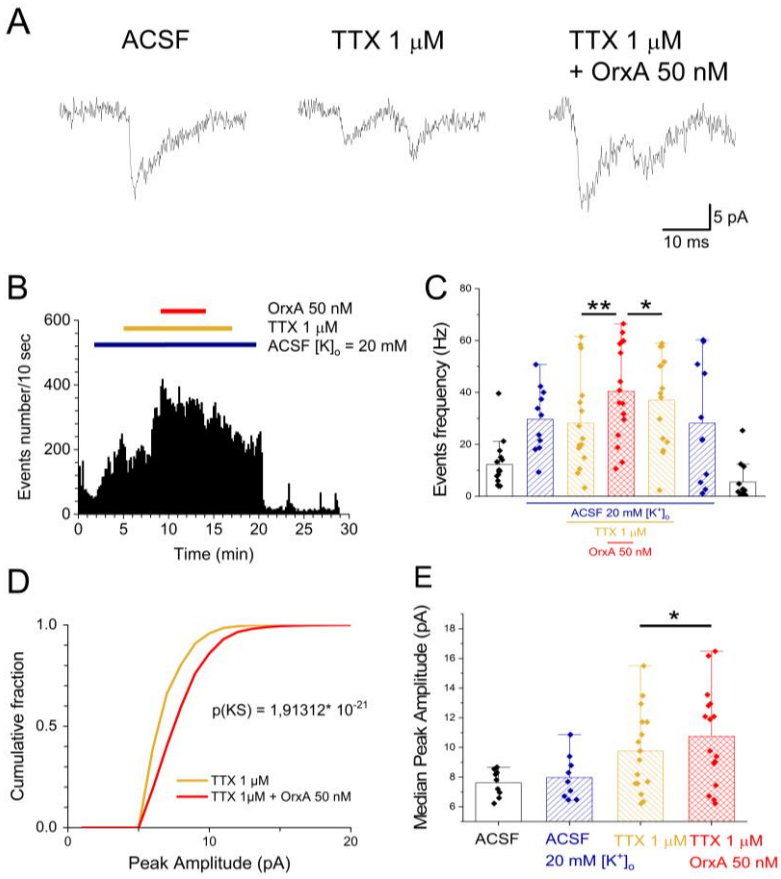

Figure 5.1. OrxA effect on miniature EPSCs in persistent depolarizing conditions. (A) Sample traces of one mEPSC per each pharmacological condition, from the same cell. (B) Typical time course of the mEPSC frequency, isolated by the administration of TTX 1 μM. Bars give the number of synaptic events measured within consecutive 10 s intervals.

Figure 5.1. *(follows)* (C) OrxA produced a significant excitatory effect. Bars give the average mEPSC frequency, calculated from 2 min continuous recording in the indicated conditions, at the steady state. On average, OrxA produced a ~ 44% increase in mEPSC frequency, bringing it from 28.12 ± 4.51 Hz to 40.50 ± 4.63 Hz ($p = 0.00176$, with paired t-test, N = 16) (D) Cumulative distribution of the mEPSC amplitudes recorded in an illustrative neuron for 2 min (steady-state) in the presence or absence of OrxA. OrxA produced a significant increase of median synaptic events amplitudes (KS test). (E) On average, OrxA produced a ~ 10% increase in mEPSC median amplitude, bringing it from 9.75 ± 0.69 to 10.75 ± 0.81 pA ($p = 0.026$, with paired t-test, N = 16) Bars give the average mEPSC median amplitude, calculated from 2 min continuous recording in the indicated conditions, at the steady state.

This EPSC stimulation exerted by OrxA was partly abolished when voltage-gated Ca^{2+} channels (Ca_V) were blocked by 100 µM Cd^{2+} (Swandulla & Armstrong, 1989; Fig. 5.2), suggesting that OrxA is able to modulate presynaptic calcium influx. Interestingly, a stimulatory effect of OrxA persisted in the presence of Cd^{2+}, suggesting that part of the OrxA action is mediated by Ca^{2+} release from intracellular stores (Leonard & Kukkonen, 2014). The slowness of recovery in the presence of Cd^{2+} could be due to Cd^{2+} interfering with the clearance phase or directly potentiating Ca^{2+} release (Choong et al. 2014).

Figure 5.2. OrxA effect on miniature EPSCs in persistent depolarizing conditions plus Cd^{2+}. (A) Sample traces of one mEPSC per each pharmacological condition, from the same cell. (B) Typical time course of the mEPSC frequency, isolated by the administration of TTX 1 µM. Bars give the number of synaptic events measured within consecutive 10 s intervals. Bars give the number of synaptic events measured within consecutive 10 s intervals. (C) OrxA produced a significant excitatory effect. Bars give the average mEPSC frequency, calculated from 2 min continuous recording in the indicated conditions, at the steady state. On average, OrxA produced a ~ 23% increase in mEPSC frequency,

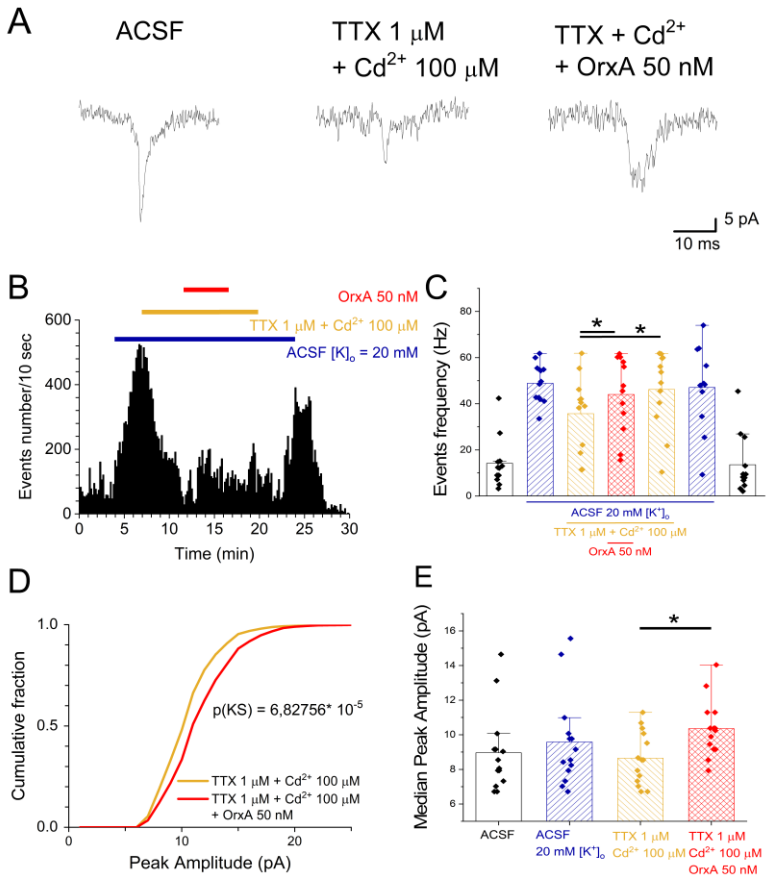

Figure 5.2. *(follows)* bringing it from 33.42 ± 4.92 Hz to 41.02 ± 5.31 Hz (p = 0.007, with paired t-test, N = 16) (D) Cumulative distribution of the mEPSC amplitudes recorded in an illustrative neuron for 2 min (steady-state) in the presence or absence of OrxA. OrxA produced a significant increase of median synaptic events amplitudes (KS test). (E) On average, OrxA produced a ~ 7% increase in mEPSC median amplitude, bringing it from 8.96 ± 0.62 to 9.58 ± 0.71 pA (p = 0.0095, with paired t-test, N = 14) Bars give the average mEPSC median amplitude, calculated from 2 min continuous recording in the indicated conditions, at the steady state.

In order to understand if the OrxA signalling acts through the modulation of glutamate receptors, and to assess the relative contribution of AMPARs and NMDARs, we repeated the same protocol with the addition of either CNQX 20 µM, a specific AMPAR blocker, or AP5 40 µM, a specific NMDAR blocker, to TTX for the same administration timespan. It seems that most events are AMPAR-dependent because their frequency is drastically reduced upon CNQX administration. On the other hand, mEPSC frequency is similarly reduced during AP5 administration but seems to be still increased by OrxA, suggesting a partial involvement of NMDARs and confirming its mainly presynaptic effect (Fig 5.3).

Figure 5.3. Effects of NMDAR and AMPAR block on miniature EPSCs enhancement in persistent depolarizing conditions. (A) Sample traces of one mEPSC per each pharmacological condition, from the same cell. (B) Typical time course of the mEPSC frequency during a recoding with CNQX 20 µM administration. Bars give the number of synaptic events measured within consecutive 10 s intervals. (C) OrxA didn't produce a significant effect on the average mEPSC frequency when AMPARs are blocked. Data calculated from 2 min continuous recording in the indicated conditions, at the steady state (4.78 ± 3.41 Hz vs 7.10 ± 4.28 Hz; p = 0.73, with paired t-test, N = 3) (D) On average, OrxA didn't produce a change in mEPSC median amplitude, with CNQX (7.17 ± 0.52 pA vs 7.26 ± 0.54 pA; p = 0.80, with paired t-test, N = 3) (E) Sama as A. (F) Typical time course of the mEPSC frequency during a recoding with AP5 40 µM administration. Bars give the number of synaptic events measured within consecutive 10 s intervals. (G) OrxA didn't produce a significant effect on the average mEPSC frequency when NMDARs are blocked. Data calculated from 2 min continuous recording in the indicated conditions, at the steady state (5.44 ± 3.23 Hz vs 8.33 ± 2.85 Hz; p = 0.41, with paired t-test, N = 4) (D) On average, OrxA didn't produce a change in mEPSC median amplitude, with AP5 (7.17 ± 0.52 pA vs 7.26 ± 0.54 pA; p = 0.80, with paired t-test, N = 4). Bars give the average mEPSC median conditions, at the steady state.

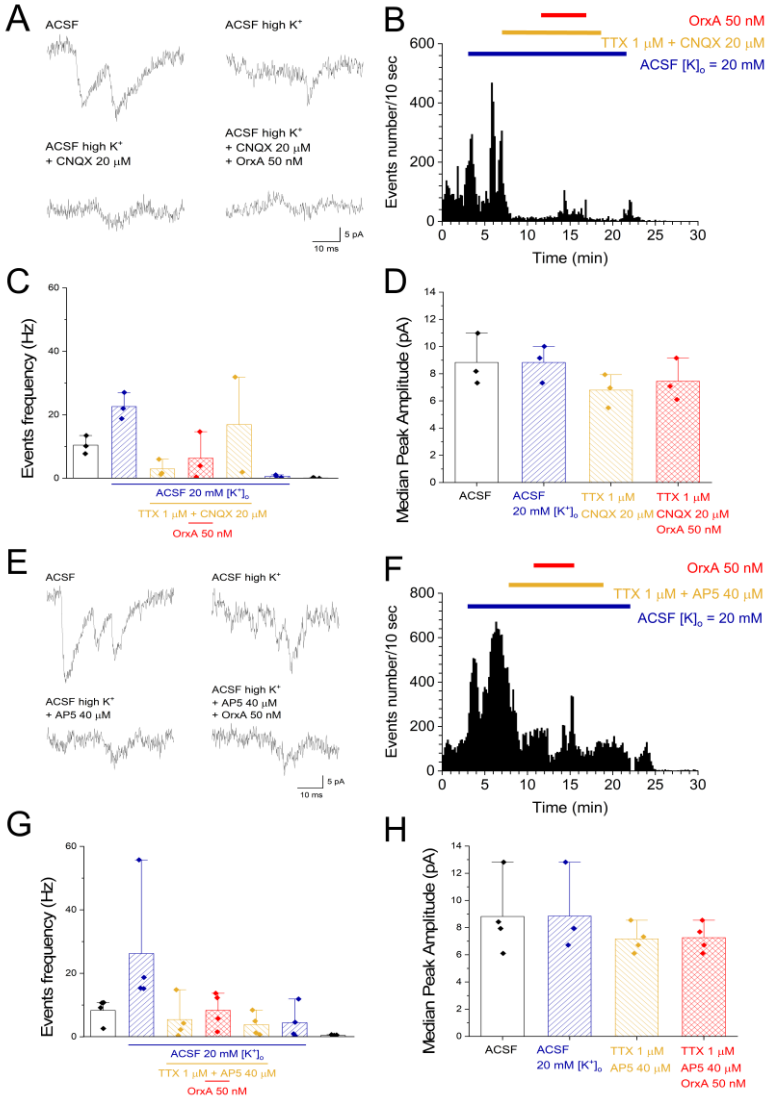
A
ACSF
ACSF high K+
ACSF high K+
+ CNQX 20 μM
ACSF high K+
+ CNQX 20 μM
+ OrxA 50 nM
5 pA
10 ms
B
OrxA 50 nM
TTX 1 μM + CNQX 20 μM
ACSF [K]o = 20 mM
Events number/10 sec
Time (min)
C
Events frequency (Hz)
ACSF 20 mM [K+]o
TTX 1 μM + CNQX 20 μM
OrxA 50 nM
D
Median Peak Amplitude (pA)
ACSF
ACSF 20 mM [K+]o
TTX 1 μM CNQX 20 μM
TTX 1 μM CNQX 20 μM OrxA 50 nM
E
ACSF
ACSF high K+
ACSF high K+
+ AP5 40 μM
ACSF high K+
+ AP5 40 μM
+ OrxA 50 nM
5 pA
10 ms
F
OrxA 50 nM
TTX 1 μM + AP5 40 μM
ACSF [K]o = 20 mM
Events number/10 sec
Time (min)
G
Events frequency (Hz)
ACSF 20 mM [K+]o
TTX 1 μM + AP5 40 μM
OrxA 50 nM
H
Median Peak Amplitude (pA)
ACSF
ACSF 20 mM [K+]o
TTX 1 μM AP5 40 μM
TTX 1 μM AP5 40 μM OrxA 50 nM

Patch-clamp on C57BL6 mice

We then extended the above study to C57BL6 mice, to achieve the following purposes: 1) to assess if our observations are robust with respect to variations in genetic background, thus warranting a greater translatability; 2) to study the specific contribution of Ox2R to the orexinergic effects on PFC, by availing of our Ox2R-Δ mice.

In agreement with the results obtained with FVB mice, OrxA 100 nM increased the mean EPSC frequency in Pys from C57 mice (data not shown). Moreover, stimulating with OrxB 100 nM or OrxB-AL 200 nM produced minor effects on the events' frequency in Pys of both C57 and in Ox2R-Δ mice (Fig. 5.4), in overall agreement with the notion that EPSCs in PFC Pys are mainly controlled by Ox1R receptors. No effect on EPSCs amplitude was found with any treatment (Fig. 5.4).

Figure 5.4. OrxB and OrxB-AL effects on EPSCs in Py neurons. (A) OrxB effects on EPSC frequency in C57BL6/J and Ox2R-Δ mice. Bars give the average EPSC frequency, calculated from 2 min continuous recording in the indicated conditions, at the steady state (N = 3 and 4) (B) OrxB effects on EPSC amplitude in C57BL6/J and Ox2R-Δ mice. Bars give the average EPSC median amplitude, calculated from 2 min continuous recording in the indicated conditions, at the steady state (N = 3 and 4) (C) OrxB-AL effects on EPSC frequency in C57BL6/J and Ox2R-Δ mice. Bars give the average EPSC frequency, calculated from 2 min continuous recording in the indicated conditions, at the steady state (N = 5 and 3) (D) OrxB-AL effects on EPSC amplitude in C57BL6/J and Ox2R-Δ mice. Bars give the average EPSC median amplitude, calculated from 2 min continuous recording in the indicated conditions, at the steady state (N = 5 and 3).

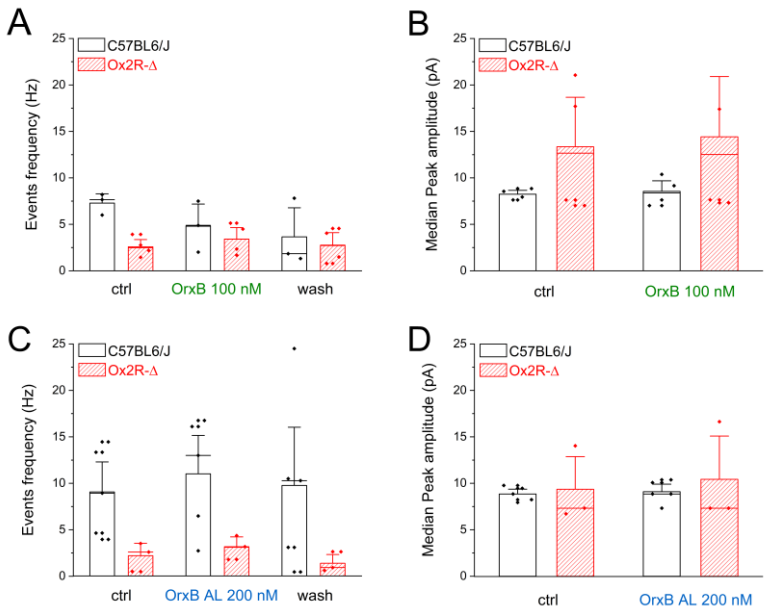

These preliminary results show that the OrxA effect on excitatory transmission seems conserved across genetic background. On the other hand, the OrxB and OrxB-AL data suggest that Ox2Rs are not much involved in the excitatory transmission regulation on Pys.

Distribution of Ox2R in murine PFC

We next studied the distribution of Ox2R by immunocytochemistry on 50 µm thick coronal slices from Ox2R-flox and Ox2R-Δ mice of both sexes. We performed quadruple stainings with: DAPI to highlight the cell nuclei and distinguish the tissue layer architecture; anti-OrxA antibody (Ab) to stain the orexinergic fibres and terminals; anti-PV Ab,

to stain the PV^+ interneuron population, mainly fast-spiking and chandelier cells (Rudy et al. 2011), or anti-SOM Ab, for the SOM^+ interneurons, mainly regular-spiking (Makram et al. 2004); and anti-Ox2R or anti-GFP Ab, for the GFP that is expressed instead of Ox2R in Ox2R-Δ mice.

The specificity of our anti-Ox2R Ab was tested by IHF on positive control reference tissue (from Ox2R-flox mice), and negative control tissues (from Ox2R-Δ mice and from Ox2R-flox mice with the specific Ab blocking peptide in the reaction mixture. We evaluated the Ox2R staining intensity by calculating the percentage of pixels showing a signal in the corresponding optical channel over the entire number of analysed pixels in the stack (1024x1024 pixels for each of the 30-40 planes of the stack, depending on the specific thickness). By this approach, we found that the 1.2 ± 0.3 % of the stack pixels were $Ox2R^+$ in the Ox2R-flox PFC (n = 6, Fig. 5.5 A), whereas the 0.7 ± 0.2 % in the Ox2R-flox + blocking peptide PFC (n = 3, Fig. 5.5 B) and the 0.2 ± 0.06% in the Ox2R-Δ brain slices (n = 3, Fig 5.5 C). The difference between Ox2R-flox and Ox2R-Δ tissue, the most appropriate negative control, is clear and statistically significant (unpaired t-test with Welch correction, p-value = 0.013), confirming the Ox2R specific staining. The signal displayed by Ox2R-flox + blocking peptide was intermediate (p-value = 0.12 compared to Ox2R-flox tissue; unpaired t-test with Welch correction;

Fig. 5.5 D), suggesting that the blocking effect of the peptide was incomplete at the stoichiometry we used (peptide vs Ab was 2:1, as suggested by the producer).

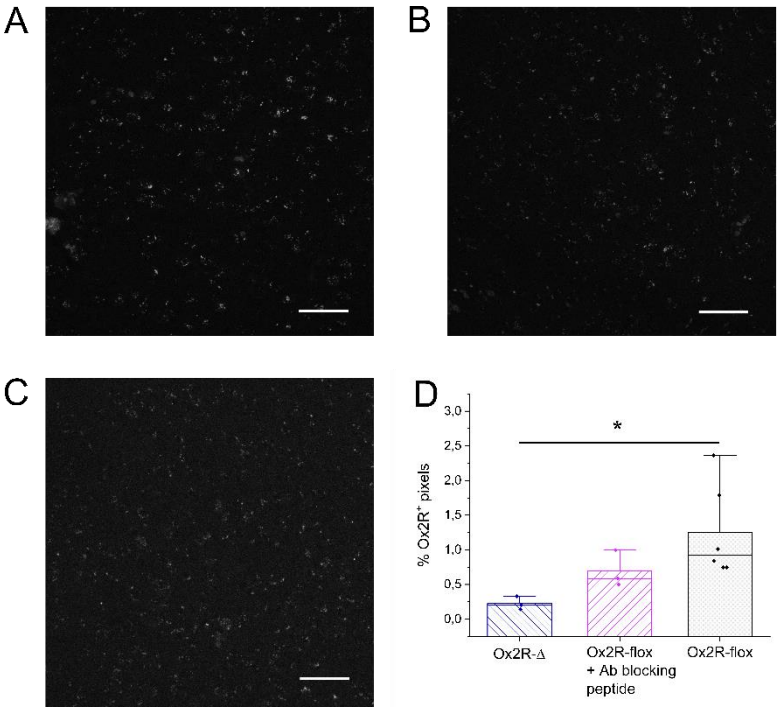

Figure 5.5. Verification of the anti-Ox2R Ab specificity. (A) Maximal intensity projection of a 40x Z-stack of a 50 µm slice processed for IHF against Ox2R (AlexaFluor 680) from Ox2R-flox tissue, mPFC layer V (B) Same as A, from Ox2R-flox tissue with anti-Ox2R Ab blocking peptide in the reaction mixture (C) Same as A, from Ox2R-Δ tissue; scale bar 50 µm (D) % or Ox2R+ pixels in the stack per slice group; the difference between Ox2R-flox and Ox2R-Δ tissue, the strongest negative control, is statistically significant (unpaired t-test with Welch correction, p-value = 0.013).

The analysis of Ox2R distribution across the two PFC subregions and their layers showed a low, speckled and

uniformly distributed signal (Two Way ANOVA for subregion and layer, p-value = 0.92; Fig. 5.6 A). The same holds true for the GFP signal in Ox2R-Δ tissue, indicating no overall difference between genotypes (Two Way ANOVA, p-value = 0.86; Fig. 5.6 B).

Figure 5.6. Distribution of the Ox2R in the murine prefrontal cortex. (A) Mean total fluorescence intensity of Ox2R (AlexaFluor 680) from Ox2R-flox tissue; comparison between PFC subregions and layers (Two Way ANOVA, p-value = 0.92) (B) Mean total fluorescence intensity of GFP (AlexaFluor 680) from Ox2R-Δ tissue; comparison between PFC subregions and layers (Two Way ANOVA, p-value = 0.86).

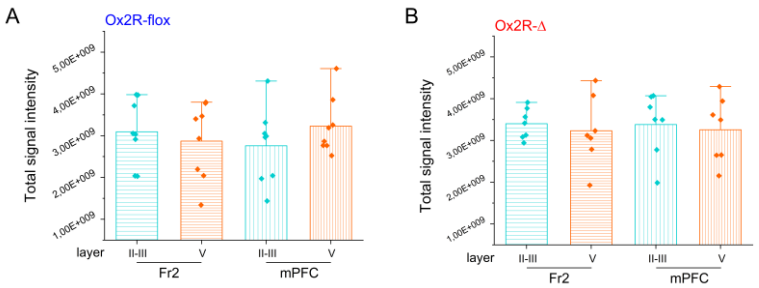

To study the distribution of the orexinergic innervation with respect to neurochemically different interneurons, we assessed the colocalization of OrxA with PV, as well as of OrxA with SOM staining in Fr2 e mPFC from Ox2R-flox mice. We repeated the same stainings also on Ox2R-Δ tissue to assess if the KO generated any variation from the physiological condition. Representative images at P105 are shown in Fig. 5.7 (A-E, OrxA:PV; F-J, OrxA:SOM). The degree of colocalization was estimated by computing the

Manders coefficients and by performing the Intensity correlation analysis (ICA). Representative ICA graphs related to the Fig. 5.7 pictures are in Fig.5.8).

Figure 5.7. Representative Fr2 IHF staining for PV^+ and SOM^+ interneurons, OrxA and Ox2R/GFP. (A-E) Maximal intensity projection of a 40x Z-stack from a 50 µm slice of Ox2R-Δ tissue, Fr2 layer V (A) merged channels (B) DAPI (C) OrxA, AlexaFluor 488 (D) PV, Rhodamine RedX (E) GFP, AlexaFluor 680 (F-J) Maximal intensity projection of a 40x Z-stack from a 50 µm slice of Ox2R-flox tissue, Fr2 layer II-III (F) merged channels(G) DAPI (H) OrxA, AlexaFluor 488 (I) SOM, Rhodamine RedX (J) Ox2R, AlexaFluor 680. Scale bar 50 µm.

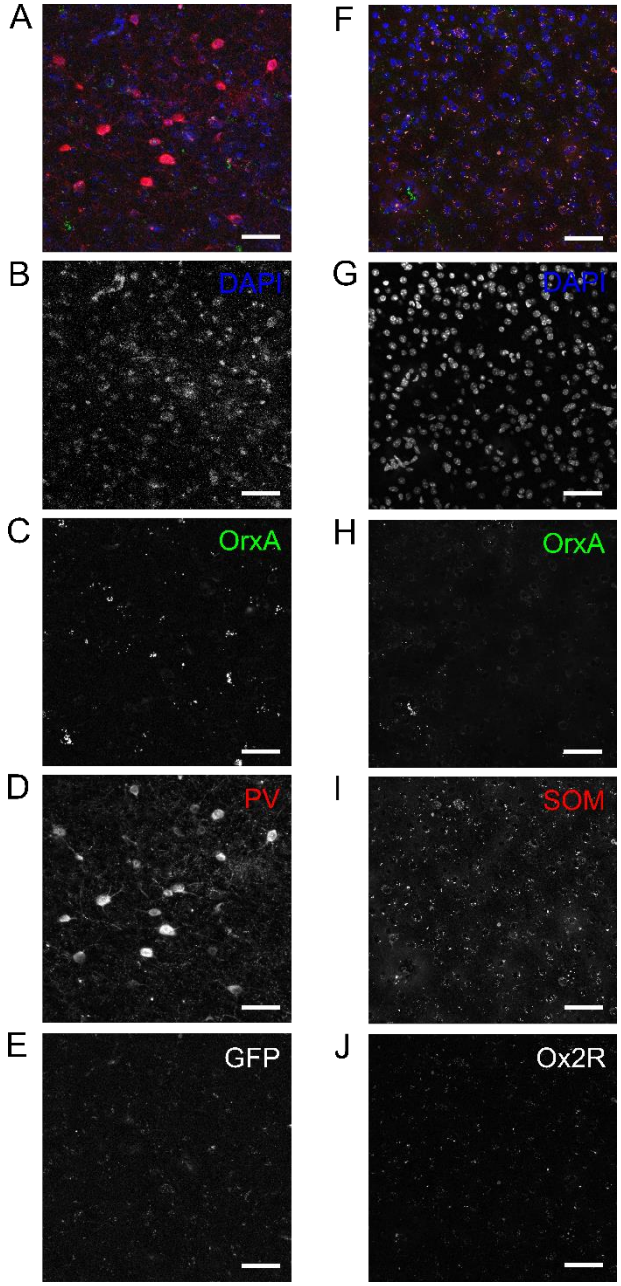
A
F
B
DAPI
G
DAPI
C
OrxA
H
OrxA
D
PV
I
SOM
E
GFP
J
Ox2R

Figure 5.8. Representative colocalization analysis. (A) Maximal intensity projection of the OrxA and PV channels; Ox2R-Δ tissue, Fr2 layer V (A') ICA graph for the OrxA channel (A'') ICA graph for the PV channel (B) Maximal intensity projection of the PV and GFP channels; Ox2R-Δ tissue, Fr2 layer V (B') ICA graph for the PV channel (B'') ICA graph for the GFP channel (C) Maximal intensity projection of the OrxA and SOM channels; Ox2R-flox tissue, Fr2 layer II-III (C') ICA graph for the OrxA channel (C'') ICA graph for the SOM channel (D) Maximal intensity projection of the OrxA and SOM channels; Ox2R-flox tissue, Fr2 layer II-III (D') ICA graph for the SOM channel (D'') ICA graph for the Ox2R channel. Scale bar 50 µm.

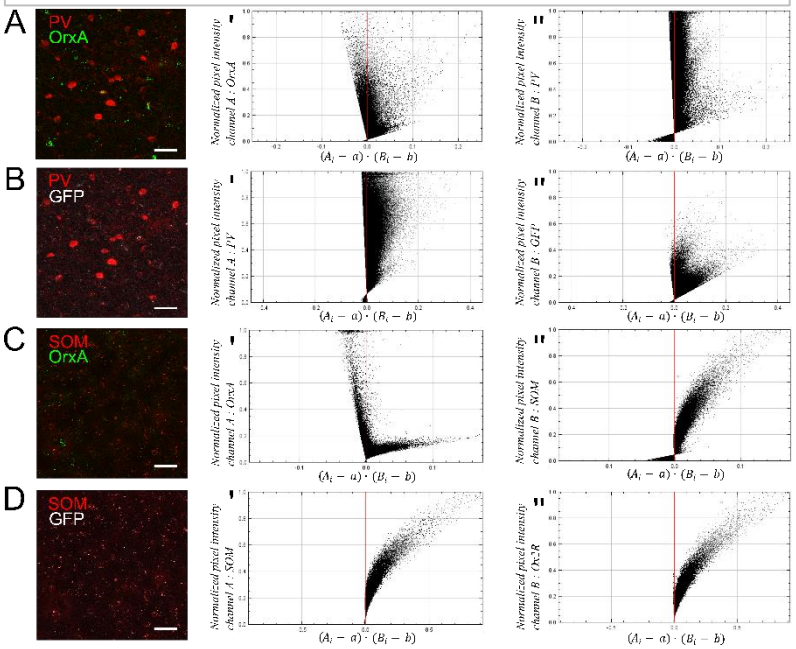

In the mature Fr2, the overlap between OrxA and PV was weak, both in layer II-III and in V. In particular, the mean M1 coefficient, indicating the proportion of colocalizing OrxA:PV signal over the OrxA total signal, was 0.31 ± 0.07 for layer II-III and 0.27 ± 0.08 for layer V; the mean M2 Manders'

coefficient, indicating the proportion of colocalizing OrxA:PV signal over the PV total signal, was 0.12 ± 0.05 for layer II-III and 0.09 ± 0.04 for layer V. The ICQ computed for the OrxA:PV colocalization was 0.11 ± 0.02 for layer II-III and 0.10 ± 0.02 for layer V, confirming some orexinergic innervation of PV^+ neurons in both Fr2 layers. In the mature mPFC, the overlap between OrxA and PV was moderate, too. In particular, the mean M1 coefficient was 0.32 ± 0.12 for layer II-III and 0.36 ± 0.12 for layer V; the mean M2 Manders' coefficient was 0.11 ± 0.03 for layer II-III and 0.12 ± 0.04 for layer V. The ICQ computed for the OrxA:PV colocalization was 0.12 ± 0.01 for layer II-III and 0.13 ± 0.02 for layer V, confirming a moderate orexinergic innervation of PV^+ neurons also in both mPFC layers (Table 5.1). In general, the OrxA:PV colocalization was not significantly different across PFC subregions or layers (Two Way ANOVA, $p\text{-value}_{M1} = 0.89$, $p\text{-value}_{M2} = 0.94$, $p\text{-value}_{ICQ} = 0.56$).

The same analysis performed on Ox2R-Δ tissue showed that the orexinergic innervation is widely conserved across genotypes. In fact, in the mature Fr2, the mean M1 coefficient was 0.24 ± 0.04 for layer II-III and 0.25 ± 0.07 for layer V; the mean M2 Manders' coefficient was 0.20 ± 0.10 for layer II-III and 0.21 ± 0.11 for layer V. The ICQ for the OrxA:PV colocalization was 0.13 ± 0.03 for layer II-III and 0.12 ± 0.03 for layer V. On the other hand, for the mature mPFC, the

mean M1 coefficient was 0.30 ± 0.12 for layer II-III and 0.36 ± 0.10 for layer V; the mean M2 Manders' coefficient was 0.15 ± 0.06 for layer II-III and 0.13 ± 0.05 for layer V. The ICQ for the OrxA:PV colocalization was 0.12 ± 0.03 for layer II-III and 0.10 ± 0.02 for layer V (Table 5.2). In general, the OrxA:PV colocalization was not significantly different across PFC subregions or layers (Two Way ANOVA, p-value$_{M1}$ = 0.58, p-value$_{M2}$ = 0.70, p-value$_{ICQ}$ = 0.82).

As for the analysis of the colocalization between OrxA and SOM, in the mature Fr2 and mPFC of both genotypes, the overlap was again moderate, both in layer II-III and in V. All the Manders' coefficients and ICQs are reported in Table 5.1 and 5.2, side by side to those related to the OrxA:PV colocalization analysis. The only significantly different colocalization index between genotypes is the ICQ for layer V of mPFC, regarding OrxA:SOM colocalization: it is higher for Ox2R-Δ than for Ox2R-flox mice (0.17 ± 0.01 vs 0.12 ± 0.008, unpaired t-test, p-value = 0.02), indicating a probably stronger innervation of SOM$^+$ interneurons in mice lacking Ox2R (Fig. 5.8 A). In general, the OrxA:SOM colocalization in Ox2R-flox tissue was not significantly different across PFC subregions or layers (Two Way ANOVA, p-value$_{M1}$ = 0.90, p-value$_{M2}$ = 0.66, p-value$_{ICQ}$ = 0.41) and the same can be said for the Ox2R-Δ tissue (Two Way ANOVA, p-value$_{M1}$ = 0.52, p-value$_{M2}$ = 0.41, p-value$_{ICQ}$ = 0.66).

Table 5.1. OrxA:PV and OrxA:SOM colocalization analysis in Ox2R-flox tissue. All values are mean ± SEM of at least 3 mice.

Region	***Layer***	***Markers***	**M1**	**M2**	**ICQ**
Fr2	*II-III*	OrxA:PV	0.31 ± 0.07	0.12 ± 0.05	0.11 ± 0.02
		OrxA:SOM	0.31 ± 0.04	0.36 ± 0.07	0.15 ± 0.02
	V	OrxA:PV	0.27 ± 0.08	0.09 ± 0.04	0.10 ± 0.02
		OrxA:SOM	0.44 ± 0.04	0.33 ± 0.05	0.14 ± 0.01
mPFC	*II-III*	OrxA:PV	0.32 ± 0.12	0.11 ± 0.03	0.12 ± 0.01
		OrxA:SOM	0.44 ± 0.08	0.39 ± 0.03	0.04±0.002
	V	OrxA:PV	0.36 ± 0.12	0.12 ± 0.04	0.13 ± 0.02
		OrxA:SOM	0.35 ± 0.04	0.37 ± 0.05	0.12±0.008

Table 5.2. OrxA:PV and OrxA:SOM colocalization analysis in Ox2R-Δ tissue. All values are mean ± SEM of at least 3 mice.

Region	***Layer***	***Markers***	**M1**	**M2**	**ICQ**
Fr2	*II-III*	OrxA:PV	0.24 ± 0.04	0.20 ± 0.10	0.13 ± 0.03
		OrxA:SOM	0.55 ± 0.16	0.24 ± 0.07	0.19 ± 0.02
	V	OrxA:PV	0.25 ± 0.07	0.21 ± 0.11	0.12 ± 0.03
		OrxA:SOM	0.50 ± 0.01	0.32 ± 0.08	0.17 ± 0.02
mPFC	*II-III*	OrxA:PV	0.30 ± 0.12	0.15 ± 0.06	0.12 ± 0.03
		OrxA:SOM	0.38 ± 0.06	0.43 ± 0.05	0.05±0.005
	V	OrxA:PV	0.36 ± 0.10	0.13 ± 0.05	0.10 ± 0.02
		OrxA:SOM	0.46 ± 0.07	0.32 ± 0.07	0.17 ± 0.01

Some interesting differences were observed between the colocalization indices of OrxA with the PV and SOM signals in the same genotype background. In fact, in the Ox2R-flox brain slices, the M2 coefficient, indicating the proportion of colocalizing signal over the PV or SOM total signal, is significantly higher for the SOM signal than for PV in all layers of both regions (the mean $M2_{SOM}$ is between 2.9 and 3.5 times the $M2_{PV}$), pointing to a denser orexinergic innervation of SOM^{+} interneurons (Fig. 5.9 B). In Ox2R-Δ tissue, conversely, only the $M1_{SOM}$ was 2 times $M1_{PV}$ in Fr2 layer V and $M2_{SOM}$ was 2.9 times $M2_{PV}$ in mPFC layer II-III (Fig. 5.9 C).

Figure 5.9. Significantly different colocalization indices for OrxA:PV/SOM analysis. (A) The ICQ for OrxA:SOM colocalization in mPFC layer V is significantly lower in Ox2R-flox tissue than in Ox2R-Δ tissue (unpaired t-test, p-value = 0.02) (B) The M2 coefficients for OrxA:PV colocalization are significantly lower than OrxA:SOM in Ox2R-flox tissue for all regions and layers (unpaired t-test, p-value = 0.04, 0.01, 0.0008, 0.007) (C) The M1 coefficient for OrxA:PV is lower than for OrxA:SOM in Fr2 layer V and the M2 coefficient for OrxA:PV is lower than for OrxA:SOM in mPFC layer II-III in Ox2R-Δ tissue (unpaired t-test, p-value = 0.03, 0.02). * p-value < 0.05 ** p-value < 0.01

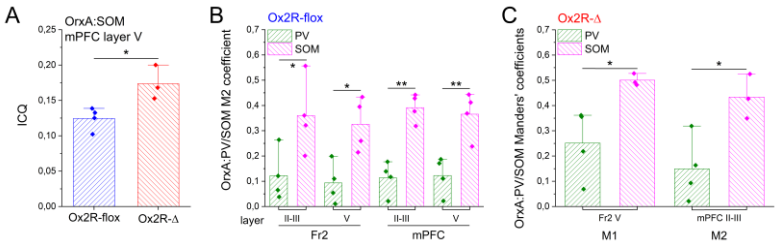

The same approach was followed to analyse the distribution of Ox2R with respect to neurochemically different interneurons, PV^+ and SOM^+, in both Fr2 e mPFC from Ox2R-flox and Ox2R-Δ mice. All the results are reported in Table 5.3 and 5.4. In general, the PV:Ox2R colocalization wasn't significantly different in Ox2R-flox tissue across PFC subregions or layers, but for the ICQ, which is slightly higher in mPFC vs Fr2 (Two Way ANOVA, $p\text{-value}_{M1} = 0.26$, $p\text{-value}_{M2} = 0.96$, $p\text{-value}_{ICQ} = 0.04$) and the same holds true for the SOM:Ox2R colocalization (Two Way ANOVA, $p\text{-value}_{M1} = 0.17$, $p\text{-value}_{M2} = 0.90$, $p\text{-value}_{ICQ} = 0.61$). The results are analogous for the Ox2R-Δ tissue (Two Way ANOVA, $p\text{-value}_{M1} = 0.54$, $p\text{-value}_{M2} = 0.17$, $p\text{-value}_{ICQ} = 0.22$ for PV:GFP and $p\text{-value}_{M1} = 0.68$, $p\text{-value}_{M2} = 0.11$, $p\text{-value}_{ICQ} = 0.78$ for SOM:GFP). The colocalization of Ox2R or GFP with PV in the mPFC was different between genotypes; in fact, ICQs for both layer II-III and V are significantly lower in Ox2R-Δ mice (0.06 ± 0.007 vs 0.04 ± 0.004, p-value = 0.02, and 0.06 ± 0.002 vs 0.04 ± 0.002, p-value = 0.0004, unpaired t-test with Welch correction, Fig. 5.10 A). Moreover, M1 is lower in Ox2R-Δ Fr2 layer V (0.04 ± 0.01 vs 0.15 ± 0.03, unpaired t-test, p-value = 0.02, Fig. 5.10 B).

Table 5.3. PV:Ox2R and SOM:Ox2R colocalization analysis in Ox2R-flox tissue. All values are mean ± SEM of at least 3 mice.

Region	***Layer***	***Markers***	**M1**	**M2**	**ICQ**
Fr2	*II-III*	PV:Ox2R	0.05 ± 0.01	0.43 ± 0.07	0.05± 0.003
		SOM:Ox2R	0.19 ± 0.03	0.49 ± 0.07	0.04 ± 0.002
	V	PV:Ox2R	0.04 ± 0.01	0.41 ± 0.09	0.06 ± 0.02
		SOM:Ox2R	0.19 ± 0.01	0.53 ± 0.06	0.04 ± 0.003
mPFC	*II-III*	PV:Ox2R	0.06 ± 0.01	0.38 ± 0.09	0.06 ± 0.007
		SOM:Ox2R	0.26 ± 0.02	0.58 ± 0.09	0.04 ± 0.002
	V	PV:Ox2R	0.05 ± 0.01	0.43 ± 0.09	0.06 ± 0.002
		SOM:Ox2R	0.23 ± 0.04	0.49 ± 0.06	0.04 ± 0.002

Table 5.4. PV:GFP and SOM:GFP colocalization analysis in Ox2R-Δ tissue. All values are mean ± SEM of at least 3 mice.

Region	***Layer***	***Markers***	**M1**	**M2**	**ICQ**
Fr2	*II-III*	PV:GFP	0.08 ± 0.02	0.31 ± 0.05	0.05 ± 0.006
		SOM:GFP	0.16 ± 0.06	0.51 ± 0.01	0.05 ± 0.005
	V	PV:GFP	0.15 ± 0.03	0.35 ± 0.08	0.06 ± 0.02
		SOM:GFP	0.22 ± 0.04	0.57 ± 0.02	0.05 ± 0.006
mPFC	*II-III*	PV:GFP	0.12 ± 0.03	0.44 ± 0.11	0.04 ± 0.004
		SOM:GFP	0.29 ± 0.07	0.58 ± 0.04	0.05 ± 0.005
	V	PV:GFP	0.11 ± 0.02	0.51 ± 0.09	0.04 ± 0.002
		SOM:GFP	0.16 ± 0.02	0.60 ± 0.03	0.05 ± 0.003

Some other interesting differences were observed between the colocalization indices of Ox2R with the PV and SOM

signals in the same genotype background. In fact, in the Ox2R-flox brain slices, the M1 coefficient, indicating the proportion of colocalizing signal over the PV or SOM total signal, was significantly higher for the SOM signal than for PV in all layers of both regions (the mean $M1_{SOM}$ is between 4.2 and 4.8 times the $M1_{PV}$), pointing to higher expression of Ox2R on SOM^+ interneurons (Fig. 5.10 C). This is, however, paralleled by a 1.3-1.6 times higher ICQ_{PV}, compared to the ICQ_{SOM}, in Fr2 layer II-III, and mPFC layer II-III and V (Fig. 5.10 D). On the other hand, in Ox2R-Δ tissue, the only significant difference is the 1.7 times higher $M2_{SOM}$, compared to $M2_{PV}$, in Fr2 layer II-III (Fig. 5.10 E).

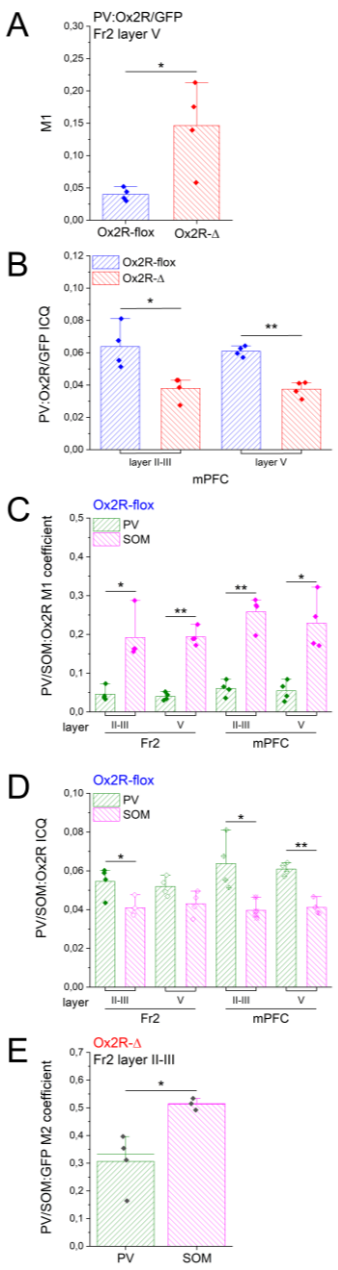

Figure 5.10. Significantly different colocalization indices for PV/SOM:Ox2R/GFP analysis. (A) The M1 for PV:Ox2R/GFP colocalization in Fr2 layer V is significantly higher in Ox2R-Δ mice than in Ox2R-flox tissue (unpaired t-test, p-value = 0.047) (B) The ICQ coefficient for PV:Ox2R/GFP colocalization is significantly lower in Ox2R-Δ mPFC than in Ox2R-flox (unpaired t-test, p-value = 0.02, 0.0004) (C) The M1 coefficient for PV:Ox2R/GFP is lower than for SOM:Ox2R/GFP in all subregions and layers of Ox2R-flox tissue (unpaired t-test, p-value = 0.05, 0.0002, 0.0007, 0.01) (D) The ICQ for PV:Ox2R/GFP is higher than for SOM:Ox2R/GFP in almost all subregions and layers in Ox2R-flox tissue (unpaired t-test, p-value = 0.03, 0.07, 0.03, 0.0003) (E) The M2 coefficient for PV:Ox2R/GFP is lower than for SOM:Ox2R/GFP in Fr2 layer II-III of Ox2R-Δ tissue (unpaired t-test, p-value = 0.02). * p-value < 0.5 ** p-value < 0.01

Discussion

Effects of OrxA and OrxB on the PFC excitatory network

Our study showed that orexins modulate the excitatory network of the murine PFC in a complex fashion. In fact, OrxA increases the frequency of EPSCs in Pys from both the FVB and the C57BL6 strain, suggesting a conserved excitatory role for the neuropeptide that was previously proved to be Ox1R-dependent by SB 3348671 block in FVB mice (Coatti, 2017). The increase of EPSC frequency is likely to be of presynaptic origin because it is also observed on mEPSCs, although in ACSF with high K. A postsynaptic effect of OrxA is also possible, as a small increase in the mEPSC median amplitude was observed in presence of OrxA. This would be consistent with previous histological analysis showing Ox1R localization on both cell bodies and neuropil, with a stronger signal in Fr2 layer V (Aracri et al. 2015).

The effect of OrxA on the synaptic events was only partially dependent on L-type Ca_V channels, as the effect of Cd^{2+} was not complete (Swandulla & Armstrong, 1989). This suggests that orexinergic signaling could also act through release of calcium from intracellular stores, which would also explain the slower washout of OrxA effect in the presence of Cd^{2+}. In fact, Cd^{2+} has been shown to directly potentiate intracellular Ca^{2+} release (Choong et al. 2014). Such interpretation would be in

accordance with numerous studies of the OxRs' downstream signalling pathways, which involve the $G_{q/11}$, $G_{i/o}$, and G_s proteins, and in turn PLC-IP_3/DAG, PLD/phosphatic acid, PLA/arachidonic acid, and mitogen-activated protein kinase (MAPK) cascades (Wang et al. 2018). In neuron-like cells, orexin receptors' activation usually involves the activation of PLC and $[Ca^{2+}]_i$ elevation (Holmqvist et al. 2002, Ozcan et al. 2010): OrxA elevates $[Ca^{2+}]_i$ by activating L- and N-type Ca^{2+} channels, an effect mediated by phosphatidylcholine-specific PLC and PKC in dopaminergic neurons (Uramura et al. 2001); the action of OrxA on Ox1R induces an increase of $[Ca^{2+}]_i$ in juvenile rat prefrontal cortex neurons, dependent upon extracellular Ca^{2+} influx via L-type Ca^{2+} channels activated by the intracellular PLC–PKC signalling pathway (Xia et al. 2009); OrxA directly excites layer II/III Pys in the mPFC of juvenile rats through an Ox1R – K and non-selective cationic channels pathway (Yan et al. 2012); OrxA acts on OX1R–PLC–PKC to upregulate the voltage-gated L-type calcium channel, which subsequently activates the hypothalamic AMPK signalling pathway in NPY neurons (Wu et al. 2013). Moreover, orexins have also been shown to increase postsynaptic $[Ca^{2+}]_i$ via Ox2R, and the increase in $[Ca^{2+}]_i$ is induced by the AC-PKA–mediated activation of voltage-gated R- and T-type Ca^{2+} channels (Nakamura et al. 2010). However, more studies are needed to understand the

precise mechanism by which OrxA exerts its effects on the murine prefrontal cortex, because the landscape of the possible pathways and signalling intermediates is variegated and shows differences across age and animal models.

However, OrxB and OrxB-AL do not seem to be much involved in the excitatory transmission regulation on Pys, suggesting a secondary role for Ox2Rs. This differs, however, from what reported by some authors (Bayer et al. 2002; Lambe & Aghajanian, 2003; Bayer et al. 2004; Lambe et al. 2005), but it could be due to a species or region-dependent divergence, whose physiological meaning needs further investigation.

Given this complex landscape of possible interactions and responses, the most likely mechanism for the observed orexinergic effects on layer V Fr2 Pys is the following: the excitatory effect of orexins on these neurons is mainly mediated by Ox1Rs, probably representing a mostly presynaptic contribution, to which a postsynaptic effect adds up, and both of them partially depend on the activation of L-type Ca_V channels. However, more studies are needed to clarify this complex signalling landscape.

Ox1R and Ox2R distribution in the PFC

Previous work by our team (Aracri et al. 2015) showed the Ox1R distribution by immunocytochemistry in coronal

sections of Fr2, layer V. An intense and diffuse signal was observed, with immunoreactive spots on cell bodies of large and medium size neurons as well as in the neuropil. Double staining with Ox1R/GAD65 showed little colocalization in Fr2, so Ox1R is rarely expressed by GABAergic fibres. Similarly, virtually no colocalization was observed with terminals stained by anti-parvalbumin (PV) antibodies, PV being a marker for FS neurons and chandelier cells (Rudy et al. 2011). However, the colocalization of Ox1R with both GAD65 and PV revealed a diffuse labelling on the cell bodies of a subpopulation of GABAergic interneurons expressing Ox1R. The specific neurochemical nature of these neurons remains to be specified, but a recent paper on cingulate cortex, which is in anatomofunctional continuity with mPFC, suggests that they are nNOS/NK1R^{+}, one of the rarest groups of GABAergic neurons (Williams et al. 2019). On the other hand, the Ox1R's colocalization with the glutamatergic terminal marker vesicular glutamate transporter 1 (VGLUT1) showed a widespread colocalization on the neuropilar synaptic terminals that take contact with the Ox1R^{+} cell bodies, whereas Ox1R and VGLUT2 revealed scarce colocalization. Since VGLUT1 is mainly expressed by intracortical terminals and VGLUT2 by extrinsic afferent (mainly thalamocortical) glutamatergic fibres (Hur and Zaborsky 2005; Nakamura et

al. 2005; Graziano et al. 2008), this means that Ox1R tends to selectively regulate intracortical transmission.

Our present data on the Ox2R distribution are preliminary but already significant under some aspects. The analysis of the distribution of the Ox2R by IHF highlighted a diffuse, speckled signal around putative cell bodies and in the neuropil with no clear subregion or layer-specific staining. The GFP signal in the Ox2R-Δ tissue showed a similar distribution, as well (Fig. 5.8).

The analysis of both OrxA:PV and OrxA:SOM colocalization was not significantly different across PFC subregions or layers, indicating a fairly uniform innervation of PV^+ and SOM^+ interneurons located in different PFC subregions and layers in both genotype backgrounds. However, differences between orexinergic innervation of neurochemically different interneurons seem to be present in Ox2R-flox animals: the M2 coefficient, indicating the proportion of colocalizing signal over the PV or SOM total signal, is significantly higher for the SOM signal than for PV in all layers of both regions (the mean $M2_{SOM}$ is between 2.9 and 3.5 times the $M2_{PV}$), pointing to a denser orexinergic innervation of SOM^+ interneurons (Fig. 5.10 B). In the Ox2R-Δ tissue, conversely, only the $M2_{SOM}$ was 2.9 times $M2_{PV}$ in mPFC layer II-III (Fig. 5.10 C), so this seems to be a variable feature between genetic backgrounds.

However, when compared directly between Ox2R-flox and Ox2R-Δ tissue, the only different colocalization index is ICQ for mPFC layer V, which is higher in Ox2R-Δ (5.10 A), suggesting a putatively stronger innervation of SOM^+ interneurons in mice lacking Ox2R in a kind of compensatory fashion.

On the other hand, the analysis of both PV:Ox2R/GFP and SOM:Ox2R/GFP colocalization wasn't significantly different across PFC subregions or layers but for the ICQ, which is slightly higher in mPFC vs Fr2 for Ox2R-flox tissue, indicating a mainly uniform expression of Ox2R or its substitute GFP in PV^+ and SOM^+ interneurons located in different PFC subregions and layers in both genotype backgrounds. Moreover, differences between the Ox2R expression of neurochemically different interneurons seem to be present in Ox2R-flox animals: the M1 coefficient, indicating the proportion of colocalizing signal over the PV or SOM total signal, is significantly higher for the SOM signal than for PV in all layers of both regions (the mean $M1_{SOM}$ is between 4.2 and 4.8 times the $M1_{PV}$), pointing to higher expression of Ox2R on SOM^+ interneurons (Fig. 5.12 C). However, the ICQ_{PV} is 1.3-1.6 times higher than ICQ_{SOM}, in Fr2 layer II-III, and mPFC layer II-III and V (Fig. 5.12 D), suggesting an opposite interpretation. This might be related to the background noise, which may affect the M2 coefficient more

than the ICQ, but it is unlikely that the observed 4-5 x fold change in this value is only due to noise. It may rather be due to a different sensitivity of the two indices to the colocalization of the PV or SOM signals with that of Ox2R. In fact, the SOM staining is much more widespread than the PV one due to the intrinsically different nature of the marker (parvalbumin is a Ca^{2+}-chelating agent, highly expressed in the cytoplasm and giving a uniform staining of somata; conversely, somatostatin is a neurotransmitter, generally highly concentrated in intracellular vesicles, and giving a diffuse and speckled signal). To better assess if SOM^+ interneurons do express more Ox2Rs than PV^+ ones, other assays are needed, such as mRNA fluorescence in situ hybridization or real-time PCR on fluorescence-based sorted SOM^+ and PV^+ cells after tissue digestion. Overall, this preliminary IHF data suggest that SOM^+ interneurons are more sensitive than PV^+ ones to the orexinergic input in the whole PFC, both because they seem to be more densely innervated by $OrxA^+$ fibres and because they may express more Ox2Rs. This result is in line with the idea that orexins regulate rhythmogenesis in the PFC at frequencies around the θ band, given that SOM^+ interneurons are involved in the generation of ≈ 10 Hz oscillations in the pyramidal neuron activity in the neocortex (Hilscher et al. 2017) as well as in θ rhythm generation in the hippocampus (Amilhon et al. 2015; Mikulovic, 2016; Mikulovic

et al. 2018). Moreover, SOM^+ interneurons chemogenetic activation increases EEG θ activity in M2 region, the premotor cortex, in close connection with Fr2/Fr2 (Funk et al. 2017), strongly suggesting an implication of SOM^+ interneurons in rhythm generation in the PFC.

Effects on θ rhythmogenesis

Orxs have an impact on θ rhythmogenesis, as proved by both animal and human studies. In fact, Orx loss in $Orx^{KO/KO}$ mice, which mimics the orexin depletion associated to narcolepsy, causes impaired TDW maintenance in baseline wake (Vassalli & Franken, 2017). Moreover, the brain activity of $Orx^{KO/KO}$ mice exhibits stereotypical ~2-s-long very high-amplitude hypersynchronous paroxysmal theta bursts in the PFC at the onset of cataplexy attacks, preceding the hippocampal θ activity commonly associated with cataplexy and REM sleep (Vassalli, et al. 2013). Similar paroxysmal θ bursting events were evidenced during cataplexy attacks of narcoleptic children. Orxs are thus implied in the emergence of paroxysmal cortical oscillations, suggestive of a cortical microcircuit direct involvement in early cataplexy cortical hypersynchronies in the θ band.

The balance of OrxA and OrxB and their stability in extracellular fluid are unknown. At the present stage, we can hypothesize two mechanisms by which a strong decrease of

Orx signals could lead to a paroxysmal increase in PFC θ activity associated with cataplexies.

1) Because some lines of evidence indicate that OrxB levels in the brain are 2-3 times higher than OrxA levels (Mondel et al. 1999), it is possible that the deletion of OrxA and OrxB could have stronger effects on SOM^+ interneurons (mainly expressing Orx2R). Relieving a tonic stimulation of these interneurons could release Py cell activity, clustered around theta.

2) Deletion of OrxA and OrxB could cause a compensatory effect by increasing the complement of the receptors implicated in the other ascending excitatory pathways (e.g., the cholinergic), thus facilitating the onset of Py cell-dependent θ waves in PFC.

References

Alonso, A., Khateb, A., Fort, P., Jones, B.E., & Muhlethaler, M. (1996). Differential oscillatory properties of cholinergic and noncholinergic nucleus basalis neurons in guinea pig brain slice. European journal of neuroscience 8, 169-182.

Amilhon, B., Huh, C. Y., Manseau, F., Ducharme, G., Nichol, H., Adamantidis, A., & Williams, S. (2015). Parvalbumin interneurons of hippocampus tune population activity at theta frequency. Neuron, 86, 1277-1289.

Ammoun, S., Holmqvist, T., Shariatmadari, R., Oonk, H. B., Detheux, M., Parmentier, M., ... & Kukkonen, J. P. (2003). Distinct recognition of OX1 and OX2Receptors by orexin peptides. Journal of Pharmacology and Experimental Therapeutics, 305, 507-514.

Aracri, P., Amadeo, A., Pasini, M.E., Fascio, U., & Becchetti, A. (2013) Regulation of glutamate release by heteromeric nicotinic receptors in layer V of the secondary motor region (Fr2) in the dorsomedial shoulder of prefrontal cortex in mouse. Synapse, 67, 338-357.

Aracri, P., Banfi, D., Pasini, M.E., Amadeo, A., Becchetti, A. (2015) Orexin (hypocretin) regulates glutamate input to fast-spiking interneurons in layer V of the Fr2 region of the murine prefrontal cortex. Cereb. Cortex, 25, 1330-1347.

Asahi, S., Egashira, S. I., Matsuda, M., Iwaasa, H., Kanatani, A., Ohkubo, M., ... & Morishima, H. (2003). Development of an orexin-2 receptor selective agonist, [Ala11, D-Leu15] orexin-B. Bioorganic & medicinal chemistry letters, 13, 111-113.

Baimel, C., Lau, B.K., Qiao, M. & Borgland, S.L. (2017) Projection-target-defined effects of orexin and dynorphin on VTA dopamine neurons. Cell Rep. 18, 1346-1355.

Bayer, L., Eggermann, E., Saint-Mleux, B., Machard, D., Jones, B. E., Mühlethaler, M., & Serafin, M. (2002). Selective action of orexin (hypocretin) on nonspecific thalamocortical projection neurons. Journal of Neuroscience, 22, 7835-7839.

Bayer, L., Serafin, M., Eggermann, E., Saint-Mleux, B., Machard, D., Jones, B. E., & Mühlethaler, M. (2004). Exclusive postsynaptic action of hypocretin-orexin on sublayer 6b cortical neurons. Journal of Neuroscience, 24, 6760-6764.

Bolte, S., & Cordelières, F.P. (2006). A guided tour into subcellular colocalization analysis in light microscopy. J. Microsc. 224, 213-232.

Castro-Alamancos, M.A., Rigas, P., & Tawara-Hirata, Y. (2007). Resonance (approximately 10 Hz) of excitatory networks in motor cortex: effects of voltage-dependent ion channel blockers. Journal of physiology 578, 173-191.

Choong, G., Liu, Y., & Templeton, D. M. (2014). Interplay of calcium and cadmium in mediating cadmium toxicity. Chemico-biological interactions, 211, 54-65.

Coatti, A. (2017) Heteromeric nicotinic receptors regulate developing and mature prefrontal circuits: interaction with other neuromodulators, and implications for sleep-related hypermotor epilepsy. PhD Thesis, University of Milano-Bicocca.

Cohen, M. X. (2014). A neural microcircuit for cognitive conflict detection and signaling. Trends in neurosciences, 37, 480-490.

Dahan, L., Astier, B., Vautrelle, N., Urbain, N., Kocsis, B. & Chouvet, G. Prominent burst firing of dopaminergic neurons in the ventral tegmental area during paradoxical sleep. Neuropsychopharmacology 32, 1232-1241 (2007).

Eban-Rothschild, A., Rothschild, G., Giardino, W.J., Jones, J.R. & de Lecea, L. VTA dopaminergic neurons regulate ethologically relevant sleep-wake behaviors. Nat. Neurosci. 19, 1356-1366 (2016).

Eban-Rothschild, A., Borniger, J.C., Rothschild, G., Giardino, W.J., Morrow, J.G. & de Lecea, L. (2020) Arousal state-dependent alterations in VTA-GABAergic neuronal activity. eNeuro 7, 1-13.

Floresco, S.B., West, A.R., Ash, B., Moore, H. & Grace, A.A. Afferent modulation of dopamine neuron firing differentially regulates tonic and phasic dopamine transmission. Nat. Neurosci. 6, 968-973 (2003)

Funk, C. M., Peelman, K., Bellesi, M., Marshall, W., Cirelli, C., & Tononi, G. (2017). Role of somatostatin-positive cortical interneurons in the generation of sleep slow waves. Journal of Neuroscience, 37, 9132-9148.

Graziano, A., Liu, X.-B., Murray, K.D., & Jones, E.G. (2008). Vesicular glutamate transporters define two sets of glutamatergic afferents to the somatosensory thalamus and two thalamocortical projections in the mouse. J. Comp. Neurol. 507, 1258-1276.

He, C., Chen, Q.H., Ye, J.N., Li, C., Yang, L., Zhang, J., Xia, J.X., & Hu, Z.A. (2015). Functional inactivation of hypocretin 1 receptors in the medial prefrontal cortex affects the pyramidal neuron activity and gamma oscillations: An in vivo multiple-channel single-unit recording study. Neuroscience 297, 1-10.

Hilscher, M.M., Leão, R.N., Edwards, S.J., Leão, K.E., & Kullander, K. (2017). Chrna2-Martinotti Cells Synchronize Layer 5 Type A Pyramidal Cells via Rebound Excitation. PLoS Biol. 15:e2001392.

Holmqvist, T., Akerman, K.E., & Kukkonen, J.P. (2002). Orexin signaling in recombinant neuron-like cells. FEBS Lett. 256, 11-14.

Lambe, E. K., & Aghajanian, G. K. (2003). Hypocretin (orexin) induces calcium transients in single spines postsynaptic to identified thalamocortical boutons in prefrontal slice. Neuron, 40, 139-150.

Lambe, E. K., Olausson, P., Horst, N. K., Taylor, J. R., & Aghajanian, G. K. (2005). Hypocretin and nicotine excite the same thalamocortical synapses in prefrontal cortex: correlation with improved attention in rat. Journal of Neuroscience, 25, 5225-5229.

Li, B., Chen, F., Ye, J., Chen, X., Yan, J., Li, Y., Xiong, Y., Zhou, Z., Xia, J., & Hu, Z. (2010). The modulation of orexin A on HCN currents of pyramidal neurons in mouse prelimbic cortex. Cerebral cortex 20, 1756-1767.

Li, Q., Lau, A., Morris, T. J., Guo, L., Fordyce, C. B., & Stanley, E. F. (2004). A syntaxin 1, Gαo, and N-type calcium channel complex at a presynaptic nerve terminal: analysis by quantitative immunocolocalization. Journal of Neuroscience, 24, 4070-4081.

Markram, H., Toledo-Rodriguez, M., Wang, Y., Gupta, A., Silberberg, G., & Wu, C. (2004). Interneurons of the neocortical inhibitory system. Nature reviews neuroscience, 5, 793-807.

Mikulovic, S. (2016). On the Mechanisms Behind Hippocampal Theta Oscillations: The role of OLMα2 interneurons. Doctoral dissertation, Acta Universitatis Upsaliensis.

Mikulovic, S., Restrepo, C. E., Siwani, S., Bauer, P., Pupe, S., Tort, A. B., ... & Leão, R. N. (2018). Ventral hippocampal OLM cells control type 2 theta oscillations and response to predator odor. Nature communications, 9, 1-15.

Nakamura, Y., Miura, S., Yoshida, T., Kim, J., & Sasaki, K. (2010). Cytosolic calcium elevation induced by orexin/hypocretin in granule cell domain cells of the rat cochlear nucleus in vitro. Peptides, 31, 1579-1588.

Ozcan, M., Ayar, A., Serhatlioglu, I., Alcin, E., Sahin, Z., & Kelestimur, H. (2010). Orexins activates protein kinase C-mediated Ca2+ signaling in isolated rat primary sensory neurons. Physiol. Res. 59, 255-262.

Peyron, C., Tighe, D. K., Van Den Pol, A. N., De Lecea, L., Heller, H. C., Sutcliffe, J. G., & Kilduff, T. S. (1998). Neurons containing hypocretin (orexin) project to multiple neuronal systems. Journal of Neuroscience, 18, 9996-10015.

Rudy, B., Fishell, G., Lee, S., & Hjerling-Leffler, J. (2011). Three groups of interneurons account for nearly 100% of neocortical GABAergic neurons. Dev. Neurobiol. 71, 45-61.

Sakurai, T., Amemiya, A., Ishii, M., Matsuzaki, I., Chemelli, R. M., Tanaka, H., ... & Yanagisawa, M. (1998). Orexins and orexin receptors: a family of hypothalamic neuropeptides and G protein-coupled receptors that regulate feeding behavior. Cell, 92, 573-585.

Sakurai, T. (2014). The role of orexin in motivated behaviours. Nature Reviews Neuroscience, 15, 719-731.

Silva, L.R., Amitai, Y., & Connors, B.W. (1991). Intrinsic oscillations of neocortex generated by layer 5 pyramidal neurons. Science 251, 432-435.

Soya, S., & Sakurai, T. (2020). Evolution of orexin neuropeptide system: Structure and function. Frontiers in Neuroscience, 14, 691.

Sutcliffe, J.G., & de Lecea, L. (2002). The hypocretins: setting the arousal threshold. Nature Rev Neurosci 3, 339-349.

Swandulla, D., & Armstrong, C. M. (1989). Calcium channel block by cadmium in chicken sensory neurons. Proc Natl Acad Sci (USA) 86, 1736-1740.

Tsintsadze, T., Williams, C. L., Weingarten, D. J., Von Gersdorff, H., & Smith, S. M. (2017). Distinct actions of voltage-activated Ca2+ channel block on spontaneous release at excitatory and inhibitory central synapses. J. Neurosci. 37, 4301-4310.

Uramura, K., Funahashi, H., Muroya, S., Shioda, S., Takigawa, M., & Yada, T. (2001). Orexin-a activates phospholipase C- and protein

kinase C-mediated Ca2+ signaling in dopamine neurons of the ventral tegmental area. Neuroreport. 12:1885-1889.

Vassalli, A., Dellepiane, J. M., Emmenegger, Y., Jimenez, S., Vandi, S., Plazzi, G., ... & Tafti, M. (2013). Electroencephalogram paroxysmal theta characterizes cataplexy in mice and children. Brain, 136, 1592-1608.

Vassalli, A., & Franken, P. (2017). Hypocretin (orexin) is critical in sustaining theta/gamma-rich waking behaviors that drive sleep need. Proceedings of the National Academy of Sciences, 114, E5464-E5473.

Wang, C., Wang, Q., Ji, B., Pan, Y., Xu, C., Cheng, B., ... & Chen, J. (2018). The orexin/receptor system: molecular mechanism and therapeutic potential for neurological diseases. Front. Mol. Neurosci. 11, 220.

Wang, X.J. (2010). Neurophysiological and computational principles of cortical rhythms in cognition. Physiol. Rev. 90, 1195-1268.

Wenger Combremont, A.L., Bayer, L., Dupre, A., Muhlethaler, M., & Serafin, M. (2016). Effects of Hypocretin/Orexin and Major Transmitters of Arousal on Fast Spiking Neurons in Mouse Cortical Layer 6B. Cerebral cortex 26, 3553-3562.

Williams, R. H., Black, S. W., Thomas, A. M., Piquet, J., Cauli, B., & Kilduff, T. S. (2019). Excitation of cortical nNOS/NK1R neurons by hypocretin 1 is independent of sleep homeostasis. Cerebral Cortex, 29, 1090-1108.

Wu, W. N., Wu, P. F., Zhou, J., Guan, X. L., Zhang, Z., Yang, Y. J., ... & Wang, F. (2013). Orexin-A activates hypothalamic AMP-activated protein kinase signaling through a Ca2+-dependent mechanism involving voltage-gated L-type calcium channel. Molecular pharmacology, 84, 876-887.

Xia, J. X., Fan, S. Y., Yan, J., Chen, F., Li, Y., Yu, Z. P., & Hu, Z. A. (2009). Orexin A-induced extracellular calcium influx in prefrontal cortex neurons involves L-type calcium channels. Journal of physiology and biochemistry, 65, 125-136.

Yan, J., He, C., Xia, J. X., Zhang, D., & Hu, Z. A. (2012). Orexin-A excites pyramidal neurons in layer 2/3 of the rat prefrontal cortex. Neuroscience letters, 520, 92-97.

Chapter 6. Orexinergic modulation of the ventral tegmental area: a possible regulator of hippocampal-dependent θ rhythmogenesis

Abstract

In mice in which Ox2R is deleted in DA cells, the θ rhythm is dramatically potentiated during wakefulness. The effect is not observed in mice lacking Ox1R, or both receptors in DA cells (Li et al. 2020). The VTA^{DA} cells regulate the hippocampal θ wave generator, by sending projection fibres that activate the hippocampus via the forebrain septum. Here, we use $Ox2R^{Dat\text{-}CKO}$ mice to establish the proper experimental conditions to investigate the possible mechanisms underlying their θ-enriched waking profile, at both the network and the cellular level. I established appropriate recording conditions to study the firing activity in the VTA-hippocampal pathway, by using horizontal slices laid onto high-density multi-electrode array dishes. Global burst activity could be monitored for hours, in different experimental conditions, in slices from $Ox2R^{Dat\text{-}CKO}$ and the $Ox2R^{flox/flox}$ controls. Preliminary results suggest that OrxB tends to inhibit global firing in $Ox2R^{flox/flox}$ slices, whereas the effect is excitatory in in $Ox2R^{Dat\text{-}CKO}$, suggesting that the increased θ activity in the latter may depend on a relief of an inhibitory effect produced by Ox2Rs on firing activity of the VTA-hippocampal pathway.

Preliminary patch-clamp experiments on VTA^{DA} cells are consistent with this hypothesis.

Introduction

Both the excessive daytime sleepiness and cataplexy symptoms of narcolepsy powerfully respond to dopaminergic drugs: D2 receptor agonist injection into the ventral tegmental area (VTA, housing the A10 DA cell group) acutely aggravates cataplexy, while antagonists have the opposite effect, in narcoleptic dogs (Reid et al. 1996) and mice (Burgess et al. 2010).

Electrophysiological and RT-PCR experiments suggested DA^{VTA} cells express both Ox1R and R2 (Korotkova et al. 2003), which was recently confirmed by using Ox1R and R2 GFP-reporter murine lines (Li et al. poster). Both OrxB and OrxA increase the firing rate and induce a TTX-resistant depolarization in DA cells in the VTA (Korotkova et al. 2003), whereas in the adjacent *substantia nigra* (SN), DA cells are unresponsive to Orxs, but GABA neurons in the *pars reticulata* are directly excited by both peptides (Korotkova et al. 2002).

Orxs are also involved in excitatory synaptic plasticity of DA^{VTA} neurons (Borgland et al. 2006; Borgland et al. 2008): and infusion of Orx in VTA *in vivo* potentiates DA release in VTA targets, including the PFC and the nucleus accumbens

(NAc). At the behavioural level, DA^{VTA} activity correlates with reward and reward prediction (Schultz, 2015). DA^{VTA} cells, however, also respond to adverse alerting cues (Bromberg-Martin et al. 2010), suggesting that they encode motivational salience. The role of Orxs in modulating DA neurotransmission was recently proposed to be a critical aspect of its complex function in behaviour (Aston-Jones et al. 2010; Calipari & Espana, 2012; Boutrel et al. 2013; Shaw et al. 2017).

Our collaborators Sha Li and Anne Vassalli (University of Lausanne) found that DA-specific Ox2R CKO ($Ox2R^{Dat\text{-}CKO}$) mice exhibit a dramatic and constitutive increase of EEG θ frequencies in waking (Li et al. 2020). This was not observed in mice lacking Ox1R, or both receptors, in DA cells. While Ox2R binds with high affinities both the OrxA and B peptides, Ox1R binds much better OrxA. Thus, Ox2R differs from Ox1R in responding with high affinity to OrxB. It is noteworthy that the levels of OrxB in the rat brain were reported to be 2-3 times higher than OrxA levels (Mondal et al. 1999). Evidence for differential responses of the two Orx receptors in DA cells was reported at the electrophysiological level and in association with drug consummatory behaviours (Baimel & Borgland, 2012), but their significance is poorly understood.

The different electrocortical phenotype of the $Ox1R^{Dat\text{-}CKO}$ and $Ox2R^{Dat\text{-}CKO}$ mice suggests that the 2 receptors exert divergent functions within the Orx-to-DA pathway. The waking EEG spectrum of $Ox2R^{Dat\text{-}CKO}$ mice in baseline resembles the one induced by optogenetic stimulation of DA^{VTA} cell bodies, which promotes waking and induces awakening from both SWS and REMs (Eban-Rothschild et al. 2016). During 6 h continuous DA^{VTA} cell photostimulation, the mice sustained a waking state featuring a prominent ~9 Hz θ peak, suggesting that DA cell activation induces stable Theta-dominated wakefulness (TDW) expression. Oishi et al. (2017) indeed suggested that VTA-evoked waking is a specific subtype of wakefulness, that requires D2-like receptor signaling pathway, and may involve the NAc.

These observations are consistent with reports pointing to VTA as part of the broad network governing θ rhythm generation (Orzel-Gryglewska et al. 2014). As discussed earlier, different sources of θ activity are present in the brain, with a complex interplay (e.g., Talk et al. 2004; Paz, Bauer, & Paré, 2008; Korotkova et al. 2018; see also references in Chapter 5). VTA appears to be part of the network regulating the hippocampus, the region displaying the highest amplitude of θ waves and recently found to have an intrinsic θ rhythm generator (Amilhon et al. 2015). Silencing or lesioning the VTA disrupts, while local injection of dopaminergic agents

induces, hippocampal θ activity. DA fibres originating from the VTA activate the hippocampus via the forebrain septum, and local field potential (LFP) recordings in the VTA show strong θ activity both during REMs and active waking (Orzel-Gryglewska et al. 2014).

DA neurons display two major firing modes, a low-frequency tonic mode, and a high-frequency bursting mode. These are induced by distinct contexts and underlie distinct behaviours (Hyland et al. 2002). The DA neuron burst firing is under glutamatergic regulation and modulated by AMPA and NMDA receptors (AMPAR and NMDAR, respectively). NMDAR activation can evoke a burst of high-frequency firing, which is not observed under AMPAR activation. Experimental evidence is still fragmentary, but mathematical modelling suggests that the AMPAR/NMDAR balance is a major determinant of DA cell firing, with co-activation of AMPARs and NMDARs being the most efficient to induce high-frequency firing (Zakharov et al. 2016). Therefore, a decrease in NMDAR compared to AMPAR activation would tend to facilitate lower (<10 Hz), compared to higher (>20 Hz) frequencies, and thus could enhance θ oscillations. Because Ox2R signalling was shown to mediate postsynaptic NMDAR potentiation in DA^{VTA} cells (Borgland et al. 2008), loss of Ox2R in DA cells may unbalance the overall effect of Orx towards AMPARs, which would impair high-frequency firing,

and increase the cells propensity to show low (θ) frequency spiking. This may contribute to the enhanced baseline TDW expression of $Ox2R^{Dat\text{-}CKO}$ mice.

Understanding why the θ rhythm is selectively potentiated in mice in which Ox2R is deleted in DA cells, but not in mice lacking Ox1R, or both receptors, requires detailed understanding of the physiological role of each receptor. In principle, one should at least compare the effect of regulating either receptor in the local VTA circuit and in the intact VTA-hippocampal network. The latter purpose is particularly hard to reach, because of the experimental difficulties encountered with electrophysiological recordings on brain slices laid onto multi-electrode arrays. Here, we aimed to establish experimental conditions apt to investigate the possible mechanisms underlying their θ-enriched waking profile, by studying $Ox2R^{Dat\text{-}CKO}$ mice at the cellular and network level, for comparison with ctrl and Ox2R-Δ mice.

Materials and Methods

Brain slices

For the multi-electrode array (MEA) and patch-clamp experiments carried out at the University of Lausanne, a total of 11 young adult $Ox2R^{Dat\text{-}CKO}$ ($Ox2R^{flox/flox}$ $DAT^{+/cre}$) and 8 Ox2R-flox ($Ox2R^{flox/flox}$ $DAT^{+/+}$) mice (University of Lausanne) of both sexes (7 males and 4 females; and 5 + 3 nb,

respectively), ranging from P28 to P56, were used. The animals were housed with food and water *ad libitum* under an LD12:12 cycle (lights-on, i.e., Zeitgeber Time ZT0, at 08:00 AM). All experiments were performed in accordance with the Swiss federal law, and using protocols approved by the State of Vaud Veterinary Office.

After a deep anaesthesia with 5% isoflurane, mice were decapitated and the brains were rapidly extracted and placed in ice-cold solution, containing (mM): 90.9 CholineCl, 25 NaHCO3, 0.7 CaCl2, 2.5 KCl, 1.25 NaH2PO4, 7 MgCl2, 25 D-glucose, 3 Sodium Pyruvate, 3 myo-inositol and 11.6 ascorbic acid, and aerated with 95% O2 and 5% CO2 (pH 7.4). Coronal (300 µm thick) slices from the ventral tegmental area (VTA) were cut between -2.94 mm and -3.66 mm from bregma, or horizontal VTA slices (200 µm) were cut at -7.60 to -8.42 mm from bregma, 2.40 to 1.58 mm from the interaural line (Franklin & Paxinos, 2008), with a VT1000S (in Milano, Leica Microsystems) or MICROM HM 650 V vibratome (Lausanne, Thermo Scientific) and then maintained at 30°C in the above solution for at least 1h before being transferred to the recording chamber or onto the MEA chip. The horizontal slices also contained a portion of the hippocampal formation connected to the VTA tissue as spared by the cut.

For the patch-clamp experiments carried out at the University of Milano-Bicocca, a total of 2 juvenile female C57BL6/J mice (Charles River, USA) and 2 male Ox2R-Δ ($Ox2R^{GFP/GFP}$ $DAT^{+/+}$) mice (University of Lausanne), ranging from P14 to P19, were kept in pathogen-free conditions, with free access to food and water, and a 12 h light-dark cycle. The described procedures followed the Italian law (2014/26, implementing the 2010/63/UE) and were approved by the local Ethical Committee and the Italian Ministry of Health (68/2021-PR).

MEA recordings

For extracellular neuronal recordings a CMOS-based high-density microelectrode array was used (HD-MEA; single-well MEA by MaxWell Biosystems). The HD-MEA features 11,011 electrodes in an area of 1.99 × 1.75 mm2 (17.8 µm center-to-center pitch, 3'161 electrodes/mm2 density). The size of each platinum electrode size is 10.2 × 8.6 $µm^2$. Platinum black is deposited on the electrodes to lower their impedance. Any subset of electrodes could be flexibly routed to 1020 channels to specifically acquire recordings from the area covered by the brain slice. The sampling frequency was 20'000 Hz and the LSB 6.294 µV. All recorded signals were amplified with a 512 x gain and filtered (high-pass: ~1 Hz, low-pass: 300 Hz) using on-chip circuitry. The detection thresholds were: 0.1 Hz for firing rate; 20 µV for spike amplitude; 200 ms for inter-spike interval (ISI). An external platinum wire attached to the

inner wall of the HD-MEA chamber served as the reference electrode.

Each slice was placed on top of the MEA chip with the help of an ACSF drop: once obtained the right orientation over the electrodes by gently rotating the tissue with a fine brush, the drop was dried up with paper wipes and the remaining water film under the tissue was thinned by absorption with filter paper. The position of each slice on the MEA chip was documented by acquiring a picture of it in the recording position just before placing it on the MEA recording system, by using a SMZ745 stereomicroscope (Nikon) equipped with an acquisition camera. The MEA chip was placed in the recording system, the contacts connected and the tissue holder arm properly positioned on top of the slice and lowered util the tissue was completely adherent to the chip at the bottom of the recording chamber.

The slice activity was recorded continuously at 34°C by means of a PH01 inline heater (Multichannel Systems) for the solution inlet. The solution perfusion of the recording chamber was achieved through a needle inlet with magnetic holder and a grounded rubber tube outlet; the flow was set to 3 mL/min. The ACSF composition was (mM): 129 NaCl, 21 NaHCO3, 1.6 $CaCl_2$, 3 KCl, 1.25 NaH_2PO4, 1.8 $MgSO_4$, 10 D-glucose, aerated with 95% O_2 and 5% CO_2 (pH 7.4). The slice was

allowed to settle down on the MEA chip for 15 minutes, and then the recordings were performed in the following fashion: an Activity Scan in control solution with all the possible 1020 electrode configuration subsets of the initial area selection; a Network Assay with the most active electrode configuration for each condition (5' control, 5' preconditioning drugs, 5' agonist/antagonist, 5' or 10' washout). In this way, the recordings can be considered at the steady state for each condition, minimizing the initial excitatory effect of the mechanical pressure the tissue holder exerts onto the slice when securing its position and adherence to the MEA chip.

For the burst analysis, the burst detection algorithm is based on three steps (MaxLab Live Software): spike times from all the recorded electrodes are binned into a histogram with a fixed bin size of 0.1 ms; the histogram is smoothed through convolution with a Gaussian kernel (kernel width = 0.3 s, default value) and normalized by the total number of recording electrode, giving the network activity plot; bursts in the network activity are detected by comparing neighbouring values in order to find all the local maxima of a curve. Only those peaks that meet criteria set by the parameters burst detection threshold = 1.2 and minimum peak distance = 1.0 s are selected.

Patch-clamp recordings

All experimental procedures carried out in Milano were executed as explained in Chapter 3. The recordings in Lausanne were performed with an equipment comprising: an upright microscope (Olympus BX50WI), a Multiclamp 700B (Molecular Devices) and iXon Camera X2481 (Andor), at 32-34°C. Micropipettes (3-4 MΩ) were pulled from borosilicate capillaries (TW150F-4; WPI) with a DMZ horizontal puller (Zeitz Instr.). Slices were perfused at 2.5-3 mL/min with artificial cerebrospinal fluid (ACSF) containing (mM): 126 NaCl, 24 NaHCO3, 2.4 $CaCl_2$, 2.5 KCl, 1.2 NaH_2PO4, 1.2 $MgCl_2$, 10 D-glucose, aerated with 95% O_2 and 5% CO_2 (pH 7.4). Pipettes contained (mM): 140 KGluconate, 10 HEPES, 10 KCl, 0.1 EGTA, 10 phosphocreatine, 4 Mg-ATP, 0.4 Na-GTP (pH 7.3). Traces were low-pass Bessel filtered at 2 kHz and digitized at 10 kHz, with pClamp10/Digidata 1322A (Molecular Devices). Only one neuron was sampled in each slice, to avoid uncontrolled long-term effects of neuromodulators (e.g. on receptor desensitization).

Drugs and solutions

Drugs and solutions were the same as in Chapter 4, except for DA and quinpirole, which were purchased from Tocris Bioscience (Bristol, UK), dissolved in distilled water at 1000x concentration, aliquoted and stored at -20°C.

Results

HD-MEA

The HD-MEA allowed to record the extracellular potential signal from the whole region of interest at high density around the most active subregions. We established the proper conditions to study the firing activity in the VTA-hippocampal pathway, by using horizontal slices whose global burst activity could be followed for about an hour, in different experimental conditions. This was achieved even if slice cutting is a traumatic event and causes a reduction in the recordable active units at the cut interface with the recording electrodes. In fact, the cut and recovery solutions contained CholineCl instead of NaCl, as well as ascorbic acid as antioxydant, drastically reducing the likelihood of an excitatory insult even to the most superficial cells, and thanks to energy supplements like sodium pyruvate and myo-inositol.

I recorded the VTA network activity in disinhibitory conditions, that are meant to enhance the spontaneous rhythmogenesis and θ resonance of the local network (Buzsaki, 2002). The hippocampus-generated θ activity is thought to comprise atropine-sensitive and atropine-insensitive components (Buzsaki, 2002). I revealed the atropine-insensitive θ activity by treating the tissue with 0 Mg^{2+} ACSF – to relieve the NMDAR block – plus bicuculline 20 μM – a blocker of $GABA_A$

receptors – to enhance the excitatory component of the network (Orzeł-Gryglewska et al. 2010). Conversely, I stimulated the atropine-sensitive θ activity with ACh 30 μM, which in turn depends, depends on GABAergic neurons' activity (Wang, 2010). The effect of ACh is composite, as it acts both on VTA^{DA} and on VTA^{GABA} neurons in VTA, and is generally excitatory (Picciotto et al. 2012). In this preparation we likely observed the combined effects on the hippocampal slab that was included in the brain slice and on the VTA proper. In both conditions I tested the effects of either OrxA 100 nM or OrxB 100 nM, to assess their specific contribution to the global network activity.

A sample of the obtained data is reported in Fig. 6.1. The firing activity referred to each acquisition channel is illustrated in the time raster plot, i.e., the temporal sequences of the spikes (displayed as ticks) recorded from each channel. Figure 6.1 shows two sample slices and recording results from an $Ox2R^{flox/flox}$ (A, B, C) and from an $Ox2R^{DatCKO}$ mouse (D, E, F). B and E show the heatmaps for the firing rate, the spike amplitude and the active electrodes, flanked by the relative histograms. C and F show the raster plot and network activity curve for the first 60 s of recording, as well as the histograms for n° of spikes per burst, burst duration, burst peak firing rate, and inter-burst interval. In the raster plot, each horizontal trace represents continuous recording from

one active electrode. The apparent columns reveal the network up-states or bursts, i.e., the periods during which most neurons fire simultaneously and their cumulative activity results as a detectable peak in the network activity curve (see Methods). In the network activity curve the computed network firing rate is plotted against time, to show the global firing patterns in the selected electrodes of the slice.

Figure 6.1. Typical HD-MEA recordings of VTA horizontal slices with ACh 30 μM. (A) Picture of the Ox2R$^{flox/flox}$ slice on top of the MEA chip with the chip boundaries and brain regions of interest highlighted. (B) Heatmaps of firing rate, spike amplitude and active electrodes, with relative histograms and the histogram for interspike intervals. (C) Raster plot and network activity curve, with histograms for n° of spikes per burst, burst duration, burst peak firing rate, and inter-burst interval. (D) Picture of the Ox2R^{DatCKO} slice on top of the MEA chip. (E) Same as B referred to D. (F) Same as C referred to D.

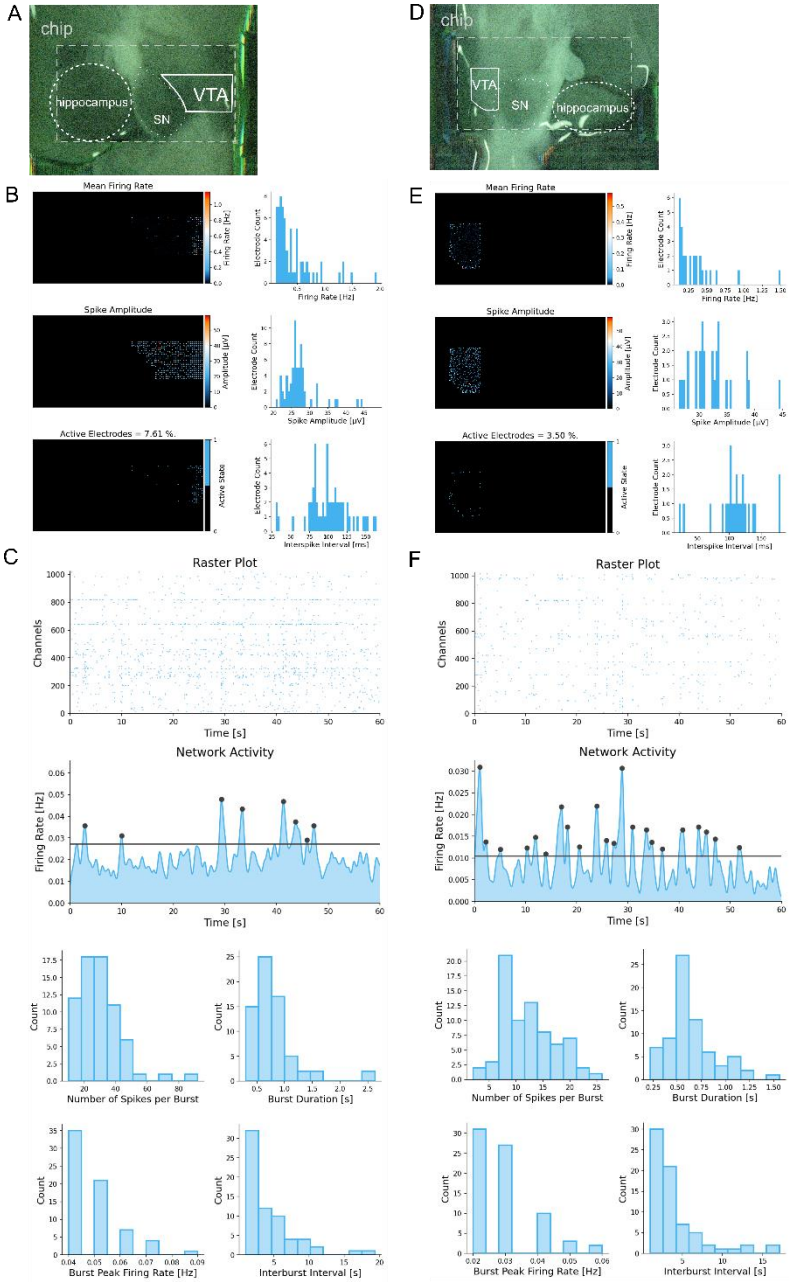
A
chip
hippocampus
VTA
SN
D
chip
VTA
SN
hippocampus
B
Mean Firing Rate
Firing Rate [Hz]
Electrode Count
Spike Amplitude
Amplitude [µV]
Spike Amplitude [µV]
Active Electrodes = 7.61 %
Active State
Interspike Interval [ms]
E
Mean Firing Rate
Spike Amplitude
Active Electrodes = 3.50 %
C
Raster Plot
Channels
Time [s]
Network Activity
Firing Rate [Hz]
Count
Number of Spikes per Burst
Burst Duration [s]
Burst Peak Firing Rate [Hz]
Interburst Interval [s]
F
Raster Plot
Network Activity

In these recordings, the global network activity can be measured by the network burst frequency, duration and inter-burst interval (IBI) (Table 6.1). The effects of Orxs on the VTA network were different depending on the stimulation protocol used. When the network was disinhibited in the control $Ox2R^{flox/flox}$ mice, OrxA 100 nM had an excitatory effect, that is it increased both the frequency and duration of the bursts, while reducing the IBI, whereas OrxB 100 nM showed an inhibitory action. On the contrary, in $Ox2R^{DatCKO}$ mice, OrxA reduced the burst frequency, while increasing burst duration and IBI, showing the ability to reduce the excitability of the network (not only fewer bursts, but also longer ones at a slower frequency). On the other hand, OrxB was mildly excitatory, as it increased burst frequency and decreased burst duration and IBI, so producing more frequent but shorter network bursts. When the network is stimulated through ACh, in $Ox2R^{flox/flox}$ mice, OrxA is mildly inhibitory whereas OrxB is excitatory. On the other hand, in $Ox2R^{DatCKO}$ mice, OrxA was mildly inhibitory (it lengthened both burst duration and IBI) and OrxB was clearly inhibitory.

Table 6.1. Global network activity parameters, burst analysis. Comparison between genotypes and pharmacological conditions ($Ox2R^{flox/flox}$ N = 2, 2, 2 and 1; $Ox2R^{Dat\text{-}CKO}$ N = 2, 1, 2 and 2).

Geno-type	Condition	Burst fr (Hz)	Burst duration (s)	IBI (s)
Ox2R$^{flox/flox}$	0 Mg^{2+} + bicuculline 20 µM	0.13 ± 0.12	0.67 ± 0.12	3.95 ± 0.73
	+ OrxA 100 nM	0.31 ± 0.01	0.71 ± 0.04	3.28 ± 0.10
	wash	0.40 ±0.07	0.74 ± 0.01	3.44 ± 0.04
Ox2R^{DatCKO}	0 Mg^{2+} + bicuculline 20 µM	0.27 ± 0.04	0.62 ± 0.03	3.86 ± 0.52
	+ OrxA 100 nM	0.11 ± 0.08	0.66 ± 0.04	9.70 ± 4.36
	wash	0.25 ± 0.01	0.63 ± 0.01	3.91 ± 0.23
Ox2R$^{flox/flox}$	0 Mg^{2+} + bicuculline 20 µM	0.17 ± 0.13	0.75 ± 0.01	3.99 ± 0.59
	+ OrxB 100 nM	0.15 ± 0.14	0.64 ± 0.12	52.27 ± 48.7
	wash	0.16 ± 0.13	0.68 ± 0.11	9.52 ± 5.99
Ox2R^{DatCKO}	0 Mg^{2+} + bicuculline 20 µM	0.23	0.68	4.27
	+ OrxB 100 nM	0.25	0.61	3.85
	wash	0.21	0.64	4.77
Ox2R$^{flox/flox}$	ACh 30 µM	0.29 ± 0.02	0.73 ± 0.03	3.43 ± 0.16
	+ OrxA 100 nM	0.24 ± 0.04	0.73 ± 0.0	4.29 ± 0.77
	wash	0.26 ± 0.01	0.74 ± 0.01	3.78 ± 0.26

Ox2R^{DatCKO}	ACh 30 µM	0.25 ± 0.01	0.69 ± 0.05	3.87 ± 0.19
	+ OrxA 100 nM	0.25	0.71	4.01
	wash	0.28 ± 0.01	0.68 ± 0.01	3.61 ± 0.13
Ox2R$^{flox/flox}$	ACh 30 µM	0.23	0.63	4.28
	+ OrxB 100 nM	0.27	0.72	3.78
	wash	0.23	0.68	4.3
Ox2R^{DatCKO}	ACh 30 µM	0.25 ± 0.01	0.66 ± 0.02	3.80 ± 0.22
	+ OrxB 100 nM	0.16 ± 0.12	0.65 ± 0.0	10.77 ± 7.05
	wash	0.14 ± 0.10	0.65 ± 0.05	6.62 ± 2.22

The distribution of action potentials with respect to bursts, which is an indication of the degree of synchronicity of the network, can be quantified by parameters such as the percentage of spikes within bursts, the number of spikes per burst (global data or normalized on each electrode; Table 6.2). The percentage of spikes within bursts tended to increase on excitatory pharmacological stimulations, and conversely for inhibitory stimulation, in the presence of 0 Mg^{2+} + bicuculline. On the contrary, in the presence of ACh 30 µM, the percentage of spikes within bursts was increased by OrxA and decreased by OrxB, in both genetic backgrounds. The number of spikes per burst and the number of spikes per

burst per electrode tended to decrease in $Ox2R^{flox/flox}$ tissue with 0 Mg^{2+} + bicuculline 20 µM + OrxA 100 nM, or with ACh 30 µM + OrxB 100 nM, whereas they tended to increase in all the other conditions. This could be an indication that in these two conditions the network bursts become shorter and more frequent, with each containing fewer spikes.

Table 6.2. Degree of synchronicity of the network. Comparison between genotypes and pharmacological conditions ($Ox2R^{flox/flox}$ N = 2, 2, 2 and 1; $Ox2R^{Dat\text{-}CKO}$ N = 2, 1, 2 and 2).

Geno-type	**Condition**	**Spikes within bursts %**	**Spikes per burst**	**Spikes per burst per electrode**
Ox2R$^{flox/flox}$	0 Mg^{2+} + bicuculline 20 µM	37.66 ± 3.36	323.45 ± 301.89	0.35 ± 0.32
	+ OrxA 100 nM	40.85 ± 1.94	7.58 ± 0.44	0.01 ± 0.0
	wash	40.31 ± 4.57	9.93 ± 2.40	0.02 ± 0.0
Ox2R^{DatCKO}	0 Mg^{2+} + bicuculline 20 µM	39.72 ± 0.12	37.00 ± 2.88	0.07 ± 0.01
	+ OrxA 100 nM	30.17 ± 13.26	162.26 ± 131.08	0.19 ± 0.13
	wash	38.34 ± 4.30	37.48 ± 2.4	0.07 ± 0.02
Ox2R$^{flox/flox}$	0 Mg^{2+} + bicuculline 20 µM	51.09 ± 10.21	245.08 ± 236.74	0.28 ± 0.27
	+ OrxB 100 nM	48.24 ± 8.63	501.78 ± 492.89	0.50 ± 0.49
	wash	53.35 ± 15.58	352.42 ± 343.97	0.35 ± 0.34

Ox2R^{DatCKO}	0 Mg^{2+} + bicuculline 20 µM	36.88	14.33	0.03
	+ OrxB 100 nM	37.45	15.37	0.03
	wash	36.91	20.3	0.04
Ox2R$^{flox/flox}$	ACh 30 µM	40.74 ± 3.03	9.52 ± 1.61	0.02 ± 0.01
	+ OrxA 100 nM	34.60 ± 2.68	10.39 ± 0.81	0.02 ± 0.01
	wash	37.20 ± 0.08	10.5 ± 0.69	0.03 ± 0.01
Ox2R^{DatCKO}	ACh 30 µM	37.77 ± 0.57	12.78 ± 0.55	0.02 ± 0.0
	+ OrxA 100 nM	33.68	15.63	0.02
	wash	38.83 ± 3.1	12.09 ± 4.9	0.02 ± 0.0
Ox2R$^{flox/flox}$	ACh 30 µM	33.04	35.24	0.05
	+ OrxB 100 nM	37.27	9.04	0.01
	wash	32.26	17.55	0.03
Ox2R^{DatCKO}	ACh 30 µM	33.89 ± 0.75	25.59 ± 3.6	0.04 ± 0.01
	+ OrxB 100 nM	42.69 ± 9.57	516.58 ± 488.35	0.52 ± 0.48
	wash	35.33 ± 0.8	230.54 ± 187.05	0.27 ± 0.21

The characteristics of the activity within the bursts, on the other hand, are described by the burst peak firing rate and the inter-spike interval (ISI) outside the burst (Table 6.3). The effect of the pharmacological treatments on the burst peak firing rate and the ISI is heterogeneous, reflecting the fact that not in all excitatory conditions the burst peak firing rate was

increased, suggesting that the excitatory effects of orexins is more complex than simply increasing the mean spike frequency of neurons. In fact, the ISI outside bursts seems to be regulated, too, showing an effect also on the action potential distribution outside the bursts.

Table 6.3. Activity within and outside the bursts. Comparison between genotypes and pharmacological conditions ($Ox2R^{flox/flox}$ N = 2, 2, 2 and 1; $Ox2R^{Dat\text{-}CKO}$ N = 2, 1, 2 and 2).

Geno-type	**Condition**	**Burst peak firing rate (Hz)**	**ISI outside (s)**
Ox2R$^{flox/fl}$ ox	0 Mg^{2+} + bicuculline 20 µM	0.37 ± 0.33	4.55 ± 1.84
	+ OrxA 100 nM	0.02 ± 0.0	0.88 ± 0.07
	wash	0.02 ± 0.0	1.36 ± 0.44
Ox2R^{Da-} tCKO	0 Mg^{2+} + bicuculline 20 µM	0.09 ± 0.02	1.16 ± 0.06
	+ OrxA 100 nM	0.24 ± 0.16	2.40 ± 0.66
	wash	0.09 ± 0.02	1.23 ± 0.27
Ox2R$^{flox/fl}$ ox	0 Mg^{2+} + bicuculline 20 µM	0.30 ± 0.28	9.20 ± 8.31
	+ OrxB 100 nM	0.66 ± 0.64	3.90 ± 2.89
	wash	0.45 ± 0.44	5.04 ± 3.95
Ox2R^{Da-} tCKO	0 Mg^{2+} + bicuculline 20 µM	0.03	1.33
	+ OrxB 100 nM	0.04	1.22
	wash	0.05	1.81
Ox2R$^{flox/flox}$	ACh 30 µM	0.02 ± 0.01	1.07 ± 0.10
	+ OrxA 100 nM	0.03 ± 0.01	1.32 ± 0.48
	wash	0.03 ± 0.01	1.05 ± 0.21
Ox2R^{Da-} tCKO	ACh 30 µM	0.03 ± 0.01	1.40 ± 0.20
	+ OrxA 100 nM	0.03	1.70
	wash	0.03 ± 0.01	1.30 ± 0.56

Ox2R$^{flox/flox}$	ACh 30 μM	0.07	1.29
	+ OrxB 100 nM	0.02	1.06
	wash	0.03	1.13
Ox2R$^{Da-tCKO}$	ACh 30 μM	0.05 ± 0.01	1.45 ± 0.21
	+ OrxB 100 nM	0.60 ± 0.55	3.60 ± 2.20
	wash	0.34 ± 0.27	2.78 ± 1.43

In conclusion, our recording conditions allowed to record the VTA-hippocampal network activity in brain slices, under a variety of experimental conditions. My preliminary results can be summarized as follows:

- the OrxA effects seem to be generally opposite to those of OrxB in the same genetic background;
- OrxA and OrxB effects seem to be specular in several respects in the Ox2R$^{flox/flox}$ vs Ox2R^{DatCKO} background;
- when the network is disinhibited (0 Mg^{2+} + bicuculline 20 μM), the most conserved pharmacological effects across genetic backgrounds are those of OrxB; moreover, in both mice strains, the burst duration is increased by OrxA and decreased by OrxB;
- when the network stimulation is achieved through ACh 30 μM administration, conversely, the most conserved actions are those of OrxA, and, in both mice strains, the percentage of spikes within bursts is lowered by OrxA and increased by OrxB.

The differential effects of OrxA and OrxB within and between genotypes are consistent with the strikingly different results obtained in vivo by deleting individual receptors, and point to the necessity of flanking the MEA experiments with patch-clamp studies, aimed at dissecting the physiological role of OxR1 and OxR2 in the VTA microcircuit.

Patch-clamp

We identified VTA in coronal and horizontal sections by firstly locating the SN (whose reticular appearance is highly characteristic) and moving medially until the cellular boundary facing VTA (a more compact tissue region). We then selected putative VTA^{DA} neurons based on the big fusiform somata morphology and on some electrical features, such as fairly broad APs, rather depolarized V_{rest} (around -50 mV, sometimes spontaneously active) and a prominent I_h sag upon hyperpolarization (Fig. 6.2 A). We also assessed the VTA^{DA} neurons' response to DA as its inhibitory effect is often used as a marker of cell identity, even if the TH^+ neurons in VTA are variably silenced by DA depending on their position on the mediolateral axis (Krashia et al. 2017).

The AP features of VTA^{DA} neurons did not change significantly upon Orx administration (Table 6.4). However, OrxA 100 nM and OrxB 100 nM increased the AP frequency in VTA^{DA} from C57 mice (Fig. 6.2 B and C; Fig. 6.3 A and B),

whereas DA 10 μM reduced it, coherently to what reported in literature (Korotkova et al. 2003; Fig. 6.2 C). On the other hand, OrxA seems to have little effect on VTA^{DA} from $Ox2R^{Dat\text{-}CKO}$ mice, but OrxB retains its excitatory effect (Fig. 6.3 A and B). Moreover, DA is mildly inhibitory also on these cells (Fig. 6.3 C). VTA^{DA} neurons from Ox2R-Δ mice were excited by OrxA but little influenced by OrxB as for the spontaneous firing (Fig. 6.3 A and B). Nonetheless, OrxB caused baseline depolarization in three cells, sometimes accompanied by an increase in synaptic input.

Figure 6.2. Typical firing of a putative VTA^{DA} neuron and its response to OrxA and OrxB in C57BL/6J tissue. (A) Putative dopaminergic neurons were characterized by testing the firing response to consecutive depolarizing current steps, lasting 500 or 1000 ms. The responses to the -100 pA, 0 pA and 50 pA steps are reported; they show the classical hyperpolarization-triggered sag, attributed to I_h, and the broad AP. (B) Spontaneous voltage oscillations were recorded from a putative VTA^{DA} neuron. Each voltage trace represents 2 minutes of continuous recording, before, during (coloured line, when dashed the application began before when shown; the total length of application is 2 minutes), and after OrxA 100 nM application. These traces are representative of 3 independent experiments. (C) Same as B, but for OrxB 100 nM application. (D) Same as B, but for DA 10 μM application.

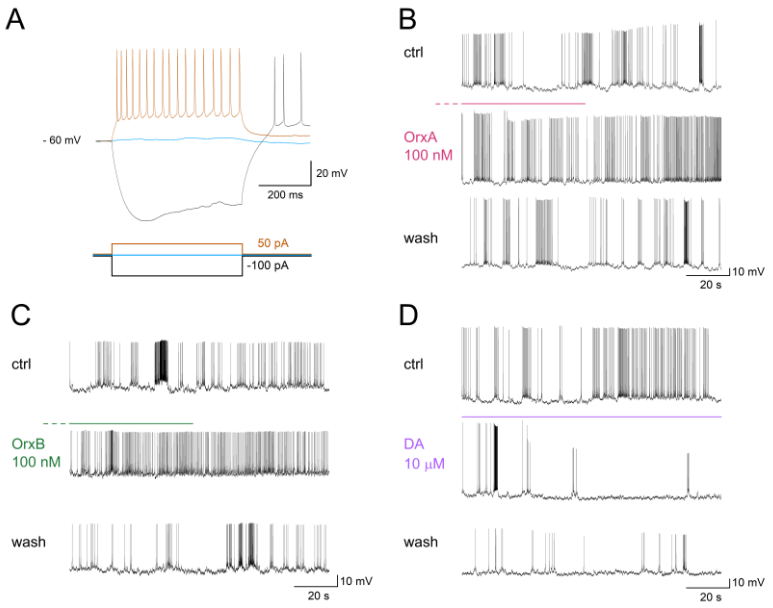

Figure 6.3. OrxB effects on AP frequency in putative VTA^{DA} neurons. (A) OrxB effect on AP frequency in Ox2R$^{Dat\text{-}CKO}$ mice. Bars give the average frequency, calculated from 2 min continuous recording in the indicated conditions, at the steady state (N = 3). (B) OrxB effect on AP frequency in Ox2R- mice. Bars give the average frequency, calculated from 2 minutes continuous recording (N =2).

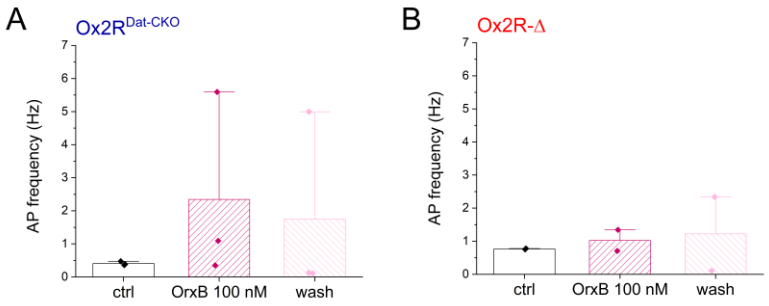

Table 6.4. Putative VTA^{DA} neurons' AP features. Comparison between genotypes and pharmacological conditions (C57BL6/J N = 3 and 1; $Ox2R^{Dat\text{-}CKO}$ N = 1 and 3; Ox2R-Δ mice N = 1 and 2).

AP feature	**Genotype**	**ctrl**	**OrxA 100 nM**	**wash**
AP Amplitude	C57BL6/J	61.4 ± 14.8	71.4 ± 17.9	70.1 ± 16.2
	$Ox2R^{Dat\text{-}CKO}$	61.4	59.0	47.3
	Ox2R-Δ	66.2	66.4	51.8
AHP Amplitude	C57BL6/J	-3.3 ± 0.5	-4.0 ± 0.3	-3.7 ± 0.6
	$Ox2R^{Dat\text{-}CKO}$	-4.3	-4.9	-5.6
	Ox2R-Δ	-4.0	-5.5	-4.4
AUC	C57BL6/J	0.0009 ± 0.002	0.002 ± 0.003	-0.06 ± 0.06
	$Ox2R^{Dat\text{-}CKO}$	0.0002	0.005	0.117
	Ox2R-Δ	-0.005	-0.004	0.03
AP Half-width	C57BL6/J	1.4 ± 0.2	1.2 ± 0.07	1.2 ± 0.06
	$Ox2R^{Dat\text{-}CKO}$	1.0	0.96	0.97
	Ox2R-Δ	1.5	1.7	3.4
Max Rise Slope	C57BL6/J	128.8 ± 31.5	167.9 ± 33.5	211.1 ± 45.8
	$Ox2R^{Dat\text{-}CKO}$	133.4	137.0	181.6
	Ox2R-Δ	126.7	114.8	57.42
Max Decay Slope	C57BL6/J	-44.1 ± 13.8	-59.7 ± 15.8	-87.6 ± 19.7

	Ox2R$^{Dat\text{-}CKO}$	-67.7	-69.9	-82.5
	Ox2R-Δ	-49.9	-45.2	-25.9
V rest	C57BL6/J	-47.8 ± 2.4	-47.9 ± 3.3	-48.3 ± 3.7
	Ox2R$^{Dat\text{-}CKO}$	-41.1	-45.0	-39.4
	Ox2R-Δ	-46.7	-45.9	-11.3
Rise slope	C57BL6/J	0.13 ± 0.02	0.37 ± 0.26	0.08 ± 0.007
	Ox2R$^{Dat\text{-}CKO}$	0.05	0.06	1.00
	Ox2R-Δ	0.12	0.05	4.9
Decay slope	C57BL6/J	-16.4 ± 13.4	-26.3 ± 14.7	-25.3 ± 14.2
	Ox2R$^{Dat\text{-}CKO}$	-15.4	-21.7	-17.6
	Ox2R-Δ	-24.8	-22.0	-4.3
AP feature	**Genotype**	**ctrl**	**OrxB 100 nM**	**wash**
AP Amplitude	C57BL6/J	35.9	37.3	36.7
	Ox2R$^{Dat\text{-}CKO}$	45.1 ± 3.4	44.1 ± 3.7	40.3 ± 5.0
	Ox2R-Δ	68.6 ± 13.2	56.7 ± 24.0	45.0 ± 32.0
AHP Amplitude	C57BL6/J	-3.2	-3.5	-3.4
	Ox2R$^{Dat\text{-}CKO}$	-5.4 ± 0.8	-5.4 ± 1.4	-5.2 ± 1.0
	Ox2R-Δ	-8.1 ± 1.6	-8.8 ± 1.0	-6.9 ± 2.5
AUC	C57BL6/J	0.003	-0.001	-0.08

	Ox2R$^{Dat-CKO}$	-0.002 ± 0.002	0.006 ± 0.001	0.02 ± 0.003
	Ox2R-Δ	-0.007 ± 0.009	0.05 ± 0.02	0.03 ± 0.002
AP Half-width	C57BL6/J	1.2	1.3	1.3
	Ox2R$^{Dat-CKO}$	0.84 ± 0.13	0.82 ± 0.28	0.87 ± 0.20
	Ox2R-Δ	1.8 ± 0.8	2.8 ± 1.8	8.1 ± 7.1
Max Rise Slope	C57BL6/J	79.3	82.0	103.9
	Ox2R$^{Dat-CKO}$	101.7 ± 0.3	140.31 ± 34.6	135.7 ± 126.4
	Ox2R-Δ	120.6 ± 74.1	105.6 ± 84.6	135.7 ± 126.4
Max Decay Slope	C57BL6/J	-27.7	-28.1	-38.6
	Ox2R$^{Dat-CKO}$	-70.2 ± 11.6	-96.8 ± 49.6	/
	Ox2R-Δ	-51.7 ± 29.1	-45.7 ± 37.3	-60.4 ± 55.0
V_{rest}	C57BL6/J	-50.4	-52.7	-54.1
	Ox2R$^{Dat-CKO}$	-43.0 ± 1.3	-45.3 ± 1.2	-43.9 ± 0.004
	Ox2R-Δ	-52.3 ± 3.6	-49.0 ± 7.6	-53.8 ± 2.4
Rise slope	C57BL6/J	0.14	0.07	0.10
	Ox2R$^{Dat-CKO}$	0.24 ± 0.13	0.49 ± 0.44	1.17 ± 1.06
	Ox2R-Δ	0.02 ± 0.004	0.01 ± 0.002	0.01 ± 0.0001

Decay slope	C57BL6/J	-1.5	-1.4	-1.6
	$Ox2R^{Dat\text{-}CKO}$	-34.3 ± 16.9	-34.9 ± 34.0	-27.0 ± 24.1
	Ox2R-Δ	-6.2 ± 0.9	-3.9 ± 0.9	-3.1 ± 2.3

Discussion

The data obtained with HD-MEA, although still preliminary, suggest that OrxA and OrxB exert differential effects on the VTA-hippocampal network, in agreement with the *in vivo* results on mice lacking either Ox1R or 2R. Because the basal spontaneous firing activity is well known to be low, in brain slices, we experimentally induced network disinhibtion by removing extracellular Mg^{2+} (to enhance NMDAR-dependent transmission) and partially depressing $GABA_A$Rs with bicuculline. In these conditions, in control mice OrxA favoured network bursts, whereas OrxB did the opposite. Because OrxB exerts its main effect on Ox2R, these data suggest that activation of the latter can cause a negative effect on the network activity. On the other hand, in $Ox2R^{DatCKO}$ tissue, OrxB stimulated MEA activity in slices, and a similar effect was observed in patch-clamp experiments. This suggests that perhaps the inhibitory effect of OrxB is directly exerted on VTA^{DA} cells, and disappears when Ox2R is deleted. In fact, we recently observed that, in control dissociated VTA^{DA} cells, OrxB applied onto the cell soma tends to decrease cell

firing (Grandi & Becchetti, unpublished results). Hence, our present working hypothesis is that removing Ox2R from VTA^{DA} cells removes a 'cell-autonomous' inhibitory effect, while leaves the excitatory input onto these cells, which is known to be stimulated by Ox2R (Borgland et al., 2008). Although orexins are generally considered to have excitatory effects, examples of inhibitory ones are also known (Leonard & Kukkonen, 2014). Our working hypothesis is highly simplified in that it does not consider the full complexity of the local VTA microcircuit, which is still far from being resolved (Morales & Margolis, 2017). An important further player is likely to be the VTA^{GABA} neuron, whose activity can strongly inhibit VTA^{DA} neuron firing (Bocklisch et al., 2013; Creed et al., 2014). VTA^{GABA} neurons are excited by both orexins (Korotkova et al., 2003 and 2004), as SN^{GABA} *pars reticulata* neurons are (Korotkova et al., 2002). Hence, it is also possible that the higher excitability of the VTA-septo-hippocampal pathway and the increase in TDW shown by $Ox2R^{Dat\text{-}CKO}$ mice is due to a specific Ox2R-dependent regulation of VTA^{DA} neurons, depending on modulation of the upstream VTA^{GABA} cells. When the Ox2R-dependent orexin sensitivity of VTA^{DA} neurons is impaired, the VTA^{GABA} cells could be unable to block the intrinsic θ-resonant hippocampal activity, either through VTA^{DA} activation or via another unknown mechanism. Unfortunatley, very little is known

about the OxR1 and R2 interplay in these cells. Testing our working hypothesis will require extensive patch-clamp studies on the VTA microcircuit.

By using MEA, I also tested ACh 30 μM, because of the well-known role of cholinergic stimulation in θ activity. In these conditions, OrxA seemed to prevent network bursts, whereas OrxB did the opposite, in control mice. The action was reversed in $Ox2R^{DatCKO}$ tissue, but in both backgrounds, the percentage of spikes within bursts was equally regulated by orexins. This indicates that modulation of this parameter is not dependent on Ox2R expression in VTA^{DA} neurons in these conditions, but likely mainly depends on the cholinergic stimulus. The cholinergic input from the tegmentum, PPT and LDT, increases VTA^{DA} cells firing and is likely to be important for burst firing of these neurons (Maskos, 2008). Moreover, the glutamatergic afferents to VTA^{DA} neurons contain nicotinic receptors of the α7 subtype and both the VTA^{DA} and VTA^{GABA} neurons contain α4*, β2* and α4*, β2* and α7* nAChRs, respectively (Klink et al, 2001). However, 65% of the cholinergic terminals form synapses onto non-DAergic neurons (Oakman et al, 1995; Garzon et al, 1999). Interestingly, VTA^{GABA} cell inactivation can be triggered by exposure to nicotine (Mansvelder et al., 2002), which first enhances GABAergic transmission, but soon causes a persistent depression of inhibitory inputs onto VTA^{DA} cells

caused by nAChR desensitization. Moreover, nicotine enhances glutamatergic transmission through nAChRs that desensitize less than those expressed on GABA neurons, and the net effect is a shift towards excitation of the DA reward system (Mansvelder et al., 2002).

It is therefore possible that ACh 30 µM stimulated a) glutamatergic terminals and b) VTA^{GABA} and VTA^{DA} neurons by somatic action. The MEA results lead to hypothesize that the burst activity duration in VTA could be mainly under GABAergic control, whereas the percentage of spikes within bursts depends on the excitatory glutamatergic transmission. Testing this hypothesis will also require extensive electrophysiological experiments on the VTA microcircuit.

References

Amilhon, B., Huh, C. Y., Manseau, F., Ducharme, G., Nichol, H., Adamantidis, A., & Williams, S. (2015). Parvalbumin interneurons of hippocampus tune population activity at theta frequency. Neuron, 86, 1277-1289.

Aston-Jones, G., Smith, R. J., Sartor, G. C., Moorman, D. E., Massi, L., Tahsili-Fahadan, P., & Richardson, K. A. (2010). Lateral hypothalamic orexin/hypocretin neurons: a role in reward-seeking and addiction. Brain research, 1314, 74-90.

Baimel, C., & Borgland, S. L. (2012). Hypocretin modulation of drug-induced synaptic plasticity. Progress in brain research, 198, 123-131.

Bocklisch, C., Pascoli, V., Wong, J. C., House, D. R., Yvon, C., De Roo, M., ... & Lüscher, C. (2013). Cocaine disinhibits dopamine

neurons by potentiation of GABA transmission in the ventral tegmental area. Science, 341, 1521-1525.

Borgland SL, Taha SA, Sarli F, Fields HL, Bonci A. (2006) Orexin A in the VTA is critical for the induction of synaptic plasticity and behavioral sensitization to cocaine. Neuron, 49, 589-601.

Borgland, S. L., Storm, E., & Bonci, A. (2008). Orexin B/hypocretin 2 increases glutamatergic transmission to ventral tegmental area neurons. European Journal of Neuroscience, 28, 1545-1556.

Boutrel, B., Steiner, N., & Halfon, O. (2013). The hypocretins and the reward function: what have we learned so far? Frontiers in behavioral neuroscience, 7, 59.

Bromberg-Martin, E. S., Matsumoto, M., & Hikosaka, O. (2010). Dopamine in motivational control: rewarding, aversive, and alerting. Neuron, 68, 815-834.

Burgess, C. R., Tse, G., Gillis, L., & Peever, J. H. (2010). Dopaminergic regulation of sleep and cataplexy in a murine model of narcolepsy. Sleep, 33, 1295-1304.

Buzsaki, G. (2002). Theta oscillations in the hippocampus. Neuron 33, 325-340.

España, E. S., & Calipari, R. (2012). Hypocretin/orexin regulation of dopamine signaling: implications for reward and reinforcement mechanisms. Frontiers in behavioral neuroscience, 6, 54.

Creed, M. C., Ntamati, N. R., & Tan, K. R. (2014). VTA GABA neurons modulate specific learning behaviors through the control of dopamine and cholinergic systems. Frontiers in behavioral neuroscience, 8, 8.

Eban-Rothschild, A., Rothschild, G., Giardino, W. J., Jones, J. R., & de Lecea, L. (2016). VTA dopaminergic neurons regulate ethologically relevant sleep–wake behaviors. Nature neuroscience, 19, 1356-1366.

Fadel, J., & Deutch, A. Y. (2002). Anatomical substrates of orexin–dopamine interactions: lateral hypothalamic projections to the ventral tegmental area. Neuroscience, 111, 379-387.

Garzón, M., Vaughan, R. A., Uhl, G. R., Kuhar, M. J., & Pickel, V. M. (1999). Cholinergic axon terminals in the ventral tegmental area target a subpopulation of neurons expressing low levels of the dopamine transporter. Journal of Comparative Neurology, 410, 197-210.

Hyland, B. I., Reynolds, J. N. J., Hay, J., Perk, C. G., & Miller, R. (2002). Firing modes of midbrain dopamine cells in the freely moving rat. Neuroscience, 114, 475-492.

Johnson, S. W., & North, R. A. (1992). Opioids excite dopamine neurons by hyperpolarization of local interneurons. Journal of neuroscience, 12, 483-488.

Klink, R., de Kerchove d'Exaerde, A., Zoli, M., & Changeux, J. P. (2001). Molecular and physiological diversity of nicotinic acetylcholine receptors in the midbrain dopaminergic nuclei. Journal of Neuroscience, 21, 1452-1463.

Korotkova, T. M., Eriksson, K. S., Haas, H. L., & Brown, R. E. (2002). Selective excitation of GABAergic neurons in the substantia nigra of the rat by orexin/hypocretin in vitro. Regulatory peptides, 104, 83-89.

Korotkova, T. M., Sergeeva, O. A., Eriksson, K. S., Haas, H. L., & Brown, R. E. (2003). Excitation of ventral tegmental area dopaminergic and nondopaminergic neurons by orexins/hypocretins. Journal of Neuroscience, 23, 7-11.

Korotkova, T. M., Ponomarenko, A. A., Brown, R. E., & Haas, H. L. (2004). Functional diversity of ventral midbrain dopamine and GABAergic neurons. Molecular neurobiology, 29, 243-259.

Korotkova, T., Ponomarenko, A., Monaghan, C. K., Poulter, S. L., Cacucci, F., Wills, T., ... & Lever, C. (2018). Reconciling the different faces of hippocampal theta: The role of theta oscillations in cognitive, emotional and innate behaviors. Neuroscience & Biobehavioral Reviews, 85, 65-80.

Krashia, P., Martini, A., Nobili, A., Aversa, D., D'Amelio, M., Berretta, N., ... & Mercuri, N. B. (2017). On the properties of identified dopaminergic neurons in the mouse substantia nigra and ventral tegmental area. European Journal of Neuroscience, 45, 92-105.

Li S, Franken P, Vassalli A. (2020) Constitutive active wakefulness in mice with hypocretin (orexin) receptor 2 inactivation in dopaminergic cells. Poster.

Li, S., Bandarabadi, M., Possovre, M.L., Tafti, M., Vassalli, A. (2020). Disruption of hypocretin/orexin receptor 1 or 2 in dopaminergic neurons differentially regulates waking theta and fast-gamma oscillations. J Sleep Res 29, Supplement 1, 9-10 (Meeting Abstract O17).

Mansvelder, H.D., Keath, J.R., & McGehee, D.S. (2002). Synaptic mechanisms underlie nicotine-induced excitability of brain reward areas. Neuron, 33, 905-919.

Maskos, U. (2008). The cholinergic mesopontine tegmentum is a relatively neglected nicotinic master modulator of the dopaminergic system: relevance to drugs of abuse and pathology. Br. J. Pharmacol., 153, S438-S445.

Mondal, M. S., Nakazato, M., Date, Y., Murakami, N., Yanagisawa, M., & Matsukura, S. (1999). Widespread distribution of orexin in rat brain and its regulation upon fasting. Biochemical and biophysical research communications, 256, 495-499.

Morales, M., & Margolis, E. B. (2017). Ventral tegmental area: cellular heterogeneity, connectivity and behaviour. Nature Reviews Neuroscience, 18, 73-85.

Ngolab, J. (2015). The Role of VTA Gabaergic Nicotinic Acetylcholine Receptors Containing the α4 Subunit in Nicotine Dependence: A Dissertation.

Oakman, S. A., Faris, P. L., Kerr, P. E., Cozzari, C., & Hartman, B. K. (1995). Distribution of pontomesencephalic cholinergic neurons projecting to substantia nigra differs significantly from those projecting to ventral tegmental area. Journal of neuroscience, 15, 5859-5869.

Oishi, Y., Xu, Q., Wang, L., Zhang, B. J., Takahashi, K., Takata, Y., ... & Lazarus, M. (2017). Slow-wave sleep is controlled by a subset of nucleus accumbens core neurons in mice. Nature communications, 8, 1-12.

Orzeł-Gryglewska, J., Kuśmierczak, M., & Jurkowlaniec, E. (2010). Involvement of GABAergic transmission in the midbrain ventral tegmental area in the regulation of hippocampal theta rhythm. Brain research bulletin, 83, 310-320.

Orzeł-Gryglewska, J., Matulewicz, P., & Jurkowlaniec, E. (2014). Theta activity in local field potential of the ventral tegmental area in sleeping and waking rats. Behavioural brain research, 265, 84-92.

Paz, R., Bauer, E. P., & Paré, D. (2008). Theta synchronizes the activity of medial prefrontal neurons during learning. Learning & Memory, 15, 524-531.

Peyron C, Tighe DK, van den Pol AN, de Lecea L, Heller HC, Sutcliffe JG, Kilduff TS. 1998. Neurons containing hypocretin (orexin) project to multiple neuronal systems. J Neurosci 18: 9996-10015.

Picciotto, M.R., Highley, M.J., & Mineur, Y.S. (2012). Acetylcholine as a neuromodulator: cholinergic signaling shapes nervous system function and behavior. Neuron 76, 116-129.

Reid, M. S., Tafti, M., Nishino, S., Sampathkumaran, R., Siegel, J. M., & Mignot, E. (1996). Local administration of dopaminergic drugs into the ventral tegmental area modulates cataplexy in the narcoleptic canine. Brain research, 733, 83-100.

Shaw, J. K., Ferris, M. J., Locke, J. L., Brodnik, Z. D., Jones, S. R., & España, R. A. (2017). Hypocretin/orexin knock-out mice display disrupted behavioral and dopamine responses to cocaine. Addiction biology, 22, 1695-1705.

Schultz, W. (2015). Neuronal reward and decision signals: from theories to data. Physiological reviews, 95, 853-951.

Talk, A., Kang, E., & Gabriel, M. (2004). Independent generation of theta rhythm in the hippocampus and posterior cingulate cortex. Brain research, 1015, 15-24.

Zakharov, D., Lapish, C., Gutkin, B., & Kuznetsov, A. (2016). Synergy of AMPA and NMDA receptor currents in dopaminergic neurons: a modeling study. Frontiers in computational neuroscience, 10, 48.

Chapter 7. Summary, Conclusions and Future Perspectives

α2* nAChRs role in epileptogenesis

In chapter 2, we studied the functional effects of the ADSHE-linked mutant $\alpha2^{Tyr252His}$ subunit in a human cell line expression system. It causes an overall reduction in the maximal response to the agonist, accompanied by a right-shift of the activation curve, which can be attributed to a strong decrease of the affinity of the ligand binding site for the agonist. Therefore, the $\alpha2^{Tyr252His}$ has a dominant negative effect and is probably responsible for the ADSHE pathogenesis in the patient carrying it.

The ADLTE-linked $\alpha2^{Arg121Leu}$ subunit seems to have a similar phenotype compared to the $\alpha2^{Tyr252His}$ but with a smaller current density reduction with saturating nicotine. However, the fact that ACh effects were not comparable to those of nicotine on the same receptors laid doubt on the possible causative role of the mutation for ADLTE and we decided to discontinue the study. We cannot anyway exclude an allosteric alteration of this mutation in linkage with the pathology.

Taken together, these results support the notion that loss of receptor function may be a more common epileptogenic mechanism for mutant α2 nAChRs, as compared to other

nicotinic subunits. Recent work in the mouse neocortex suggested that α2 nAChR subunits are specifically expressed in the Martinotti cells, usually somatostatin^{+}, that project to layer I and can synchronize the thick-tufted pyramidal cells in layer V in the θ frequency range (Hilscher et al. 2017). We can thus hypothesize that a decreased cholinergic response in Martinotti cells could reduce their responsiveness and increase their inhibition, which could lead to pyramidal cell synchronous excitation through Martinotti rebound excitation after the inhibitory phase (Becchetti et al. 2015; Hilscher et al. 2017). This kind of widely spread time-locked activity is often causative of epileptic events and it could be a plausible pathogenetic mechanism for the epileptic diseases to which these mutations are linked to.

Future studies on the specific cholinergic modulation of local rhythmogenesis by α2^{+} Martinotti interneurons' synchronizing activity in the PFC may help to better define the pathogenetic scenario of α2-linked epilepsies.

Dysfunctional SOM^{+} regular spiking interneurons and ADSHE seizures

In chapter 3 we analysed synaptic transmission and excitability in prefrontal layer V, in a murine model of ADSHE that displays a central feature of the human pathology: sleep-related seizures. The expression of β2^{V287L} throughout

development led to a selective modification of the glutamatergic input on layer V FS cells, which was accompanied by a higher sensitivity of regular spiking Martinotti cells to nAChR activation. These functional alterations were associated to prefrontal hyperexcitability. In analogy with other ADSHE models, the morphological changes in mice carrying the transgene were overall subtle. Nonetheless, these animals displayed a ~10% decrease in PFC thickness, which resembles the frontal cortex thinning observed in young patients (Lawson et al. 2002; Widjaja et al. 2011; Rahatli et al. 2020).

These results point to a possible role of α2* nAChRs in ADSHE seizures, as already suggested by the evidence of sleep-related epilepsy-linked mutations on CHRNA2, coding for the α2 nAChR subunit (Aridon et al. 2006; Conti et al. 2015; Villa et al. 2019). Recent work that PV^+ and SOM^+ GABAergic neurons cooperate in controlling feedforward inhibition at the front of epileptiform waves in vitro (Parrish et al. 2019). We found that, differently from FS cells, somatic nicotinic currents are detectable in the vast majority of SOM^+ RSNP cells, and their amplitude was larger in cells carrying $\beta2^{V287L}$. Hence, nAChR activation can potentiate the inhibition produced by these cells on pyramidal cell dendrites. Moreover, the effect of nicotine on RSNP cells was weakly sensitive to DHβE, which shows that non-α4 nAChRs are

expressed by these neurons. In fact, recent work demonstrated that α2* nAChRs are selectively expressed in layer V Martinotti cells (Hilscher et al. 2017), at least in mice. Hence, the simplest interpretation of our results is that in RSNP cells β2 mainly participates in α2β2 receptors, although specific antagonists for this nAChR subtype are not available. Regardless, the present observations point to layer V SOM^+ GABAergic neurons as possible culprits of α2-dependent ADSHE. Our working hypothesis is that loss-of-function α2* nAChRs could decrease the efficacy of pyramidal cell inhibition produced by SOM^+ cells, thus partially disinhibiting the local network. Whether the effect of α2* nAChRs could be exerted during network maturation, to produce permanent circuit alteration, remains to be determined.

Further work on the PFC microcircuit connectivity and specific rhythmogenesis modulation by ACh via α2* nAChRs could shed light on these pathogenetic mechanisms and, more generally, on activity synchronization in local neocortical networks.

A possible role for Ox2R in TMN histaminergic neuron maturation

In chapter 4 I've reported the data about the physiological validation of the Orexin Receptor 2 CKO mouse model, with

which we demonstrated that the Ox2R-flox conditional KO allele remains functional, but that CRE recombination creates a null phenotype (Ox2R-Δ).

We could highlight, as well, some small changes in the active properties of histaminergic neurons of the vTMN in the Ox2R-Δ mouse. These features lead to a slightly slower AP dynamics, suggesting a partly reduced maturation of histaminergic cells in Ox2R-Δ mice, that may be related to a possible role of Ox2R in the developmental specification of the histaminergic neuronal phenotype. Moreover, a study on narcoleptic human tissue showed an increased number of histaminergic neurons, which was not present in dog and mouse models of narcolepsy, suggesting a possible implication of the histaminergic system in the human pathogenesis of the disease and/or of the orexinergic system in the histaminergic one development, even if with enigmatic mechanisms (John et al. 2013).

However, the role of Ox2R in neuronal maturation still needs further investigation, and, if independently confirmed, this would be, to our best knowledge, its first evidence. Transcriptomic and proteomic studies may be helpful to this aim.

Both orexins modulate the microcircuit activity and θ rhythmogenesis in the PFC

In chapter 5 we studied the effects of OrxA and OrxB on the excitatory network in the PFC. Given this complex landscape of possible interactions and responses, the most likely mechanism for the observed orexinergic effects on layer V Fr2 Pys is the following: the excitatory effect of orexins on these neurons is mainly mediated by Ox1Rs, probably representing a mostly presynaptic contribution, to which a postsynaptic effect adds up, and both of them partially depend on the activation of L-type Ca_V channels. However, more studies are needed to clarify this complex signalling landscape. More studies are needed to understand the precise pathway through which OrxA exerts its effects on the murine prefrontal cortex, because the possibilities are many and show differences across age and animal models.

We also tried to enlarge the knowledge about Ox2R distribution in the murine PFC. The analysis of the distribution of the Ox2R by IHF highlighted a diffuse, speckled signal around putative cell bodies and in the neuropil with no clear subregion or layer-specific staining. The analysis of both OrxA:PV and OrxA:SOM colocalization wasn't significantly different across PFC subregions or layers, too, indicating a fairly uniform innervation of PV^+ and SOM^+ interneurons.

However, differences between orexinergic innervation of neurochemically different interneurons seem to be present in Ox2R-flox animals: the orexinergic innervation of SOM^+ interneurons seems denser than that of PV^+. However, when compared directly between Ox2R-flox and Ox2R-Δ tissue, the only different colocalization index is ICQ for mPFC layer V, which is higher in Ox2R-Δ, suggesting a putatively stronger innervation of SOM^+ interneurons in mice lacking Ox2R in a kind of compensative fashion. On the other hand, the analysis of both PV:Ox2R/GFP and SOM:Ox2R/GFP colocalization wasn't significantly different across PFC subregions or layers but for the ICQ, which is slightly higher in mPFC vs Fr2 for Ox2R-flox tissue, indicating a mainly uniform expression of Ox2R or its substitute GFP in PV^+ and SOM^+ interneurons located in different PFC subregions and layers in both genotype backgrounds. In Ox2R-flox animals there seems to be a higher expression of Ox2R on SOM^+ interneurons than on PV^+, even if with some uncertainty. To better assess if SOM^+ interneurons do express more Ox2Rs than PV^+ ones, other assays are needed, such as mRNA fluorescence in situ hybridization or real-time PCR on fluorescence-based sorted SOM^+ and PV^+ cells after tissue digestion.

Overall, this preliminary IHF data suggest that SOM^+ interneurons are more sensitive than PV^+ ones to the orexinergic input in the whole PFC, both because they seem

to be more densely innervated by $OrxA^+$ fibres and because they may express more Ox2Rs. This result is in line with the idea that orexins regulate rhythmogenesis in the PFC at frequencies around the θ band, given that SOM^+ interneurons are involved in the generation of ≈ 10 Hz oscillations in the pyramidal neuron activity in the neocortex (Hilscher et al. 2017) as well as in θ rhythm generation in the hippocampus (Amilhon et al. 2015; Mikulovic, 2016; Mikulovic et al. 2018). Moreover, SOM^+ interneurons chemogenetic activation increases EEG θ activity in M2 region, the premotor cortex, in close connection with Fr2/Fr2 (Funk et al. 2017), strongly suggesting an implication of SOM^+ interneurons in rhythm generation in the PFC.

The balance of OrxA and OrxB and their stability in extracellular fluid are unknown. At the present stage, we can hypothesize two mechanisms by which a strong decrease of Orx signals could lead to a paroxysmal increase in PFC θ activity associated with cataplexies.

1) Because some lines of evidence indicate that OrxB levels in the brain are 2-3 times higher than OrxA levels (Mondel et al. 1999), it is possible that the deletion of OrxA and OrxB could have stronger effects on SOM^+ interneurons (mainly expressing Orx2R). Relieving a tonic stimulation of these

interneurons could release Py cell activity, clustered around theta.

2) Deletion of OrxA and OrxB could cause a compensatory effect by increasing the complement of the receptors implicated in the other ascending excitatory pathways (e.g., the cholinergic), thus facilitating the onset of Py cell-dependent θ waves in PFC.

$Ox2R^{DatCKO}$ profoundly modifies the orexinergic modulation of the microcircuit activity in the VTA

In chapter 6, we investigated the effects of orexins both on the VTA global activity and on the VTA^{DA} firing.

The data obtained with HD-MEA, although still preliminary, suggest that OrxA and OrxB exert differential effects on the VTA-hippocampal network. Our present working hypothesis is that removing Ox2R from VTA^{DA} cells removes a 'cell-autonomous' inhibitory effect, while leaves the excitatory input onto these cells, which is known to be stimulated by Ox2R (Borgland et al., 2008). It is, however, highly simplified in that it does not consider the full complexity of the local VTA microcircuit, which is still far from being resolved. In fact, an important further player is likely to be the VTA^{GABA} neuron, which are excited by both orexins (Korotkova et al., 2003 and 2004). Hence, it is also possible that the higher excitability of

the VTA-septo-hippocampal pathway and the increase in TDW shown by $Ox2R^{Dat\text{-}CKO}$ mice is due to a specific Ox2R-dependent regulation of VTA^{DA} neurons, depending on modulation of the upstream VTA^{GABA} cells. When the Ox2R-dependent orexin sensitivity of VTA^{DA} neurons is impaired, the VTA^{GABA} cells could be unable to block the intrinsic θ-resonant hippocampal activity, either through VTA^{DA} activation or via another unknown mechanism. Unfortunatley, very little is known about the OxR1 and R2 interplay in these cells. Testing our working hypothesis will require extensive patch-clamp studies on the VTA microcircuit.

By using MEA, I also tested ACh 30 μM, because of the well-known role of cholinergic stimulation in θ activity. In these conditions, OrxA seemed to prevent network bursts, whereas OrxB did the opposite, in control mice. The action was reversed in $Ox2R^{DatCKO}$ tissue. However, the percentage of spikes within bursts was not dependent on Ox2R expression in VTA^{DA} neurons in these conditions, but likely mainly depends on the cholinergic stimulus. In fact, based on the literature, it is possible that ACh 30 μM stimulated a) glutamatergic terminals and b) VTA^{GABA} and VTA^{DA} neurons by somatic action. The MEA results lead to hypothesize that the burst activity duration in VTA could be mainly under GABAergic control, whereas the percentage of spikes within bursts depends on the excitatory glutamatergic transmission.

Testing this hypothesis will also require extensive electrophysiological experiments on the VTA microcircuit.

Publications

Chapter 2: Villa[1], C., Colombo[1], G., Meneghini, S., Gotti, C., Moretti, M., Ferini-Strambi, L., Chisci, E., Giovannoni, R., Becchetti, A., & Combi, R. (2019). CHRNA2 and nocturnal frontal lobe epilepsy: Identification and characterization of a novel loss of function mutation. *Frontiers in Molecular Neuroscience*, 12:17. [1] These authors have contributed equally to this work

Chapter 3: Meneghini, S., Modena, D., Colombo, G., Coatti, A., Milani, N., Madaschi, L., Amadeo, A., & Becchetti, A. The β2V287L nicotinic subunit linked to sleep-related epilepsy differently affects fast spiking and regular spiking somatostatin-expressing neurons in murine prefrontal cortex. Submitted paper (2022).

The references for this chapter are already contained in those of previous chapters, so they are omitted for the sake of brevity.

Acknowledgements - Ringraziamenti

Ringrazio il mio tutor Andrea Becchetti e la mia mentor, Marzia Lecchi, e tutti i membri passati e presenti del laboratorio di Neurofisiologia dell'Università di Milano-Bicocca: Aurora Coatti, Simone Meneghini, Francesca Gullo, Valentina Pastore, Laura Clara Grandi, Stefania Blasa, Simone Brusco, Lorenzo Corti, Sara Di Girolamo, Martina Simonti, Martina Barbieri, Giulia Guarisco. Grazie ad Alida Amadeo, Debora Modena e Niccolò Milani del laboratorio di Neuromorfologia dell'Università Statale di Milano. Senza l'insegnamento, il supporto e l'aiuto di voi tuttə non avrei portato a termine nessuno di questi lavori.

I would like to thank my co-tutor Anne Vassalli, and all the members of the Narcolepsy lab at the University of Lausanne: Mehdi Tafti, Stamatina Tzanoulinou, Sha Li, Pierre-Hugues Prouvot, Meriem Haddar, Almar Neiteler, Gianandrea Broglia, Corinne Pfister, Richie Kalusivikako, Mojtaba Bandarabadi. The time at Lausanne has been wonderful and professionally fruitful. I also would like to thank Anita Luthi for her kind availability, as well as Lila Banterle, Najma Cherrad and Laura Fernandez.

Grazie anche a tuttə ə colleghə e amicə che hanno condiviso con me la faticosa e bellissima strada del dottorato: a chi ha

scelto il DIMET come percorso di perfezionamento in quello strano ambito che è la biomedicina traslazionale; a chi ha condiviso le gioie e i dolori del terzo piano, un ecosistema di laboratori e persone che per primo in un ambiente lavorativo mi ha fatta sentire a casa; aə colleghə di dipartimento, perché solo imparando a guardarsi intorno e a dialogare ci si rende conto di non essere solə e si comprende che ogni lavoro nella scienza, anche quello svolto nella massima solitudine, è in realtà un lavoro condiviso; aə colleghə rappresentanti in università, aə compagnə militanti in ADI Milano e aə colleghə femministə con cui ho contribuito al Gender Equality Plan di Ateneo, perché l'Italia che governa deve imparare ad ascoltare l'Italia che vive e che lancia il Paese alla velocità del futuro; allə studenti che mi hanno insegnato a coltivare il loro talento e la loro intelligenza, perché il momento più bello è rendersi conto che la propria guida non serve più.

Infine, alla mia famiglia, aə miei carə e aə mieə amicə, senza cui non avrei mai avuto neanche lontanamente la motivazione necessaria a incolonnare i passi di questo percorso, dal primo all'ultimo.